UNIVERSITY OF CALIFORNIA

Santa Barbara

Adaptive Photothermal Emission Analysis Techniques for Robust Thermal Property Measurements of Thermal Barrier Coatings

A Dissertation submitted in partial satisfaction of the requirements for the degree

Doctor of Philosophy

in

Mechanical Engineering

By

Raymond Valdes

Committee in charge:

Professor Ted D. Bennett, Chair

Professor Eric Matthys

Professor Eckart Meiburg

Professor Carlos G. Levi

June 2016

The dissertation of Raymond Valdes is approved.

_____

Carlos G. Levi

_____

Eckart Meiburg

_____

Eric Matthys

_____

Ted D. Bennett, Committee Chair

March 2016

Adaptive Photothermal Emission Analysis Techniques for Robust Thermal Property Measurements of Thermal Barrier Coatings

by

Raymond Valdes

To

Melissa for all her love,

mis abuelitos por la inspiración,

my mom and dad for their faith and trust;

and all of whom have believed in me

ACKNOWLEDGEMENTS

In my first year at UCSB, I was introduced to Dr. Bennett through his graduate fluid mechanics and heat transfer series. His foundational approach to teaching heat, mass, and momentum transfer as a unified transport phenomena was a profound shift in how I model and solve physical processes in engineering. I would like to thank Dr. Bennett for mentoring me through my academic growth and learning necessary for me to complete my doctoral research and this dissertation. He has taught me how think critically and approach problems using multi-modal methods (theory, simulation, and experiment); this has helped me develop a broad range of skills as a researcher and engineer. His approach to writing has challenged me to write clearly and succinctly. Finally, he has been my biggest supporter and advocate at UCSB and tirelessly strove to help me in every opportunity and cross-road; I am forever indebted for his guidance.

I am thankful for my committee members for their insights and discussions that have helped me craft this dissertation, Prof. Carlos G. Levi, Prof. Eric Matthys, and Prof. Eckart Meiburg. I also gratefully acknowledge the funding of the LSAMP Bridge to the Doctorate Fellowship and Ford Foundation Pre-Doctoral Fellowship.

This research would not have been possible without the outstanding support of UCSB engineering, staff and technical assistance. Thank you Deryck Stave, Andy Weinberg, Greg Dahlen, Dave Bothman, Kirk Fields, Trevor Marks, Laura Reynolds, Katelynn Vargas, Julie Dunson, and Josh Johnson.

Special thanks to the professors that I have had the opportunity to TA with: Dave Bothman, Prof. Otger Campos, Prof. Bob McMeeking, Prof. Lina Kim, Prof. Glenn Beltz, and Dr. Bennett. Each have helped me develop my mentorship and teaching capabilities and it has been an honor teaching with you.

I would like to thank my graduate student friends Hans Mayer, Kevin Hoffseth, Michael Georgescu, Michael Simeone, and Christopher Peterson for their friendship and fellowship throughout the years. Mike Nava, my friend. Stephanie Mendes, my friend and then Fordie; her encouragement to reach high and her moral support inspired me to keep pushing. I would also like to thank my fellow Engr II Rm. 2215 labmates, Tyler Kakuda and Andy Tam, for welcoming me to Dr. Bennett's lab and staying in touch after their graduation to offer advice and encouragement.

I would like to thank my *Los Ingenieros* friends for their support and community – Angélica Cacho, Enrique Guzman, Marcela Arreyano, Jesús Cárdenas, Carolina Arreola, Alex Morales, Armando Veloz, Alfredo Torres, Irvin Martínez, Ruban Díaz, Aimee Flores, Amelia Herrera, Luis Garfias, Gonzalo Esparza, Jessica Mendez, Rosalía Zarate, Israel Téllez, Megan Chang, Jesús Medina, Dameon León, Luis Castellano, Javier Rodríguez, Jenny Lei, Vivian Vásquez, Michelle Nguyen, Pallavi Jain, José "J Lo" López, Jeff Georgette, José Tinoco, Rony Argueta, Christian Pérez, Areli Carnales, Abril Asencio, Edsel Pereyra, Phyllis Brady, Katherine Santizo, Debra Peña, Rigoberto Gutiérrez, Andrés Muñoz, Lupita Dávila, Sergio Sánchez, Josh Fierro, Monique Loy Fierro, Mario Mejía, Ernesto Cojoloun, Rudy Mendoza, Maritza

Sánchez, Carlos Maldonado, Pedro May, Edgar Ramírez, Patty Gómez, Victoria Melero, Jorge “George” Padilla and countless others that have welcomed me with open hearts and arms at UCSB.

I am thankful for my friends Jeff Gross, Eric Nord, Frank Menjivar, Ellison Chang, Jeff Kwak, Hooman Sherkat and Michael Gazaley; for nearly 25 years, we have pushed and supported each other to the highest levels of academic and professional excellence.

I am thankful to Kika Friend for inspiring me to do undergraduate research, who provided support and encouragement during my time at UCI, and who first recommended I apply to UCSB. Many thanks to Eyan Lee, Gus Toriz, and Jim Valenzuela, whose words and advice still hold true and guide me today, and who taught me to see the big picture, keep it real, and work independently. Jim, whom when I asked if I could do a summer research project, said “I support you 100%, … as long as I don’t have to do anything!”

Finally, I would like to thank my family: mis abuelitos (Zenaida Valdes y Leonardo Ulysses Valdes), Teresita, Tía Aymee and Ross, Tío Leo, my godfather (Robert Calix), Sophia, Alex and Emily. My mom (Maria de Los Angeles Valdes) for teaching me that education is the only thing you can truly own and for working tirelessly to provide us a safe and stable home. My dad (Ramon Valdes), who taught me that your dreams are only as big as your imagination. He has a remarkable ability to explain concepts in a

simple way; as a child I asked him how to get a PhD and he told me: “You have to write a book on something that nobody has done before”; he was right.

VITA OF RAYMOND VALDES

March 2016

EDUCATION

Bachelor of Science in Mechanical Engineering, University of California, Irvine, June 2009

Bachelor of Science in Aerospace Engineering, University of California, Irvine, June 2009

Master of Science in Mechanical Engineering, University of California, Santa Barbara, March 2014

University of California, Santa Barbara; Ph.D. Candidate, Department of Mechanical Engineering, 2012

PROFESSIONAL EMPLOYMENT

2011-2015: Graduate Teaching Assistant, Department of Mechanical Engineering, University of California, Santa Barbara

2006-2009: Project Engineering Intern, Fluid Control Systems, Parker Aerospace, Irvine, California

PUBLICATIONS

R. Valdes and T. D. Bennett, "Harmonically-Sustained Two-Color Pyrometry for Thermal Diffusivity and Thermal Conductivity Measurements," *In Preparation*. 2016.

R. Valdes and T. D. Bennett, "Coating thermal diffusivity and effusivity measurement optimization using regression-based sensitivity," *Review of Scientific Instruments*, vol. 86, no. 1, p. 015108, Jan. 2015.

T. D. Bennett and **R. Valdes**, "Differential phase of photothermal emission analysis for thermal property measurement of thermal barrier coatings," *Surface and Coatings Technology*, vol. 261, pp. 102–107, Jan. 2015.

AWARDS

Ford Foundation Pre-Doctoral Fellowship, UC Santa Barbara 2011-2014
LSAMP Bridge to the Doctorate Fellowship, UC Santa Barbara, 2009-2011
UC Irvine SAGE Scholar, UC Irvine, 2006-2009

FIELDS OF STUDY

Specialization: Thermofluid Sciences and Computational Science & Engineering
Studies in Photothermal Science with Professor Ted D. Bennett

PROFESSIONAL AFFILIATIONS AND SERVICE

American Institute of Aeronautics and Astronautics (AIAA)
Society of Automotive Engineers (SAE)
American Society of Mechanical Engineers (ASME)
Society for the Advancement of Chicanos and Native Americans in Science (SACNAS)
Los Ingenieros – UCSB Society of Hispanic Professional Engineers (SHPE)

ABSTRACT

Adaptive Photothermal Emission Analysis Techniques for Robust Thermal Property Measurements of Thermal Barrier Coatings

Raymond Valdes

The characterization of thermal barrier coating (TBC) systems is increasingly important because they enable gas turbine engines to operate at high temperatures and efficiency. Phase of photothermal emission analysis (PopTea) has been developed to analyze the thermal behavior of the ceramic top-coat of TBCs, as a nondestructive and noncontact method for measuring thermal diffusivity and thermal conductivity. Most TBC allocations are on actively-cooled high temperature turbine blades, which makes it difficult to precisely model heat transfer in the metallic subsystem. This reduces the ability of rote thermal modeling to reflect the actual physical conditions of the system and can lead to higher uncertainty in measured thermal properties. This dissertation investigates fundamental issues underpinning robust thermal property measurements that are adaptive to non-specific, complex, and evolving system characteristics using the PopTea method.

A generic and adaptive subsystem PopTea thermal model was developed to account for complex geometry beyond a well-defined coating and substrate system. Without *a priori* knowledge of the subsystem characteristics, two different measurement techniques were implemented using the subsystem model. In the first technique, the properties of the subsystem were resolved as part of the PopTea parameter estimation

algorithm; and, the second technique independently resolved the subsystem properties using a differential “bare” subsystem. The confidence in thermal properties measured using the generic subsystem model is similar to that from a standard PopTea measurement on a “well-defined” TBC system.

Non-systematic bias-error on experimental observations in PopTea measurements due to generic thermal model discrepancies was also mitigated using a regression-based sensitivity analysis. The sensitivity analysis reported measurement uncertainty and was developed into a data reduction method to filter out these “erroneous” observations. It was found that the adverse impact of bias-error can be greatly reduced, leaving measurement observations with only random Gaussian noise in PopTea thermal property measurements.

Quantifying the influence of the coating-substrate interface in PopTea measurements is important to resolving the thermal conductivity of the coating. However, the reduced significance of this interface in thicker coating systems can give rise to large uncertainties in thermal conductivity measurements. A first step towards improving PopTea measurements for such circumstances has been taken by implementing absolute temperature measurements using harmonically-sustained two-color pyrometry. Although promising, even small uncertainties in thermal emission observations were found to lead to significant noise in temperature measurements. However, PopTea analysis on bulk graphite samples were able to resolve its thermal conductivity to the expected literature values.

TABLE OF CONTENTS

Chapter 1 Introduction 1

Chapter 2 Background 9

2.1 Gas Turbine Engines and Thermal Barrier Coatings 9

2.2 Conventional Thermal Property Measurements of TBCs 15

2.3 Front Surface Photothermal Methods 21

2.3.1 Pulsed Thermal Imaging 21

2.3.2 Pulsed Thermography Method 22

2.3.3 Phase of Photothermal Emission Analysis Method 23

2.4 Summary 27

Figures 28

Chapter 3 Experimental Methods 39

3.1 Optical Heating 40

3.1.1 Laser Power 40

3.1.2 Laser Power and Stability 42

3.1.3 Laser Shape 43

3.1.4 Acoustic-Optical Modulation 44

3.2 Thermal Emission 45

3.3 Sample Mount 46

Figures and Tables 47

Chapter 4 Differential Phase of Photothermal Emission Analysis for Thermal Barrier Coatings..... 63

4.1 Introduction..... 63

4.2 Need for differential PopTea measurements..... 66

4.3 Model of heat transfer through coating, substrate, and subsystem..... 70

4.4 Application of subsystem model to dPopTea measurements..... 80

4.5 Conclusion..... 85

Figures and Tables..... 86

Chapter 5 Coating Thermal Diffusivity and Effusivity Measurement Optimization using Regression-based Sensitivity..... 91

5.1 Introduction..... 91

5.2 PopTea..... 95

5.3 Regression Analysis and Parameter Interval Estimates..... 99

5.4 Application to thermal diffusivity measurements..... 102

5.5 Summary and Conclusion..... 110

Figures and Tables..... 112

Chapter 6 Two Color Pyrometry for Thermal Diffusivity and Thermal Conductivity Measurements..... 125

6.1 Introduction..... 125

6.2 Photothermal Modeling..... 127

6.2.1 Model for temperature field..... 127

6.2.2 Model for thermal emission 132
6.3 Harmonically-Sustained Two-Color Pyrometry 136
6.3.1 Model for Surface Temperature Observations 136
6.4 Illustrative Experiments 138
6.4.1 Experimental Apparatus 138
6.4.2 Samples 140
6.4.3 Measurement Results and Discussion 142
6.5 Conclusion 148
Figures and Tables 150
Chapter 7 Conclusions 160
Appendix A: Differential PopTea Solution 165
Appendix B: Reflectivity Measurement 167
Appendix C: Biot Analysis for disk PopTea Model 170
Appendix D: Uncertainty Analysis for Two-Color Pyrometry 177
References 181

Chapter 1 Introduction

High efficiency power generation through gas-turbine engines (GTE) is possible through increased operating temperatures and more efficient thermal management systems [1]–[3]. Since operating temperatures are in excess of the metallurgical temperature limits of super-alloys [3] further near term increases to thermal efficiency, using super-alloys, will be dependent on the use improved of Thermal Barrier Coatings systems (TBCs) to provide thermal protection. TBCs are refractory ceramic coatings that protect underlying metallic surfaces from high temperature exposure and, with active cooling [4], have enabled the use of higher gas operating temperatures. Design of TBCs materials is functionally driven by thermomechanical requirements, including

low thermal conductivity, and the desire to provide “prime-reliant” performance over the designed lifetime of these coatings [5]–[7].

Thermal property measurements are beneficial to research and development, manufacturing, and for life-time monitoring of TBCs. Schulz, et al. summarized some of the benefits of measuring TBC thermal properties [8]: First, thermal conductivity is an important performance criterion, it can be used as a metric for ranking existing and novel coatings based on their thermal insulation efficiency. Second, the TBC fabrication process can be highly variable and can significantly impact thermal properties [9]. Third, isolating and determining the contribution of porosity, fine interlamellar defects, cracks, and other manufacturing variations on the resulting thermal properties can help provide guidelines for engine manufacturing to produce better coatings. Measuring thermal property changes on TBCs that have seen engine service will lead to more comprehensive lifetime prediction modeling that can better reflect the degradation effects of thermal cycling [10], thermal-shock [11], calcium-magnesium-aluminosilicate (CMAS) attack [12], syngas exposure [13], impact (FOD) [14], and other high-temperature effects. Finally, thermal properties are highly dependent on coating morphology and deposition on geometric curvature, common to gas turbine airfoil blades, can lead to significant morphological differences between coatings deposited on engine components as oppose to flat sample surfaces.

Despite its vital importance, in practice the desired level of thermal property characterization during production and post-service measurements of TBCs has not

been realized. Conventional thermal analysis techniques are unable to nondestructively evaluate the thermal properties of coatings on intact gas turbine components. Conventional methods require bulk or "free standing" samples to access both the front and rear side of the specimen [15]. Preparation of such samples can be unreliable, and working with a limited number of such samples may not capture all the manufacturing variability of coatings [15], [16]. In addition, conventional methods require optically opaque samples, that necessitate the use of optical coatings on semi-transparent TBCs, and are fundamentally thermal diffusivity (α) measurements that require additional heat capacity (C_p) and density (ρ) measurements to evaluate thermal conductivity: $k = \alpha \cdot \rho \cdot C_p$.

To increase the level of thermal property characterization of TBCs, some nondestructive front-sided thermal property measurements have emerged in recent years that address some of the limitations of conventional techniques. Nondestructive techniques share a common basis in optical heating, thermal transport modeling, and thermal response observations to estimate thermal properties. For example, the Pulsed Thermal Imaging (PTI) method applies a spatially uniform heat pulse to a TBC surface and measures the transient surface temperature with an infrared camera to resolve both the thermal diffusivity and thermal conductivity of the coating [17]. Bison et al. developed the Pulsed Thermography (PT) method that applies a Gaussian laser pulse to a TBC surface and the anisotropic in-depth and in-plane thermal diffusivity and

thermal conductivity is measured by tracking the transient temperature response [18], [19]. Phase of Photo-Thermal Emission Analysis (PopTea) measures the thermal phase response of coatings to sustained harmonic heating using a radiometric measurement of a single location on the front surface [20], [21]. The dependence on accurate thermal transport modeling that reflects the heating and sample characteristics has restricted both conventional and nondestructive techniques to well-defined and strictly controlled test samples and environments.

The motivation to move nondestructive methods away from imposing strict control over the characteristics of the samples is desired for making accurate measurements on complex, or unknown hardware configurations, and for evolving coating systems. Some simple examples of sample characteristics that can complicate coating measurements are effects of additional deposits developing on the TBC "topcoat", or delamination of the coating and substrate interface, or the underlying wall thickness. Most TBC are on actively-cooled high temperature turbine blades, illustrated Figure 1.1. Hollowed out cores on some parts of the turbine blade makes it difficult to precisely model the behavior of heat transfer into the metallic subsystem (below the coating) for specific thermal property measurement methods. This reduces the ability of rote thermal modeling to reflect the actual physical conditions of the sample, and can lead to higher uncertainty in measured thermal properties. This issue is a primary focus of the present dissertation. Building adaptive thermal modeling that can reflect changing sample characteristics and designing adaptive data reduction strategies to minimize and

filter out the use of ill-modeled experimental data is the key to developing robust measurement methods that can report thermal properties with the lowest uncertainty.

In general, PopTea, like other transient measurements, is highly sensitive to thermal diffusivity because of its prevalent role in the heat diffusion equation. However, PopTea has only a limited ability to resolve thermal conductivity from phase measurements that comes from the heat flow boundary condition at the interface between the coating and substrate material. This required thermal effusivity contrast may be obscured by the thickness of the coating or delamination between the coating and substrate, leading to inaccurate thermal conductivity measurements. However, incorporating temperature amplitude measurements into PopTea may lead to a desirable increase in sensitivity to thermal conductivity because of its direct relationship to the temperature scale. Exploring this possibility is another goal of the present dissertation.

This dissertation examines fundamental issues underpinning robust thermal property measurements that are adaptive to non-specific, complex, and evolving sample characteristics using the PopTea method. The motivation behind this research is the need to be able to make thermal property measurements of intact and serviceable TBCs on turbine hardware. To this end, the central challenges addressed in this dissertation are:

a) Develop an adaptive complex substrate model to reduce the influence of uncertainty of substrate geometries on the accuracy of thermal property measurements in Chapter 4.
b) Develop an uncertainty measurement optimization method of data reduction to minimize uncertainty by selectively filtering out experimental observations that deviate from a well-defined thermal model in Chapter 5.
c) Develop a harmonic two-color pyrometry method to enhance PopTea measurement through temperature amplitude analysis in Chapter 6. This is a preliminary step towards front-surface temperature measurements for reducing thermal conductivity uncertainty.

The unifying theme of these chapters is to reduce measurement error under uncertain physical conditions. This dissertation is organized as follows: In the chapters that follow this introduction, a thorough review of the state-of-the art understanding thermal property measurements of TBC systems is presented, with emphasis on the PopTea method, in Chapter 2. In Chapter 3, an overview of the experimental methods is presented, which includes a description of the optical heating and the thermal detection.

Chapter 4 presents the results of introducing an adaptive and generic subsystem thermal model to account for complex geometry beyond a well-defined coating and

substrate system. Experimental results are included to illustrate the method, including the demonstration of a differential PopTea approach for subsystem characterization. Complementary to addressing thermal behavior beyond a well-defined substrate, Chapter 5 will later explore a data reduction method for addressing model discrepancies.

In Chapter 5, the development of a regression-based sensitivity analysis is used to address the need to assess the uncertainty of the parameter estimation. The uncertainty method is applied to phase-spectra datasets with non-systematic bias-error introduced by model conformity discrepancies. This method's role in filtering out error for measurement optimization is discussed. This uncertainty measurement method is then the basis of uncertainty quantification in Chapter 6.

Chapter 6 extends the conventional two-color pyrometry method to make temperature measurements of a harmonically-sustained temperature field. This is the first time that the harmonic temperature amplitude-spectra are used in addition to the phase-spectra for the PopTea method. This is developed in conjunction with a single-layer disk thermal model to make thermal conductivity measurements using the temperature amplitude-spectra.

Finally, conclusions and recommendations for future directions are presented in Chapter 7.

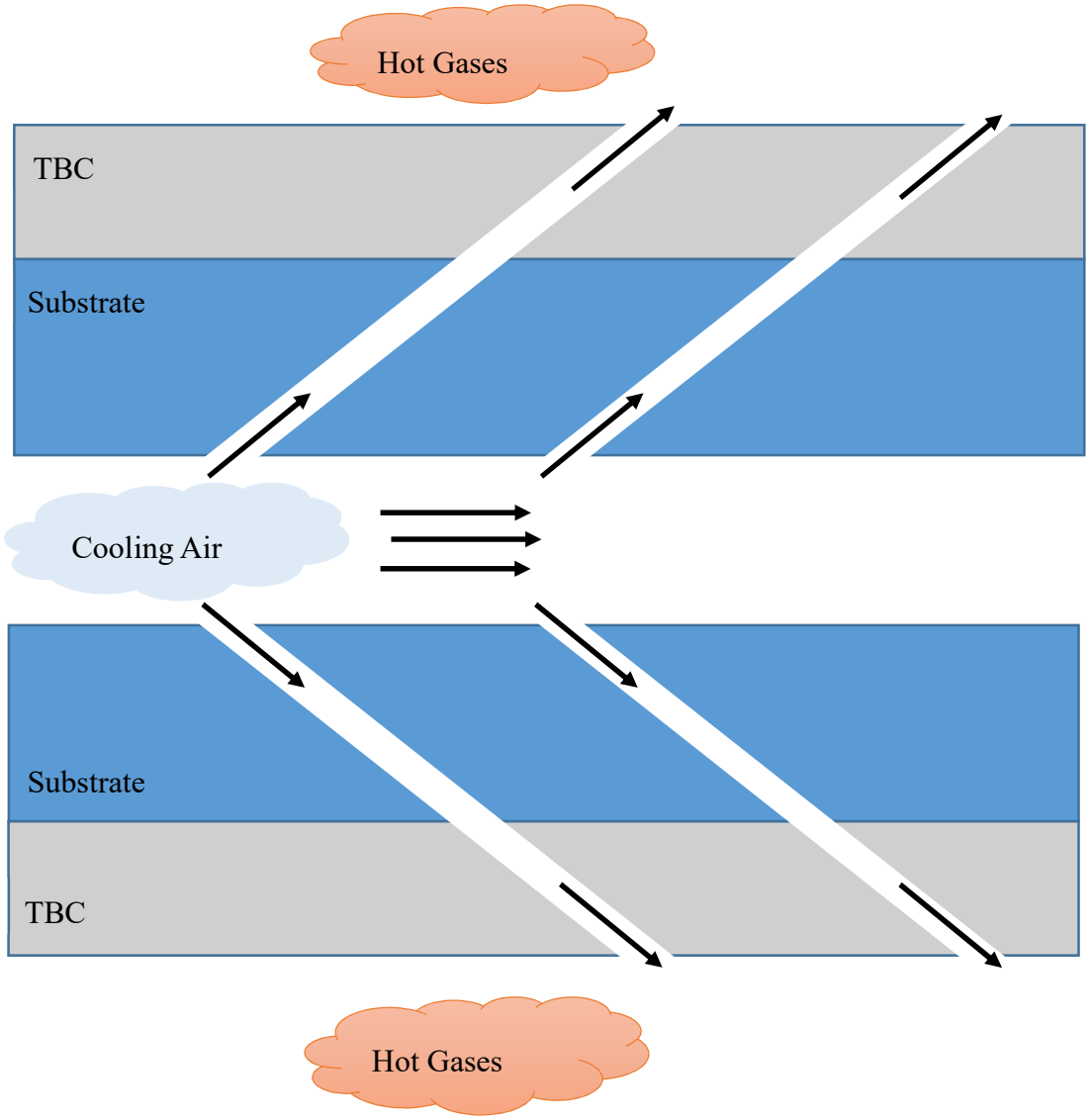

Figure 1.1: Cooling is routed through the turbine airfoil cross-section to remove heat absorbed by the component to maintain the temperature difference between the gases and the interior of the component. Figure adapted from Ref [22].

Chapter 2 Background

2.1 Gas Turbine Engines and Thermal Barrier Coatings

Gas Turbine Engines (GTEs) are used in a wide variety of applications, including, electricity generation, marine propulsion, aircraft propulsion ---both rotor and fixed-wing; a few of these implementations are illustrated in Figure 2.1. The Brayton thermodynamic cycle can be used to describe the thermodynamic states, heat transfer and work generated by GTEs. There are three fundamental components that drive this cycle, a compressor, combustor, and a turbine. The compressor increases the pressure of the inlet gas through a series of compressor stages, with typical overall pressure increases of 40:1 in aircraft GTEs [23]. The combustor elevates the temperature of the high-pressure gas; then, the high-pressure and high-temperature gas is expanded

through the turbine to produce work, Figure 2.2 shows a typical implementation for aircraft propulsion. The most demanding environments in a GTE are in the combustor and turbine stages.

Since the 1950's, when the first large-scale introduction of gas turbine engines for aircraft propulsion occurred, component operating temperatures have risen to well over 1300°C [24]. This rise in temperature has been made possible through advances in structural metal alloys, active cooling strategies, and advances in thermal barrier coatings (TBCs). This march towards higher temperatures is driven by the thermodynamics of an ideal Brayton cycle, which approaches the Carnot cycle efficiency given by:

$$\eta_{carnot} = 1 - \frac{T_i}{T_o} \tag{2.1}$$

where, T_i is the operating temperature of the gas at the turbine inlet and, for an open-loop cycle, and T_o is (ideally) the atmospheric temperature at the turbine outlet. However, the actual efficiency of GTEs are significantly lower due, in part, by active cooling methods necessary to remove heat absorbed by the turbine components [4].

Internal cooling of GTE parts is performed by heat convection, through jet impingement, pin-fin, and forced convection along a "serpentine" path within the component. Jet impingement is the redirection of a coolant flow directly against internal surfaces of the engine component. Pin-fin cooling is implemented by building

an array of fins or ribs within the component structure that serve as heat sinks that draw thermal energy from the component and into the coolant flow. External cooling is implemented by strategically placed holes and slots that sustain a coolant film over the engine component that increases the thermal boundary layer between the hot surrounding gases and the structure. Illustrations of these cooling methods are shown in Figure 2.3 and form the basis for the complex geometry and curvature within turbine components.

In addition to active cooling methods, high gas temperatures have been achieved by using TBCs. TBCs were first used in the 1980s to prolong the life expectancy of engine components under high temperature environments, and, as operating temperatures increase, they have become critical to maintaining the structural integrity of engine components. Figure 2.4 shows the general increase in gas operating temperatures due to advances in active cooling and TBC technologies.

Typical TBCs are a three-layer system, illustrated as Figure 2.5, which are deposited or grown on metallic substrates. The metal substrates are typically single-crystal nickel-alloys that have excellent thermal creep resistance. The first layer is an aluminum rich bonding coat that provides an aluminum reservoir for the thermally grown oxide (TGO). The α-Al_2O_3 TGO (second layer) serves as a thin $\sim 10\,\mu m$ but mechanically robust oxygen diffusion barrier that prevents corrosion of the metal substrate. The final topcoat is a thermally insulating oxide layer that is typically yttria partially stabilized zirconia (YSZ). Among high temperature ceramics, YSZ is uniquely

suited because it has low thermal conductivity and weight, can remain intact while withstanding large thermal stress and shock, and is chemically compatible with the underlying TGO and metallic substrates [25]. Top coats are typically deposited using electron beam-phase vapor deposition (EB-PVD) or air plasma spray (APS) methods. The EB-PVD process grows columnar grains normal to the surface that provides high "strain tolerance" to thermal stress by having the cracks and porosity between the vertical grains. The APS deposition melts powders and propels material as a spray to create a coating with a layered "splat" microstructure, having pores and cracks at the splat boundaries. The choice between these methods is based on the desired microstructure, thermal conductivity, and surface texture of the YSZ coating; an illustration of their microstructure is shown in Figure 2.6.

The key performance characteristic of the YSZ topcoat is that it has a much smaller thermal conductivity $(0.8-1.9\ \mathrm{W\cdot m^{-1}K^{-1}})$ [26] than the bond-coat and substrate layers $(\sim 10\ \mathrm{W\cdot m^{-1}K^{-1}})$ [27]. This means that even a very small deposition (100 μm to 1 mm) can create a significant $100-300°\mathrm{C}$ temperature drop from the YSZ surface to the metallic substrate. Since the TGO is thin, relative to the other layers, and the bond-coat has similar thermal properties to the substrate, it is a valid simplification to consider the TBC system as a two-layer structure, consisting of a topcoat and substrate material, with respect to thermal modeling.

For a given heat flux (q''), the top coat's thermal conductivity (k) and thickness (L) are the key properties that determine the temperature drop ΔT across the TBC:

$$\Delta T = \frac{q''L}{k} \tag{2.2}$$

Increasing this temperature drop, to maintain a desired substrate temperature, can be achieved by either reducing thermal conductivity, increasing the TBC thickness, or increasing the heat flux passing through the TBC system by the active cooling strategies previously described. Although modern GTEs use active cooling, there is a penalty with respect to the overall system pressure ratio and efficiency as air is bypassed from the compressor to the turbine components and is mixed with the hot gases. There are also practical limits on increasing coating thicknesses. In some applications, predominately in ground-based power generation, TBC coating can be $2-3$ mm thick. Thicker coatings can offer better durability and wear performance [28]. However, increasing the parasitic weight of engine parts can also pose significant problems, particularly in propulsion systems. Parasitic weight increases the startup rotational inertia of the turbines, increases the steady centrifugal loads on the turbine blades, and increases the overall weight of the engine. However, land based power generation engines are less sensitive to parasitic weights and this is often where thicker coatings are used.

The most desirable means for increasing the temperature drop across the coating is to reduce its thermal conductivity. Since thermal conductivity depends on the coating composition and microstructure, much active research is being done to improve the deposition processes and find alternatives materials that can lower thermal conductivity without sacrificing other performance criteria. The importance of predicting and estimating thermal conductivity based on material selection and processing conditions have lead researchers to develop analytical, numerical, and experimental methods for this objective.

The first-principles approaches for estimating thermal conductivity of heterogeneous materials are based on structural models using Series and Parallel Theory [29], two forms of Maxwell-Eucken Theory [30], [31] , and Effective Medium Theory [32], [33]. The Series and Parallel structural methods are based on assuming components are in the direction or parallel to the direction of heat flow [34]. The well-known Maxwell-Eucken models assume the components are spherical elements are in a dilute medium. The Effective Medium Theory is a statistical approach to structural modeling and has been reviewed by [35]–[37]. Wang presented a unifying equation that combines these five models based on simple combinatory rules [38]. The benefit of using analytical approaches come from their physical basis, and rapid and low computational cost of calculation. They serve an important role in validating numerical approaches [39], but their widespread use in thermal conductivity predictions for TBCs is limited by their difficulty to deal with nonuniform and evolving microstructures.

Numerical approaches using finite-element methods have shown much promise in predicting thermal conductivity. Emerging numerical methods tackle the challenge of nonuniform and complex microstructure by using micrographs to build numerical models based on the actual microstructure of the coating [40]–[42]. The benefits of these approaches is that they are useful in the parametric design of coatings and for elucidating the effects of microstructure. However, unless the microstructure of the coatings can be revealed using nondestructive methods, micrograph based numerical techniques will continue to remain as destructive measurement tools.

Analytical and numerical approaches for predicting thermal conductivity will continue to play an important role in the development of TBCs [42], [43]. The accuracy and precision of these approaches will continue to develop; however, the practical application of these methods are limited by their need for well-characterized microstructures, i.e. micrographs, that makes these destructive measurement methods. Their role should continue to grow as important verification and validation methods for experimental thermal conductivity measurements [44]–[46].

2.2 Conventional Thermal Property Measurements of TBCs

The ubiquitous use of coatings in gas turbine engines (GTE) drives the need for nondestructive evaluation (NDE) of thermal barrier coating systems (TBCs). Thermal property measurements infer the thermophysical properties of a material through its response to a heat source or heat flux. Several methods have been developed to address

the need for such measurements. All techniques fundamentally share three characteristics: (1) a heat transport model describing the flow of energy through the material, (2) an experimental means to probe the temperature field that results from this flow of energy, and (3) an inverse solution to the model based on a parameter estimation algorithm to determine unknown thermophysical properties [47].

Heat transport requires two thermophysical properties to describe the behavior of a system: thermal conductivity k and the volumetric heat capacity ρC_p (or equivalently k and thermal diffusivity $\alpha = k/\rho C_p$). However, most thermal property measurements seek to determine only one of these properties, with the advantage of simplifying the measurement method. For example, the conventional guarded hot plate technique [48], [49] utilizes steady-state heat diffusion to determine thermal conductivity. However, by eliminating time-dependent behavior it is impossible to measure properties related to thermal storage (i.e. ρC_p). On the other hand, methods that probe the transient behavior of heating, such as the thermal flash method [50], are used to measure thermal diffusivity. Dependencies on thermal conductivity are typically removed with the use of adiabatic or Direchlet boundaries [51]. Thermal Flash Method (also called Heat Pulse, Pulse, Flash, and Laser Flash method) [52], which is a ASTM standard method (E1461), is the most commonly used method for analyzing TBC thermal properties because is highly standardized and relatively simple. The thermal flash method generally requires separate measurements of density and heat capacity to resolve the

thermal conductivity of a material [53]–[56], or assumes a heat capacity value using the high temperature Dulong-Petit rule [57]. Relying on literature values of density and heat capacity to determine thermal conductivity from thermal diffusivity measurements can introduce a large degree of uncertainty [58]. For this reason, it is desirable to have a thermal property measurement method that is able to simultaneously resolve two independent thermal properties.

Measurements of thermal diffusivity require temporal measurements of temperature under conditions of known spatial scales for heat transfer. Scaling analysis [59] of the heat equation demonstrates that the spatial scale (Δx) and time scale (Δt) for heat transfer are related to thermal diffusivity by

$$\alpha \sim \frac{\Delta x^2}{\Delta t} \tag{2.3}$$

For example, for the thermal flash method, the time scale for heat transfer is determined from the thermogram (the temperature rise of the back surface - generally the time difference between the mid and max temperature values - in response to impulse heating of the front surface of the sample). The spatial scale for heat transfer in the thermal flash method is the thickness of the sample.

Alternatively, some thermal diffusivity methods use sustained harmonic heating, rather than the impulse heating of thermal flash. These methods have been implemented using the mirage effect [60], interferometry [61], optical reflectance [62], surface

displacement [63], and PopTea [21]. In such methods, the phase lag between heating and the thermal response of the sample is the measured time scale (when divided by the frequency of heating). Heat transfer can interact with known geometric scales in these measurements to determine thermal diffusivity. The benefit of using sustained harmonic heating is that the length scale of thermal penetration can be controlled by the heating frequency**.** This can be leveraged to make a large number of unique experimental observations as the thermal penetration probes deeper into the sample. However, the thermal flash method has had a long history of development and has been extended from bulk sample measurements to complex TBC systems. A common implementation of the thermal flash method is illustrated in Figure 2.7.

The thermal flash method, first developed by Parker, Jenkins, Butler and Abbott [50] ushered a family of non-contact methods which relied on heating the front surface of a sample and measuring the transient temperature evolution on the back surface through the use of an infrared detector. This method minimized much of the uncertainties associated with classical methods [49] by reducing the length of time required to make measurements and allowing the use of much smaller test samples [50]. The transient heat transport model and solution used by Parker is developed in Carslaw and Jaeger [64] for an opaque solid exposed to an instantaneous, uniform, and high pulse of energy at the front surface. This allowed for a relatively simple inversion for the thermal diffusivity $\left(\alpha = k/\rho C_p\right)$, such that the thermal diffusivity could be expressed as a function of the sample thickness and a time-scale parameter:

$$\alpha = 1.38\frac{L^2}{\pi^2 t_{1/2}} \tag{2.4}$$

where, the time-scale parameter $\left(t_{1/2}\right)$ is the time it takes the back face of the sample to reach half of its maximum temperature. This method can make measurements in a wide range of temperatures; for example, by increasing the sample steady state temperature Rudkin, Jenkins, and Parker were able to use the thermal flash method to measure the thermal diffusivity of titanium, molybdenum and Armco iron from $300-1800°C$ [65].

Thermal flash requires a high degree of sample preparation and measurement control for accurate measurements. Cowan [66] and Cape [67] demonstrated the need for including radiation and convective losses at temperatures greater than $1000\,K$ or by decreasing the sample thickness to reduce the timescale for thermal losses. Then, to allow accurate measurements of very thin samples, Cape, Taylor, Larson, Heckman, and Azumi [67]–[71] modeled the heat flux as a finite-pulse width. Furthermore, Chu, Taylor and Donaldson [51] argued that accounting for radial heat spreading was more relevant than the radiation or convection losses at elevated temperatures. These contributions have led to numerous solutions to the heat conduction equation that were developed to address multiple forms of heat loss and have emphasized the need for a strictly-controlled thermal flash experimental apparatus that can closely standardize these heat losses.

Thermal property measurements on TBCs differs from bulk samples because (1) they are composed of two or more distinct layers, (2) the topcoat can be semi-translucent to the heating wavelengths [72], [73] and (3) their thermophysical properties may be particularly dependent on the deposition process. The need for layered composite measurements were recognized and developed for the thermal flash method through changes in the heat conduction modeling [74]–[80]. The translucency of TBCs to radiative heating and thermometry [81] is typically addressed by applying optical coatings. However, the application of optical coatings, such as colloidal graphite, is not desirable. The porous nature of the coatings means the graphite is absorbed into the coating and this may make it difficult to remove from the surface. Furthermore, the graphite coating may act as a distinct thermal layer which influences the thermal modeling. Finally, it may be difficult to replicate the coating thickness in a systematic process [82]–[84]. The thermal flash method's need for front and rear access of the sample material means that measurements on engine hardware would require the destruction of the component. This would make the standardized thermal flash method unsuitable for tracking the evolution of the thermal properties due to in-service conditions.

In summary, the thermal flash method is widely used due to its long history and development, standardization, and many commercially available implementations (TA Insturments, Linseis, Netzsch Group). However, its need for front and rear access, optical coatings, and additional heat capacity and density measurements makes it

undesirable for nondestructive evaluation of TBCs on engine hardware. Front surface photothermal methods have emerged that address the limitations of the conventional thermal flash method.

2.3 Front Surface Photothermal Methods

The family of photothermal methods encompasses a wide range of techniques that uses optical heating as a convenient and precise form of heating [85]. The methods described in this section are three photothermal techniques that have been used to make thermal property measurements of TBCs. These methods all use optical heating sources (either by laser or flashlamp) to induce a temperature response in the TBC that can be measured. Since heating and thermal interrogation are both done at the front surface of the sample, these methods can be used for nondestructive evaluation of TBCS. This makes them promising candidates for making measurements on engine hardware.

2.3.1 Pulsed Thermal Imaging

Pulsed Thermal Imaging (PTI) was first developed as a “front-flash” thermal imaging nondestructive evaluation method to measure thermal diffusivity of ceramic composites, by Stuckey [86] and Sun [87]. The first implementation uses two Zenon flashlamps to apply a uniform pulse of thermal heating to the surface of a sample. A well-calibrated thermal imaging camera then measures the temperature response from the front surface, an illustration of the experiment is shown in Figure 2.8. A heat conduction model describes the pulse heating of the sample and is used to fit for thermal

diffusivity (α) and thermal effusivity (e) in a nonlinear parameter estimation algorithm. Thermal conductivity can be resolved from these thermal parameters by: $k = e\sqrt{\alpha}$. PTI has been used to detect small cracks and changes in porosity, and material nonunformity in ceramic composites [88] and delaminations of environmental barrier coatings on gas turbine vanes [89]. Further developments of this approach have been applied to TBCs on thin substrates [17] and the measurement has been expanded to make both thermal diffusivity and thermal conductivity measurements [90].

Some advantages of the PTI technique are that it can resolve both thermal conductivity and thermal diffusivity and it is fast for spatial mapping of coating properties because it captures the thermal imaging of a two-dimensional field [91]. The heat transfer model can accommodate a coating on a finite substrate which makes it a candidate for measurements on actual turbine structures. The limitation of PTI method is that the parameter estimation algorithm depends on a model of a surface temperature, similar to the thermal flash method. In order to measure the surface temperature of semi-translucent coatings the PTI method has needed to apply colloidal-graphite coatings to make thermal property measurements [17], [91]. The drawbacks of applying additional optical coatings to TBCs have already been previously described.

2.3.2 Pulsed Thermography Method

The Pulsed Thermography (PT) method is another type of “front-flash” thermal property measurement technique. The key characteristics of this method is that it uses

a laser to deliver a focused Gaussian-distributed heat pulse and a thermal imaging camera to view the thermal response, the experiment is illustrated in Figure 2.9. Two-dimensional anisotropic thermal modeling allowed for the resolution of both in-plane and through-plane thermal diffusivity and conductivity [18], [19]. This method has been used to study sintering and cracking of APS TBC coupons [92], the effects of APS deposition parameters [93], coating thickness of gypsum on marble [94], porosity of TBCs [95], and measurements on bulk solids [96]. The main drawback to this method is that it models laser heat absorption as a surface heat flux and circumvents the semi-translucency of the TBCs by applying optical coatings to the samples. The drawbacks of applying additional optical coatings to TBCs, to satisfy this thermal model, have already been previously described.

2.3.3 Phase of Photothermal Emission Analysis Method

The Phase of Photo-thermal Emission Analysis (PopTea) method was developed to address the limitations of the thermal flash method described in Section 2.2, the experiment is illustrated as Figure 2.10. It requires little sample preparation in that there is no need to apply optical coatings because the heat transport model accounts for the volumetric absorption and emission of thermal energy within the semi-transparent coatings [20], [21]; this makes it a truly noncontact evaluation method. Thermal modeling has been developed to address anisotropic thermal properties [20] that may

arise in EB-PVD coatings. And the PopTea method can resolve both thermal diffusivity and thermal conductivity.

The PopTea method shares some similarities with the thermal flash method, the PTI "front-flash" method, and the PT method; these methods measure a transient response to heating, and use infrared detectors to measure the thermal response from a heat source. However, differences are readily apparent in that the PTI, PT, and thermal flash method probes the sample with a heat pulse on one side and it then uses the temperature response on the back side (thermal flash Method) or front side (PTI and PT) to infer the thermal diffusivity of the sample. However, evaluating the temperature response needs a well-calibrated thermal detector. The PopTea method uses harmonic laser heating [97] and requires access to only the front side of the TBC. The harmonic thermal emission response from the front surface is interpreted by hemispherical and volumetric thermal emission modeling for the TBC system [98], [99].

For the PopTea method, assuming the harmonic temperature amplitudes are small relative to the steady state temperature, the thermal emission and laser heating will converge to the same harmonic functional form:

$$\begin{aligned} &\text{Harmonic Heating to TBC} && I(t) = \overline{I} + \tilde{I}\sin(\omega \cdot t) \\ &\text{Thermal Emission from TBC} && E(t) = \overline{E} + \tilde{E}\sin(\omega \cdot t - \phi) \end{aligned} \tag{2.5}$$

where the observed experimental measurements are based on the phase difference ϕ at an experimental laser modulation frequency $\omega = 2\pi f$, as illustrated in Figure 2.11.

The phase difference is independent to the emission signal strength and temperature amplitude; and, the measurement does not require either laser-power or detector calibration. The laser modulation frequency controls the depth of harmonic heating and this can be expressed as the thermal penetration

$$\text{thermal pentration} \sim \sqrt{\frac{\alpha}{\omega}} \tag{2.6}$$

Each change in thermal penetration results in a unique phase observation based on the thermophysical and optical parameters of the TBC system. Sweeping the laser modulation frequency makes it possible to make a large number of unique experimental observations that thermally probe the sample from the coating surface to deep into the system, a thermal penetration sweep is shown in Figure 2.11. As long as the thermal penetration reaches the coating and substrate interface, the heat conduction will have a dependence on thermal conductivity due to the heat flow continuity condition at the interface:

$$\begin{gathered} Q''_{in} = Q''_{out} \\ \left[-k_{coat} \frac{\partial T}{\partial z} = -k_{sub} \frac{\partial T}{\partial z} \right]_{\text{interface}} \end{gathered} \tag{2.7}$$

The heat conduction and then thermal emission model dependence on thermal diffusivity and thermal conductivity means that there is a reduced need for additional

"auxiliary" thermal property measurement methods to measure volumetric heat capacity and then thermal conductivity.

The ability of the method to make measurements without the need for access to the rear face of the sample has made it possible to make measurements on intact TBC systems. This has led to a series of investigations to demonstrate the capability of the PopTea method to track in-service coating degradations. Studies have elucidated thermal conductivity changes due to CMAS attack [100], thermal cycling [101], and thermal shock [102] on TBC samples. The thermal shock investigation by Yu incorporated a thermal resistance at the coating and substrate interface to identify delamination gaps. Additional studies, by Zhao, used the PopTea method to track changes in thermal conductivity due morphologies induced by rotating the substrate during deposition [103]. Finally, measurements have been made to study spatial variations in thermal properties on intact gas turbine engine components [102].

In summary, key strengths of the PopTea method is its ease of implementation because there is no need to characterize laser power or calibrate the thermal detector. The front face measurements have made it possible to make measurements on intact TBC systems. Volumetric thermal emission modeling has removed the need for additional optical coatings. Measurements that thermally probe into the substrate can resolve both thermal diffusivity and thermal conductivity; this reduces the need for additional thermal property measurement methods. However, PopTea is limited in that thermal conductivity measurements require a system with well-defined semi-infinite

substrate. The coating thickness must be known *a priori*, and the semi-steady harmonic nature of the experiment can lead to long measurement times. Finally, current implementations use a thermal detector to interrogate a small measurement spot; this makes it difficult to create 2-d thermophysical property maps.

2.4 Summary

Increases in thermal efficiency and performance of gas turbine engines have been made possible, in part, by thermal barrier coatings (TBCs) and active cooling methods. TBCs play a critical role in providing a thermal resistance between high temperature gasses and engine hardware and active cooling methods remove heat absorbed by the hot gasses. Characterizing and studying the evolution of the thermal properties of TBCs has been hindered by conventional thermal property measurement methods that need front and rear access to the TBC system. Furthermore, nondestructive thermal property measurements on gas turbine components presents unique thermal modeling challenges to front-surface thermal property measurement methods because TBC applications may be on structures with complex substrate geometries.

Figures

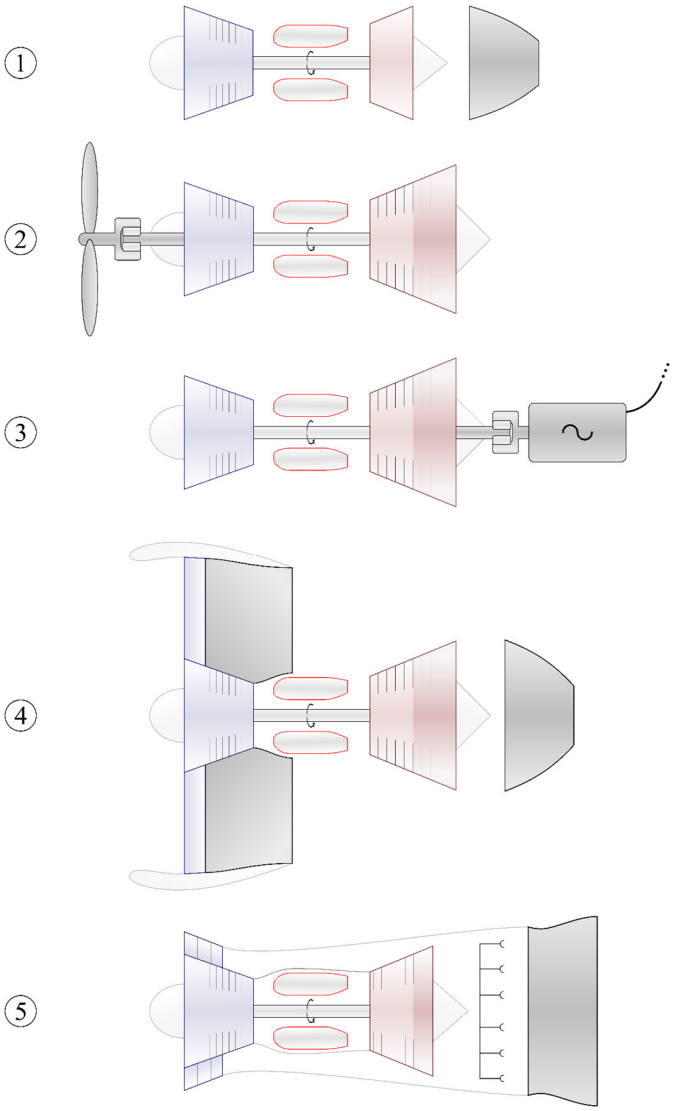

Figure 2.1: Gas turbine configurations, the compressor (blue), combustor (red-outline), and turbine (red) are shown. (1) turbojet (2) turboprop (3) turboshaft (4) high-bypass turbofan (5) low-bypass afterburning turbofan. Used under Creative Commons License, Ref [104].

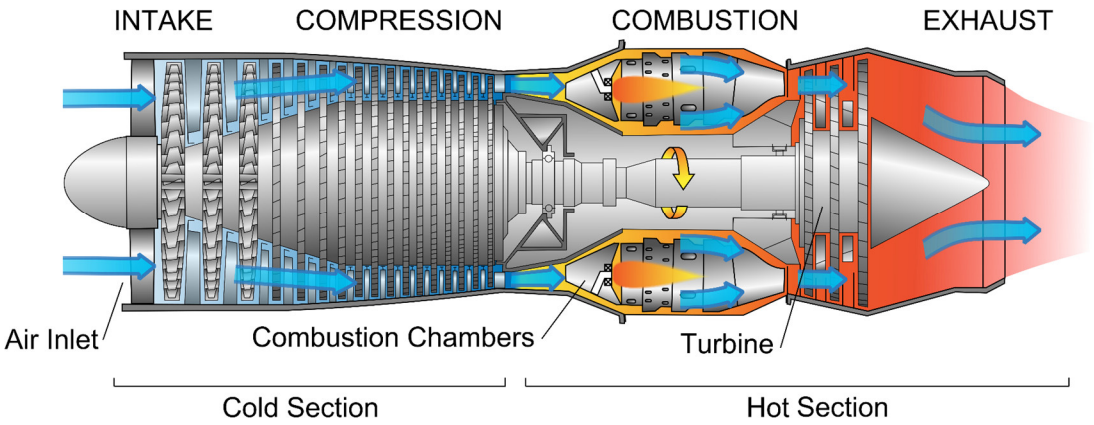

Figure 2.2: Typical high-performance jet engine for aerospace applications. Used under Creative Commons License, Ref. [105].

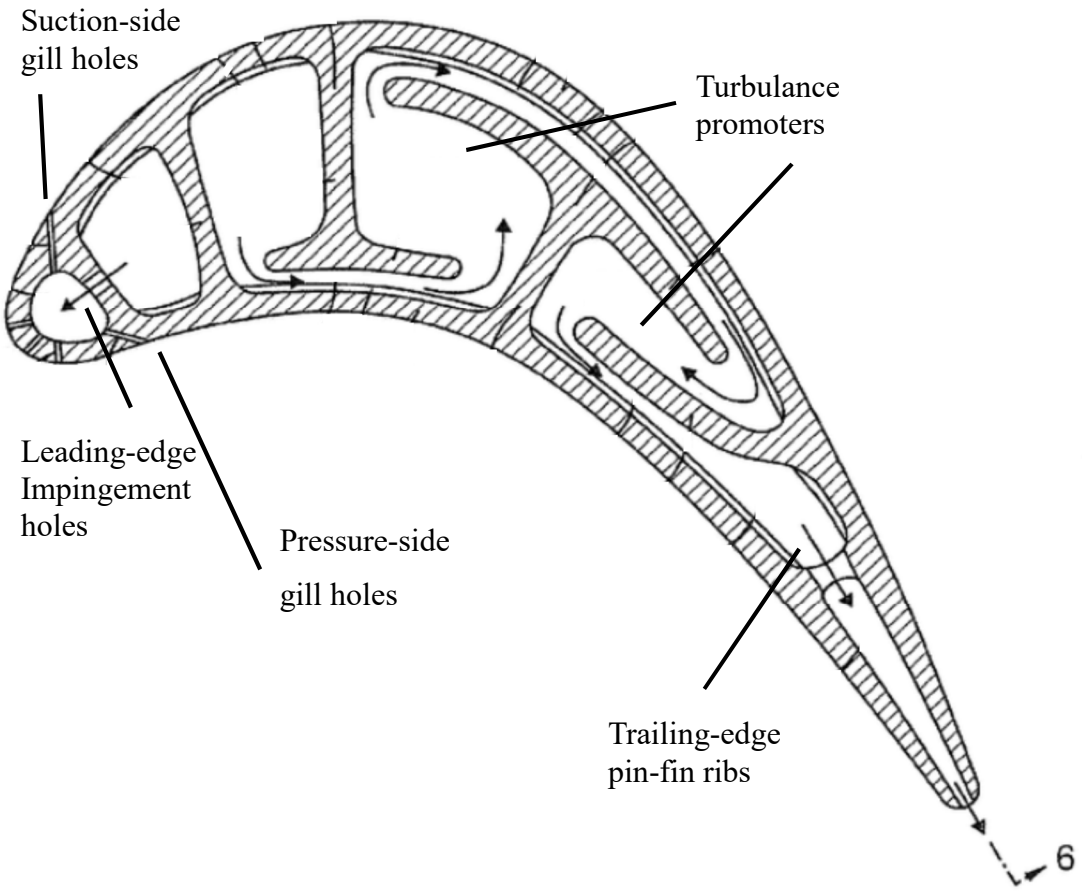

Figure 2.3: Turbine airfoil cross-section showing a combination of holes, coolant channels for film, impingement, internal, and pin-fin cooling; the geometric characteristics shown are meant to demonstrate the wide-variety of cooling implementations and may not all appear in any particular turbine blade. Figure adapted from US Patent US20120269648A1.

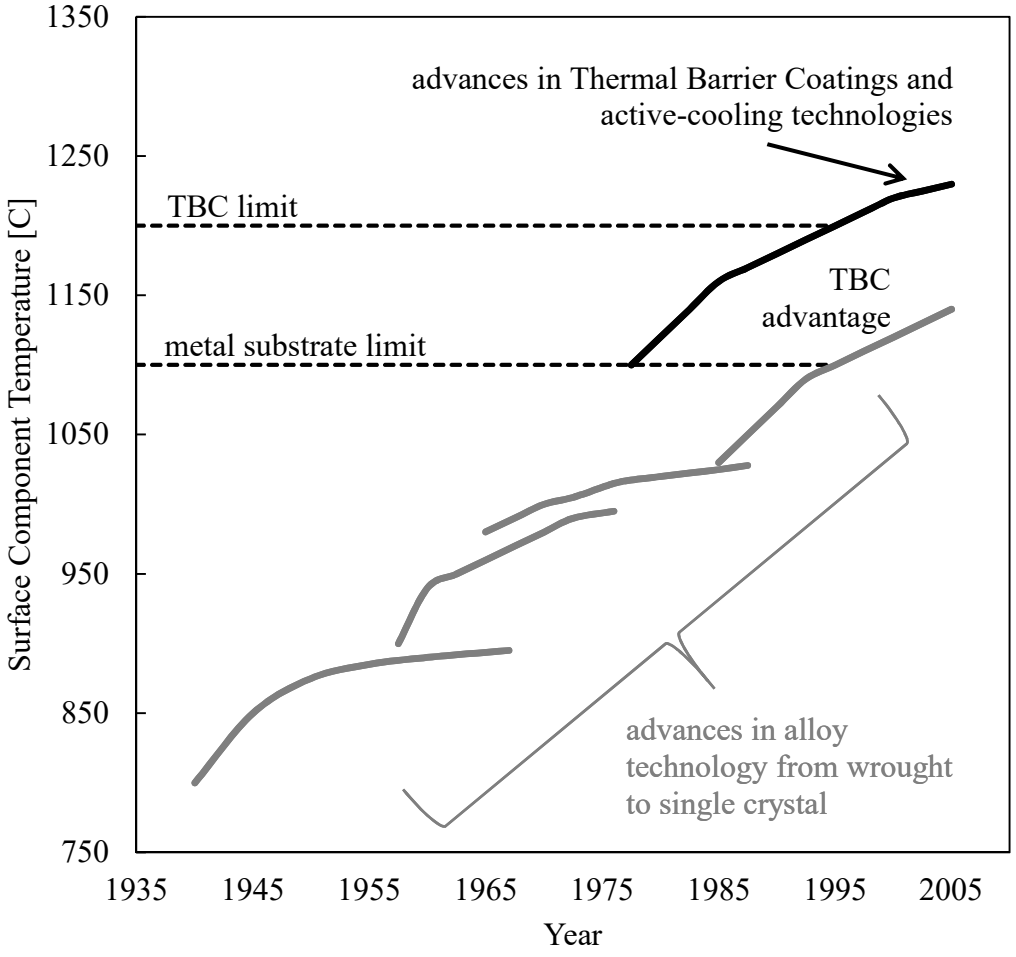

Figure 2.4: Increase of surface temperature of engine components due to high-temperature enabling technology. Figure adapted from [6], [8].

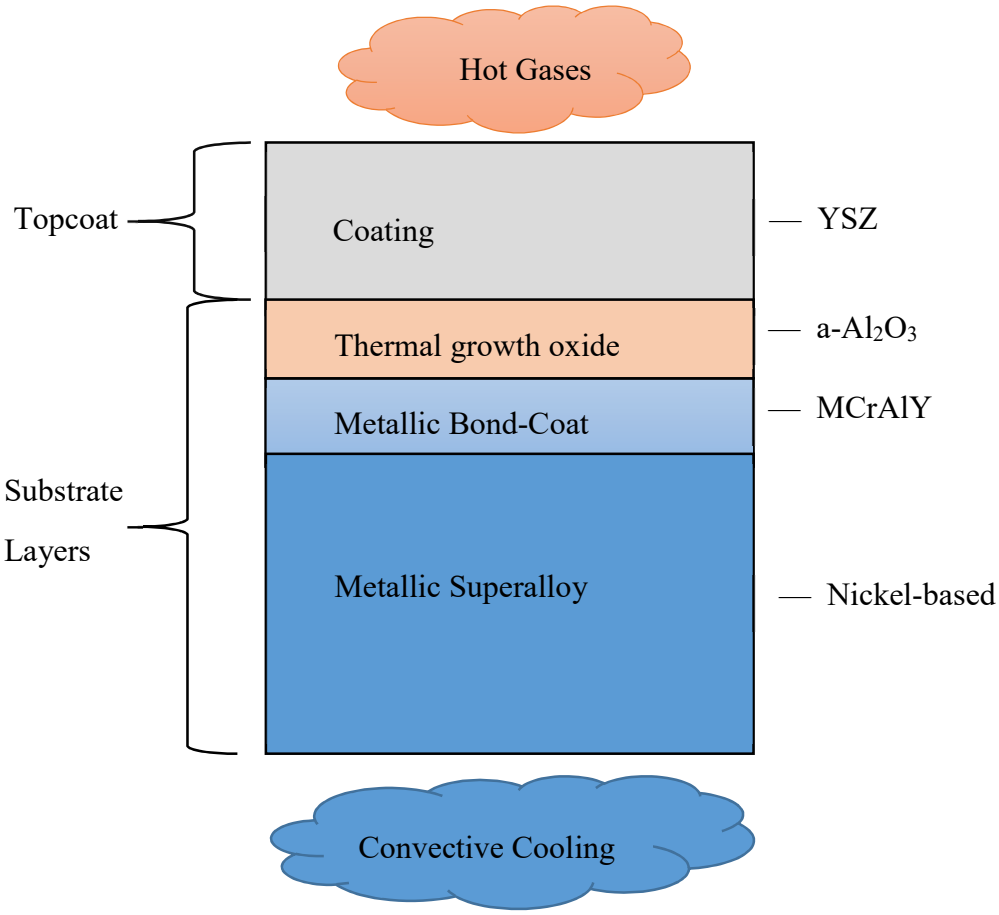

Figure 2.5: Typical Thermal Barrier Coatings systems are most often composed of a yttria stabilized zirconia (YSZ) topcoat, a thin thermal growth oxide, and a metallic bond coat adhered to a super-alloy. The coating may be designed to induce a $100-300°C$ temperature drop between the surface of the coating and the superalloy substrate. Figure adapted from Ref. [106] and is not drawn to scale.

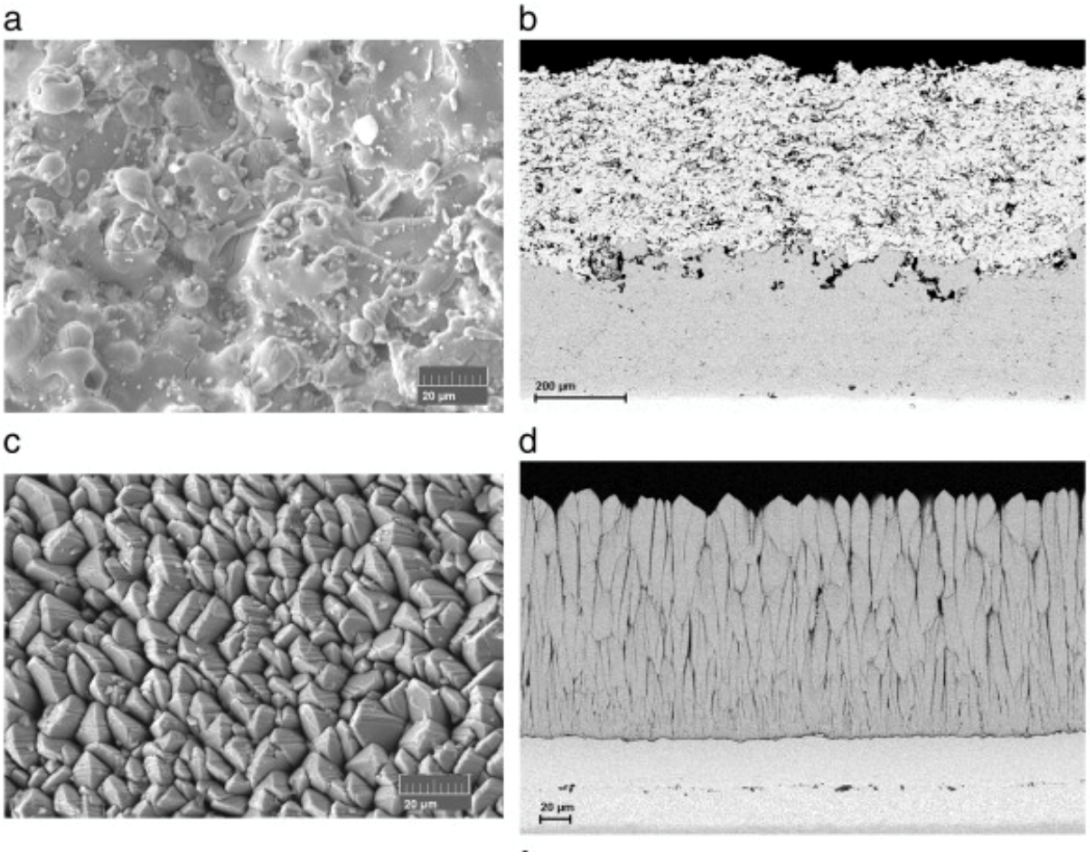

Figure 2.6: Microstructure of typical TBC coatings. Showing (a) the surface and (b) the cross-section of an APS coating. Showing (c) the surface and (d) the cross-section of an EB-PVD coating. Reprinted, with permission, Ref. [91].

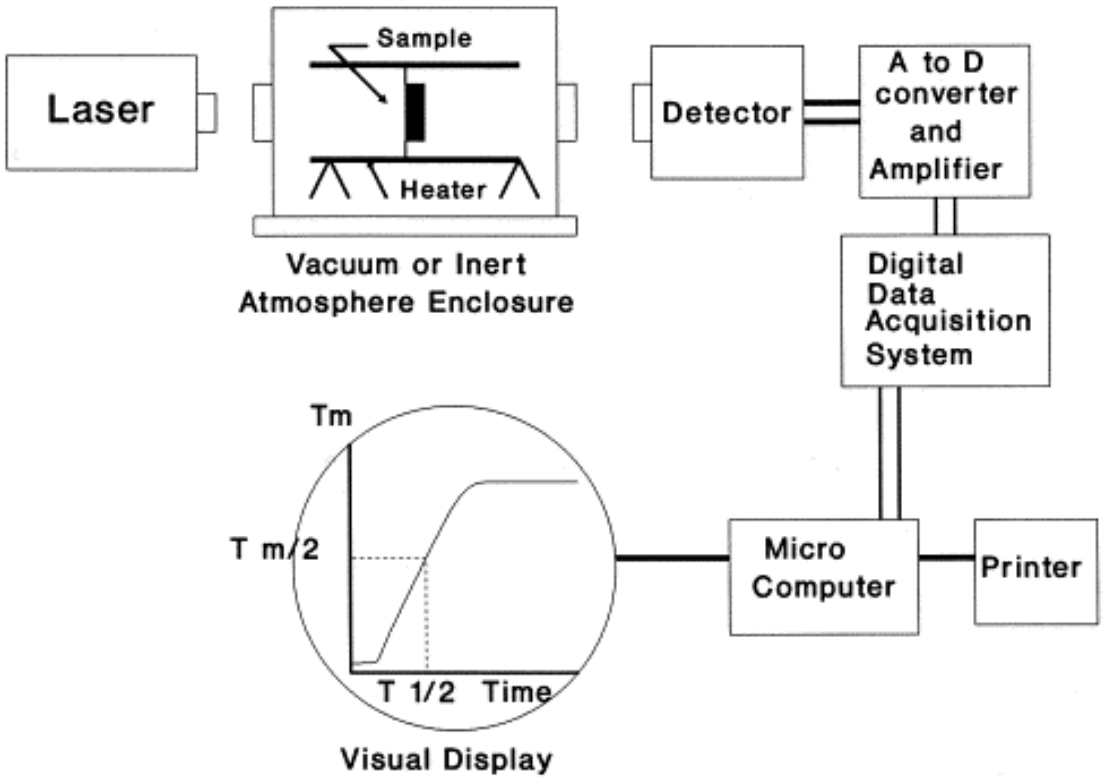

Figure 2.7: Flash Method experimental setup. Reprinted, with permission, from reference [107].

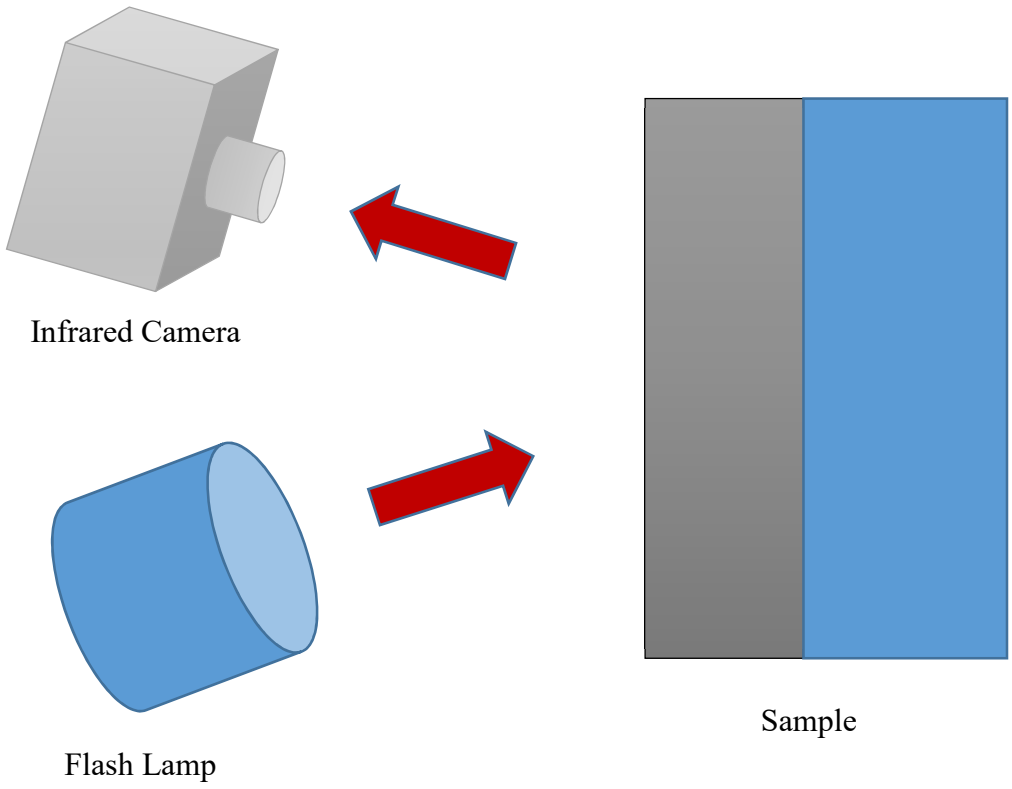

Figure 2.8: Pulsed Thermal Imaging experimental setup with a flash lamp providing the heat source and an infrared camera measuring the thermal response. Figure adapted from US Patent 7769201 B2.

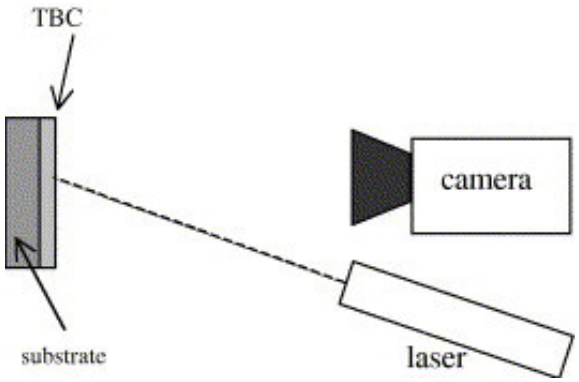

Figure 2.9: Pulsed Thermography method experimental apparatus uses a focused laser heating pulse; the temperature response is measured through thermal imaging. Reprinted, with permission, from Ref. [18].

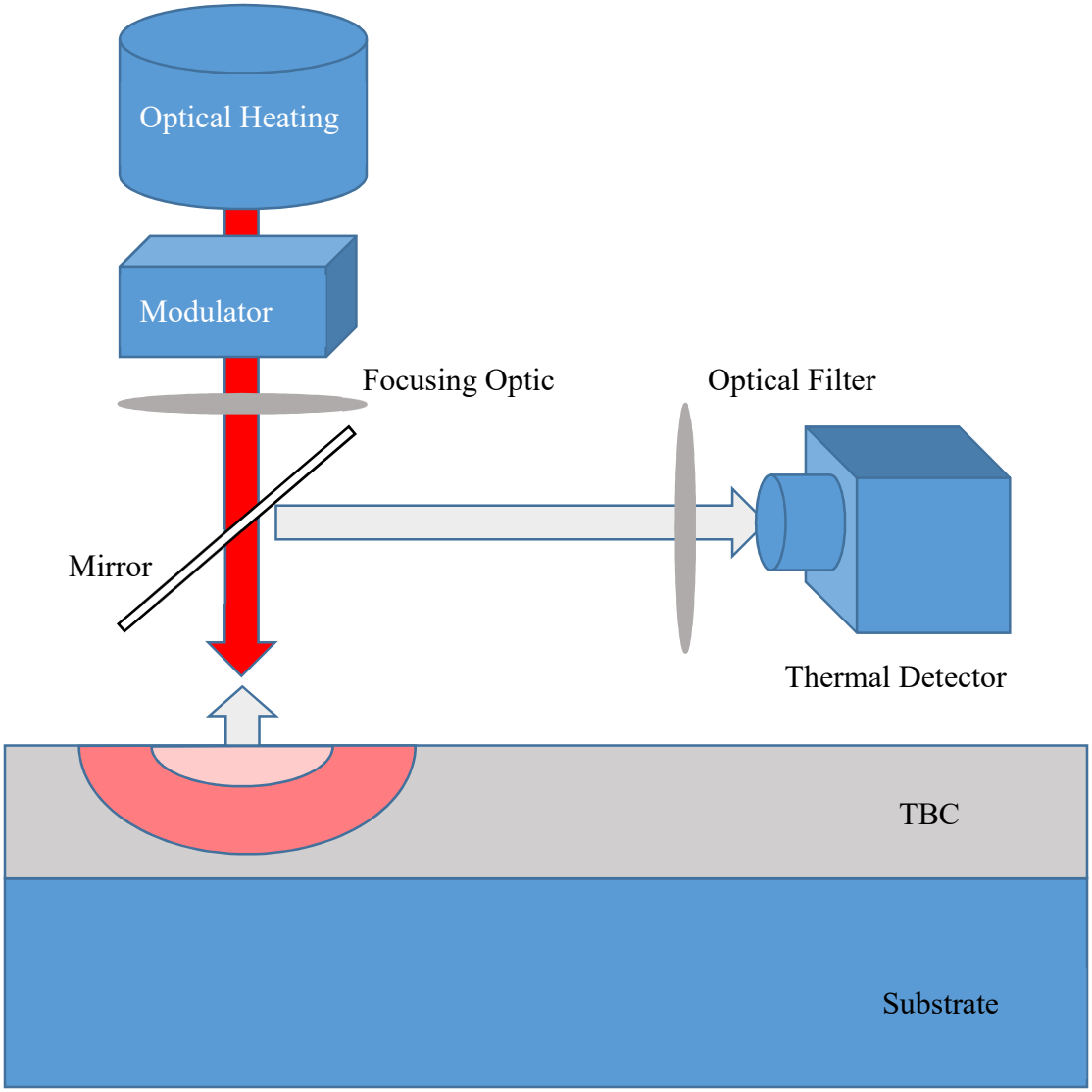

Figure 2.10: PopTea interrogates transient thermal emission from a coating that is heated from an intensity-modulated optical beam. Thermal response is based on the heat transport through the system.

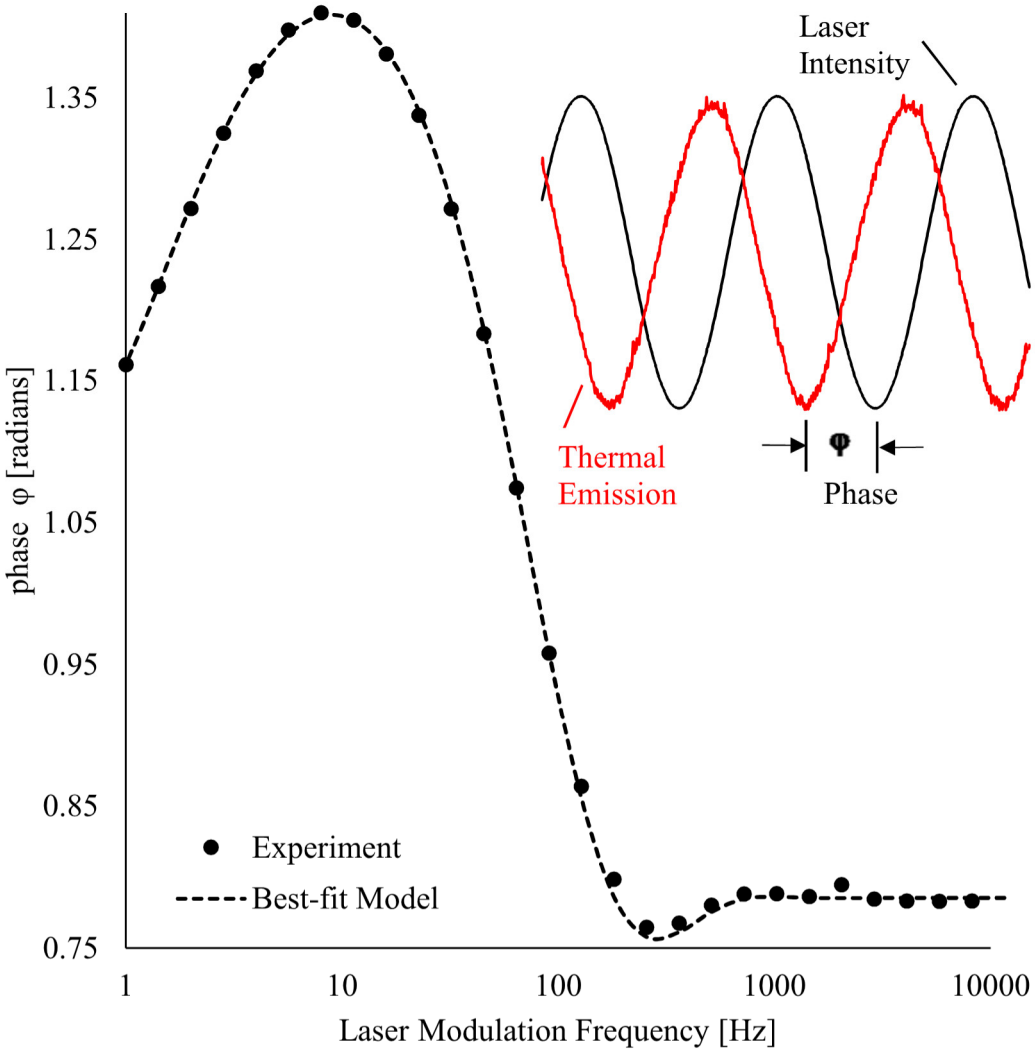

Figure 2.11: PopTea phase of emission experimental data and model best-fit. The harmonic heating and thermal emission are used to evaluate the phase at each frequency.

Chapter 3 Experimental Methods

This chapter describes the experimental apparatus common to the PopTea investigations carried out and reported in Chapter 4, Chapter 5, and Chapter 6. This encompasses a description of the optical heating, thermal detection, and data acquisition system of the PopTea method. Discussion of specific thermal modeling and analysis will be described in subsequent chapters. Similar implementations of this experiment have been described by Yu [108] and Kakuda [109]. The experiment is designed to use focused optical heating to create a harmonically-sustained temperature field in a sample and collect the hemispherical thermal emission centered at the heating point, this is illustrated in Figure 3.1. The optical heating is provided by a laser, the

intensity of the beam is controlled using an opto-acoustic modulator (AOM), and the thermal emission is monitor using a thermal detector and high-speed digitizer.

3.1 Optical Heating

Lasers have been used as a source of thermal heating in a wide-variety of applications, this includes material processing, to laser surgery, and manufacturing [110]. It is widely recognized that lasers are used because they provide a known and consistent level of power, the optical beam can focused to a small region and positioned accurately, and it is simple to automated their control using standard laboratory equipment and software [111]. The laser used for the thermal heating of the samples in the PopTea measurements was an air-cooled Synrad 60 Watt Firestar t-Series laser. The lasing gas was carbon dioxide, CO_2, emitting with a peak wavelength at 10.6 μm . The beam diameter at the output aperture of the optical resonator was 2 mm with less than a 7 milliradians full angle divergence.

3.1.1 Laser Power

The laser power was controlled using a Synrad UC-2000 Universal Laser Controller that provided the pulse width modulation (PWM) signals to the laser. This includes the PWM duty cycle, and PWM frequency. The PWM frequency is the switching rate, and the PWM duty cycle describes the percentage of the period that the laser beam is on and is used to control the time-averaged intensity of the beam. For example, a 25%

duty cycle at a PWM frequency of 20 kHz means that the laser is on for 12.5 μs and off for 37.5 μs.

The Synrad laser can be operated with a range of discrete possible PWM frequencies between 5 kHz and 20 kHz. Selecting the best PWM frequency of the laser was done by using the apparatus illustrated in Figure 3.2; the laser beam response was monitored by using a Judson Teledyne Technologies mercury cadmium telluride (HgCdTe) detector, J15D12-M204-S01M-60. The signal from the detector was amplified using a paired Judson preamplifier PA101 powered with a ±15V power supply. The signal was captured using a Hewlett Packard 54601A Oscilloscope. Sample results from this test are shown in Figure 3.3 that illustrate a small reduction in laser beam ripple by selecting the a high PWM frequency. During this measurement, the laser beam is modulated using an opto-acoustic modulator (AOM, modulator).

In order to observe the effects of PWM frequency on the phase of photothermal emission, a graphite sample was setup as illustrated in Figure 3.1 and was tested at two PWM frequencies at 5 kHz and 20 kHz. The results are illustrated in Figure 3.4 and show no significant change in the phase of photothermal emission. Discussions with Synrad application engineering revealed that increasing the PWM frequency may decrease laser power because the laser cavity temperature is expected to increase. An evaluation of the laser power was completed using a Scientech 100mm Calorimeter, model 380402 using the experimental apparatus described in Figure 3.5. The results, which are summarized in Table 3.1, showed only a 4.8% drop in power from a PWM

frequency of 5 kHz to 20 kHz. Since it appears that increasing the PWM frequency reduces ripple in the modulated beam, there are no significant changes in phase of emission, and only a small drop in laser power was observed, a PWM frequency of 20 kHz was used for the PopTea measurements.

The intensity of the beam should be approximately linear throughout the range of the duty cycle. In order to test the effect of PWM duty cycle on the quality of the modulated laser beam, the laser beam response was measured using an HgCdTe detector as illustrated in Figure 3.2. The results from the test are shown in Figure 3.6; it was expected that the intensity of the modulated laser signal would decrease with a reduction in PWM duty cycle but the results also showed an increase in noise to the modulated laser signal. In order to increase the signal-to-noise and reduce the number of signal averaging necessary, a PWM duty cycle of 99% was used for the PopTea measurements. The laser power delivered to a sample was then controlled using the acoustic-optic modulator.

3.1.2 Laser Power and Stability

Controlling the intensity of the heating requires a precise characterization of the laser power levels and stability. To perform this characterization, the laser power was monitored at 5 and 10 minute intervals with a large-aperture calorimeter for 3 hours, as illustrated in Figure 3.5. The results from a test, performed at a 99% duty cycle, 20 kHz PWM frequency, and 0.50 Volt AOM offset is shown in Figure 3.7. From this

measurement the laser power stabilized after 45 minutes with a time-averaged power level of $10.26\ \mathrm{W} \pm 0.3\%$. This means we can expect a steady and consistent heat flow from the laser beam. However, the laser power measured was time-averaged on the order of several minutes; fluctuations on timescales shorter than 2 minute could not be captured using the large-aperture calorimeter due to its long time constant. The measurements reported here are consistent with the precision of the calorimeter < 1.0%; the accuracy of the calorimeter is specified to be 5%. All PopTea measurements in subsequent work is allowed at least 45 minutes for the laser output to stabilize.

3.1.3 Laser Shape

The optical beam exiting the laser resonator is approximately circular at the aperture and transitions to a Gaussian beam in the mid and far fields. An optical distance of more than the recommended 0.75 meters was used between the resonator aperture and the sample to generate Gaussian heating beam. A traversing knife-edge measurement, as illustrated in Figure 3.8 is used to characterize the quality of the Gaussian beam and the $1/e$ beam radius. Details of the knife-edge measurement technique are described by Araújo [112]; in short, the laser power is measured using a power meter and measurements are taken as the beam is partially blocked by a sharp blade. The results from the power measurements are then fitted to a theoretical power function to resolve the laser beam radius. A well-fitted curve is only possible if the beam has a Gaussian distribution. The limitation to this approach is that it can only

characterize a single axis and requires a long measurement time. The results from a sample measurement using the Scientech Large Aperture Calorimeter are shown in Figure 3.9 and illustrate a high quality Gaussian shape. Changes in the focusing optics and its position were used to control the beam radius.

3.1.4 Acoustic-Optical Modulation

The laser beam intensity was controlled using an IntraAction Model AGM-406B1 Infrared Acousto-optic Modulator (AOM) and the physics of the instrument are detailed in Ref [113]. The modulator is powered and controlled by an IntraAction Model GE-4030 Modulator Driver that takes a low-power voltage input signal from a function generator and generates a high-powered radio frequency (RF) power driver that controls the AOM. The modulator operates using Bragg diffraction to transform a continuous input optical beam into a sinusoidal modulated beam (or any arbitrary function). Details on the physics of Bragg diffraction are explored in references [114]–[117]. For a harmonically modulated beam, defining the offset and amplitude in terms of the normalized RF drive power (P/P_{max}), the laser output power is:

$$\frac{\text{Laser Output Power}}{\text{Laser Input Power}} = \text{offset} + \text{amplitude} \bullet \sin\left(\omega \cdot t\right) \tag{3.1}$$

where, $\omega = 2\pi f$ is the drive modulation frequency. An experiment was setup to determine the linear range of the AOM with respect to its RF drive power; the experiment is illustrated in Figure 3.5. The results from the experiment are presented

in Figure 3.10 and show that the modulator's linear range is from a voltage input of 0.20 V to 0.70 V. Exceeding this linear range results in a degradation of the harmonic laser output as shown in Figure 3.11 when tested using the experimental apparatus described in Figure 3.2.

3.2 Thermal Emission

The thermal emission was collected using a hemispherical elliptical mirror. An elliptical mirror is used because it redirects beams between its two focal points, an illustration is shown in Figure 3.12. One focal point was placed at the center of the heating beam on a sample, after it passes through the mirror aperture, and a thermal detector was placed at the second focal point. This allowed the redirection of the thermal emission to an Indium Antimonide (InSb) thermal detector. This detector was chosen for its high sensitivity at $3-5\,\mu m$ and its exclusion of the $10.6\,\mu m$ laser wavelength. The detector signal was amplified using a photodiode transimpedence preamplifier and monitored using a National Instruments PCI-5112 high-speed digitizer with an internal synchronization signal. This signal was used to synchronize the function generator, AOM, and the high-speed digitizer.

Signal averaging at each AOM modulation frequency was used to increase the signal-to-noise ratio of each measurement. The data acquisition system was designed to report a single file for each measurement that contained six-waveforms of the signal-averaged function generator signal, which represented the laser signal, and the InSb

thermal detector signal. Fitting a sinewave to each of these two signals was used to determine the phase lag of the thermal emission with respect to the laser signal. An illustration of the two signals and a phase-spectrum sweep that was generated by taking measurements at various AOM modulation frequencies are shown in Figure 3.13.

3.3 Sample Mount

There were two types of samples mounts used in this dissertation. They are described as either a heated stage or an adiabatic "low-contact" holder. The heated stage is a large thermal mass (steel) that is held at a constant temperature using a PID controller and an embedded thermocouple. This heated stage facilitated measurements in which the rear temperature of the TBC system and substrate were maintained at a constant temperature. An illustration of this stage is shown in Figure 3.14.

The adiabatic "low-contact" holder consists of a vacuum chuck, formed from a Swagelok fitting, which contacts the outer boundaries of the sample. The vacuum held the sample in place and the low contact area of the front ferrule of the fitting minimized heat loss through the rear contact with the sample. Several mounts were created for testing samples of various diameters. An illustration showing the mounting hardware is shown as Figure 3.15.

Figures and Tables

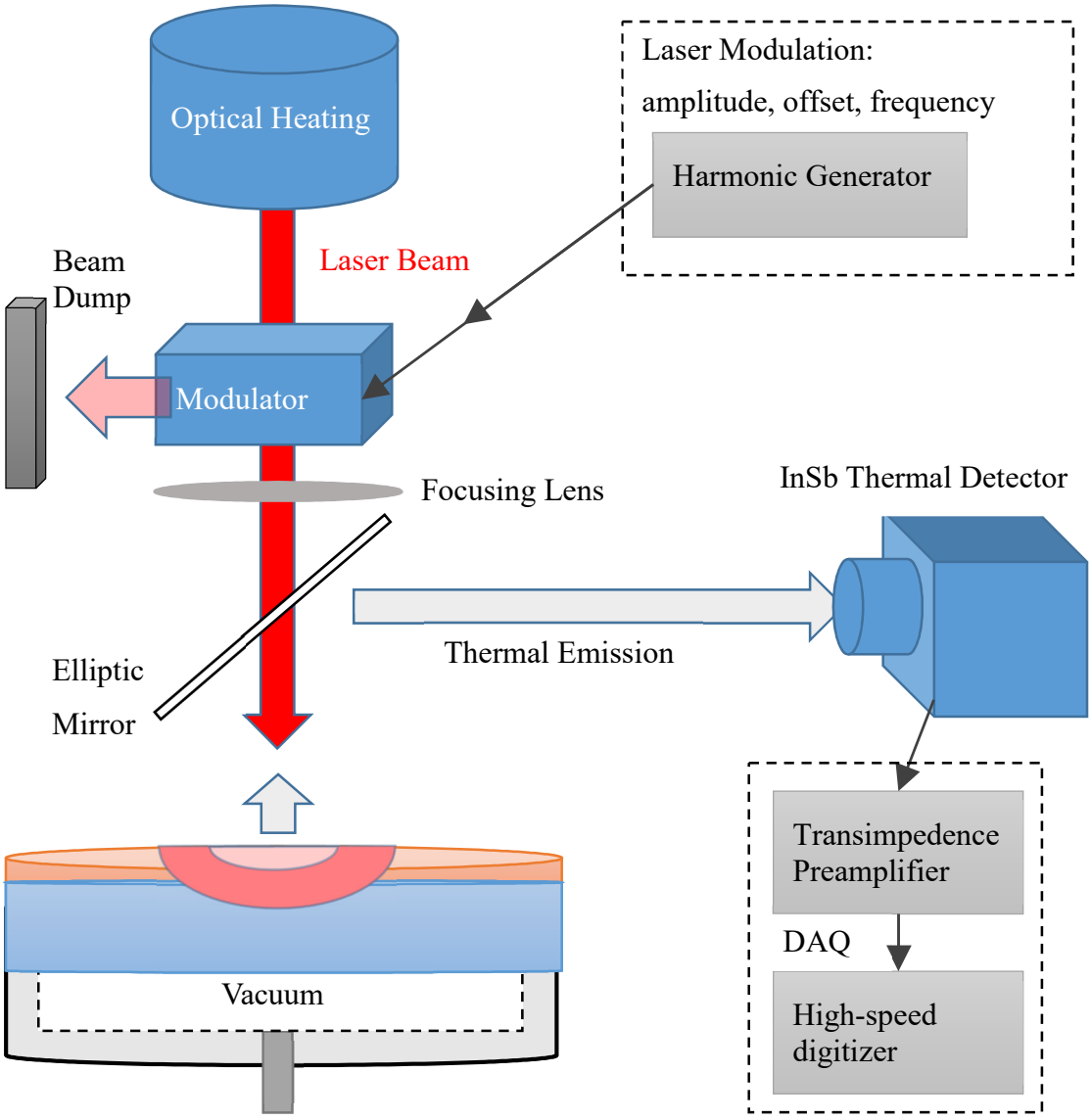

Figure 3.1: Phase of Photothermal Emission Analysis (PopTea) method, experimental apparatus.

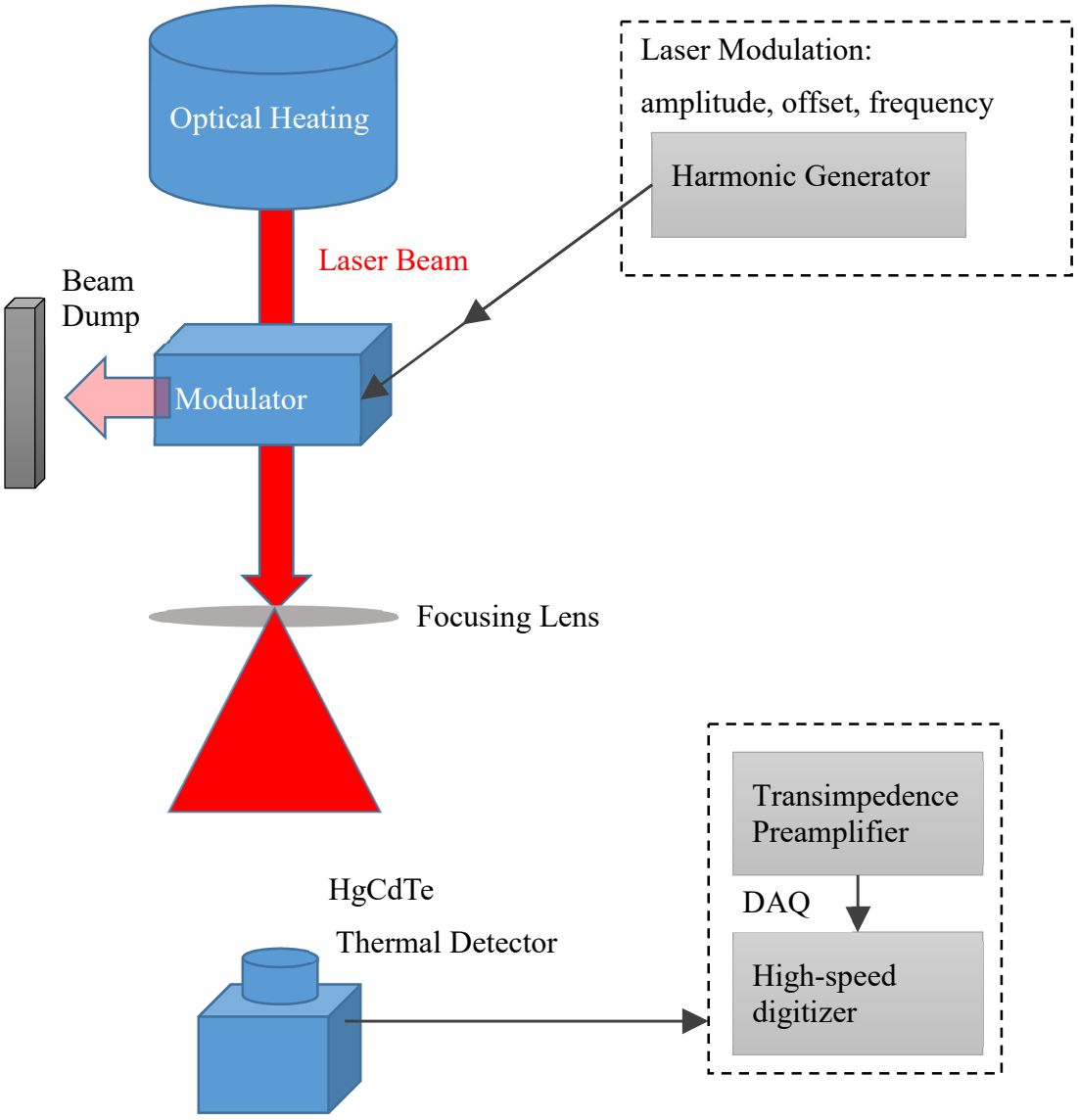

Figure 3.2: Laser Characterization, experimental apparatus.

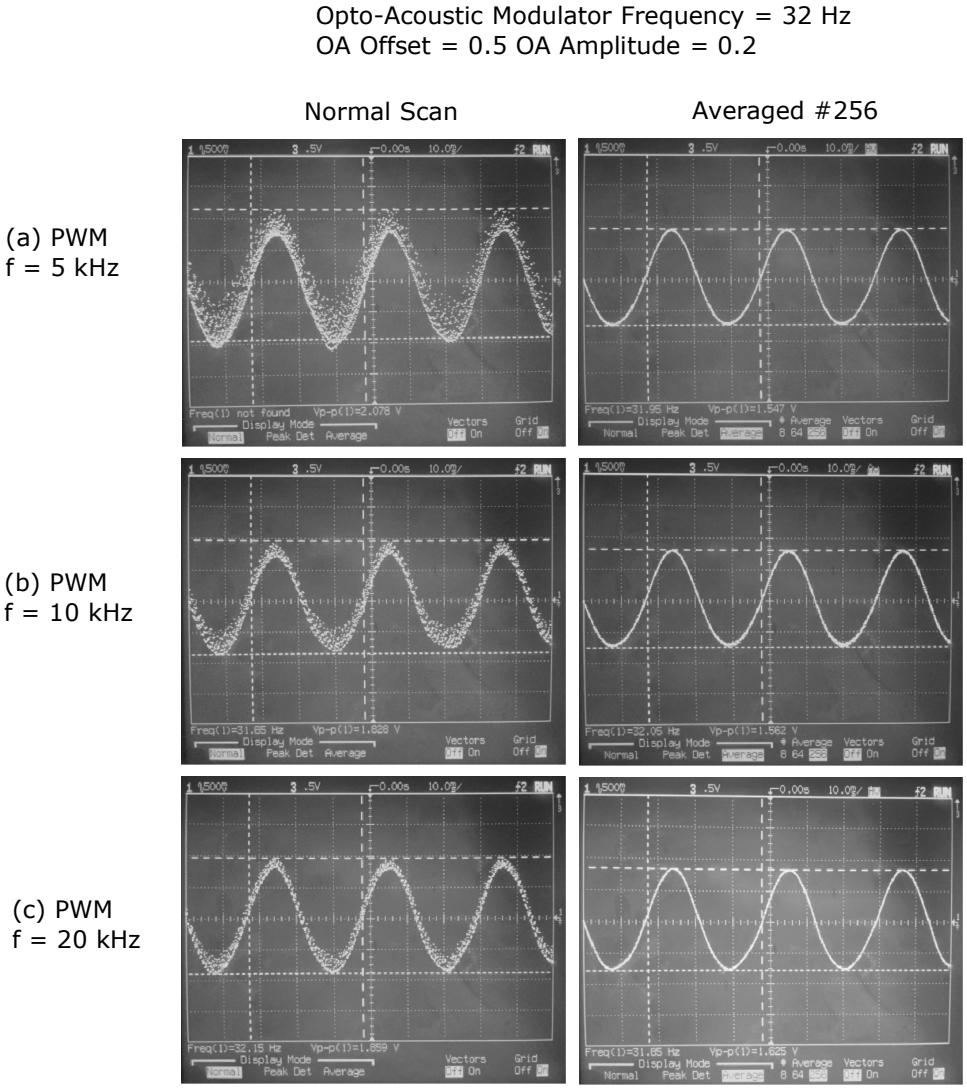

Figure 3.3: Laser detector was used to monitor changes in the modulated laser signal due to changes in the PWM frequency. The first column represents a single waveform and the second column has been signal averaged for 256 waveforms. Increased PWM frequency reduced ripple in the laser signal.

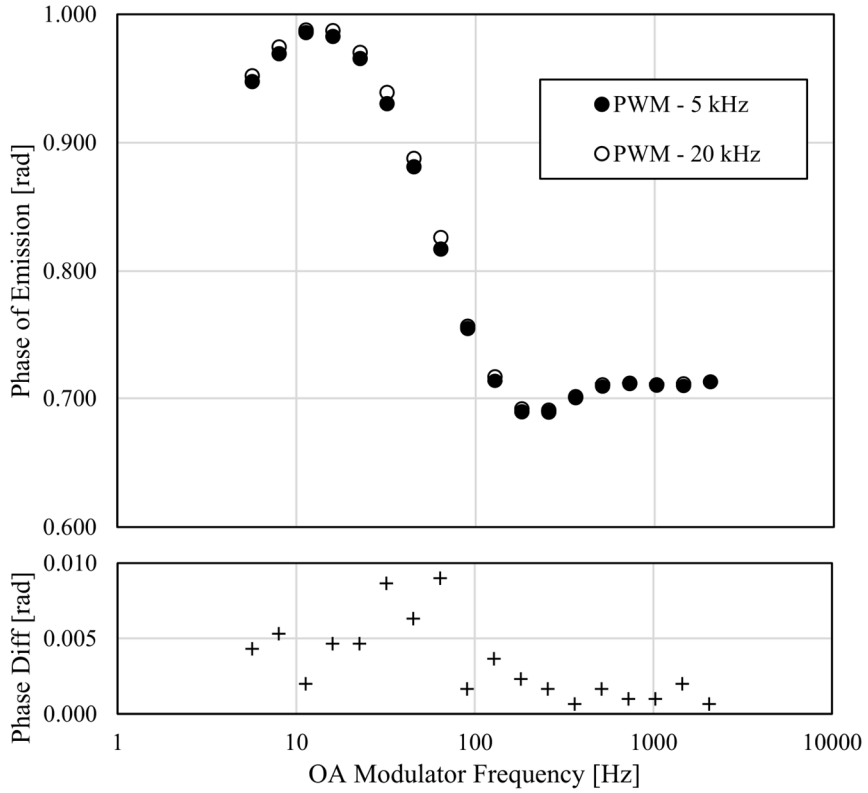

Figure 3.4: Phase of Emission relationship to changes in PWM frequency. The PWM duty cycle is 99%.

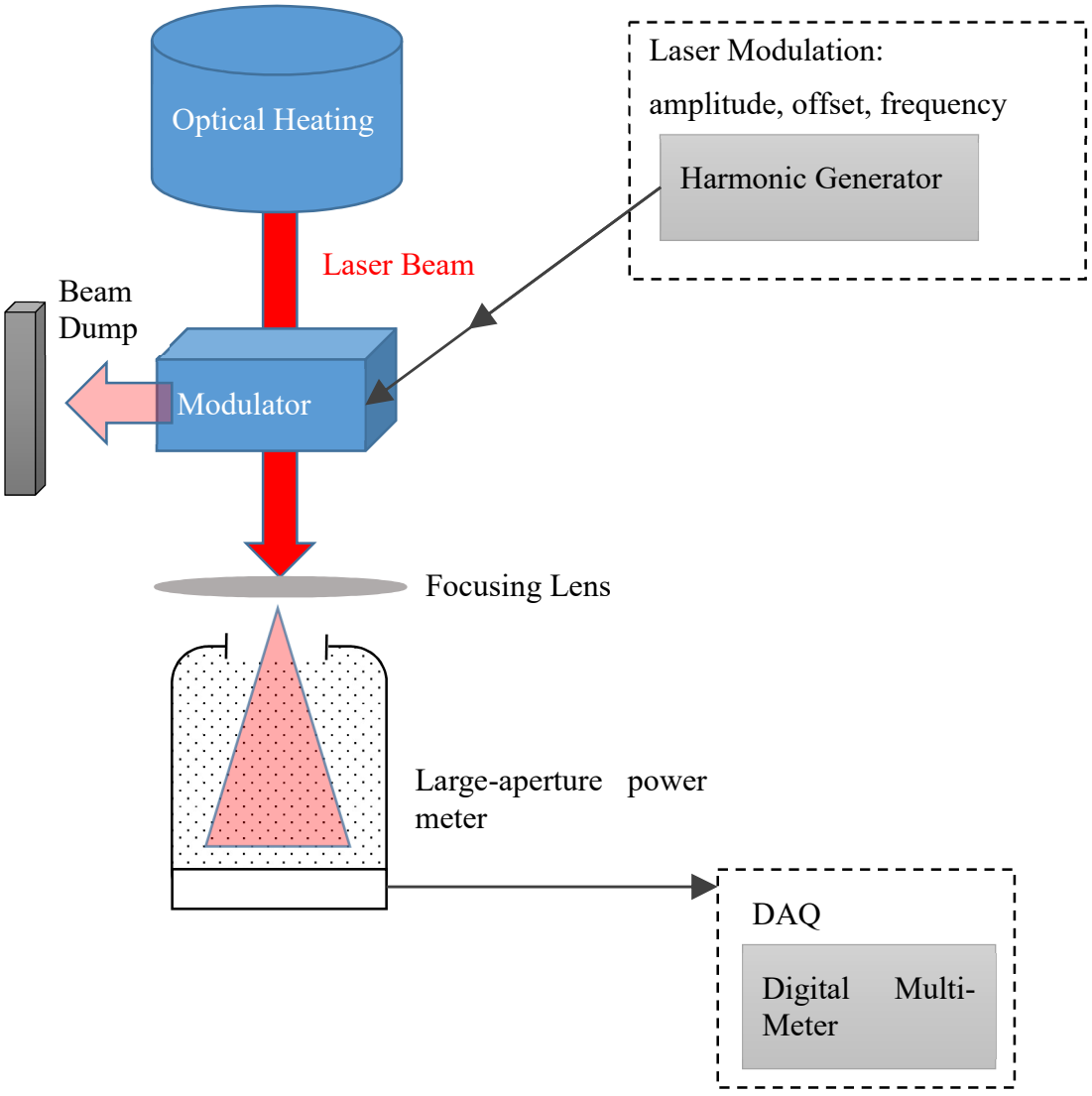

Figure 3.5: Laser power experimental apparatus; a Scientech 100mm Calorimeter, Model 380402 is used to evaluate the laser power.

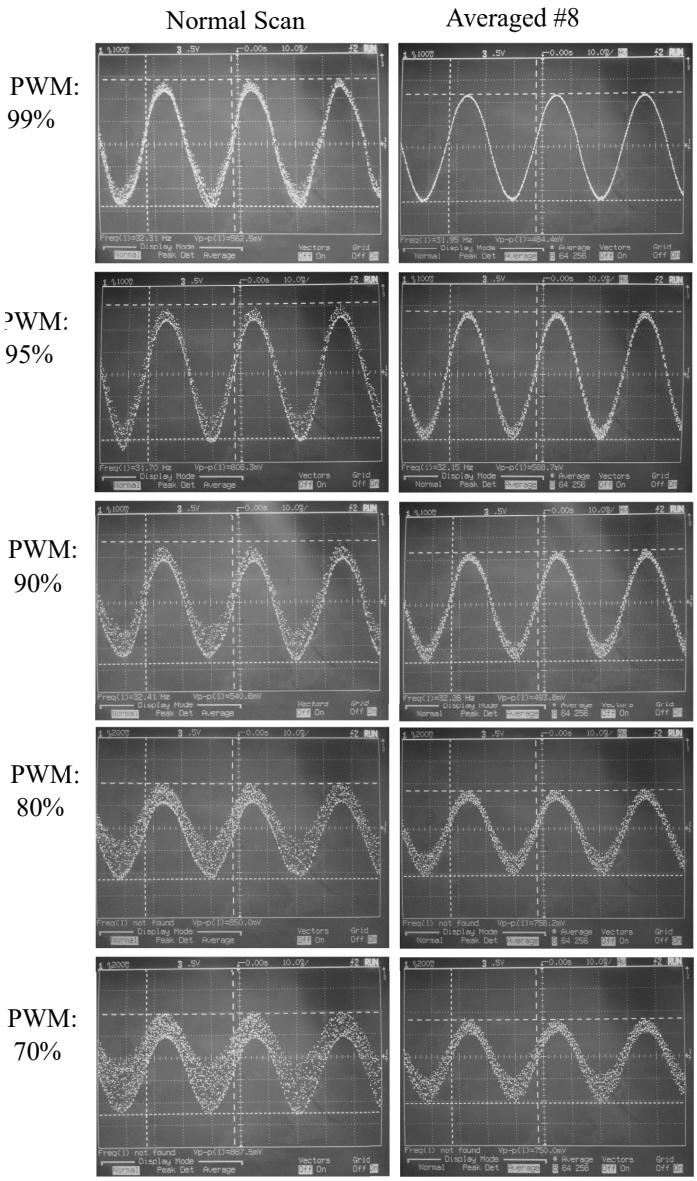

Figure 3.6: Reducing the PWM duty cycle degrades the sinusoidal modulation of the laser. The first column is a single scan and the second column is averaged over 8 waveforms. The AOM settings are 0.3 V offset, 0.1 V amplitude, at 32 Hz. The PWM frequency is 20 kHz.

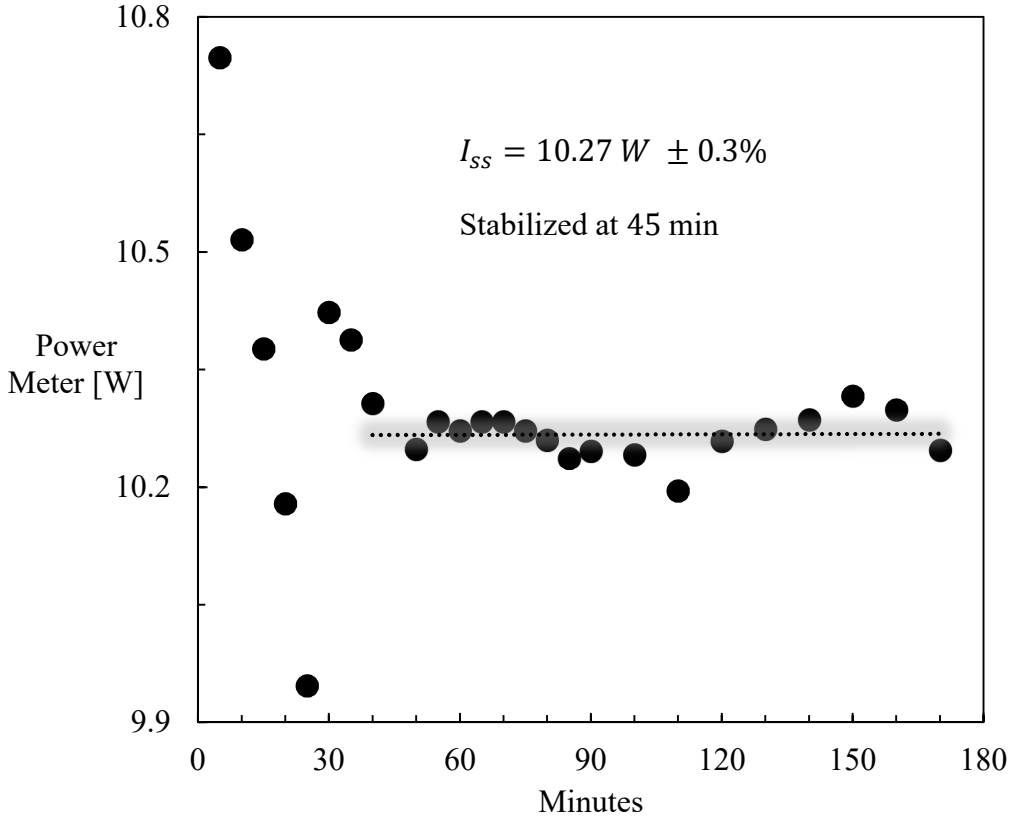

Figure 3.7: Laser stabilization power test taken at 5 minute and 10 minute intervals using experimental apparatus illustrated in Figure 3.5.

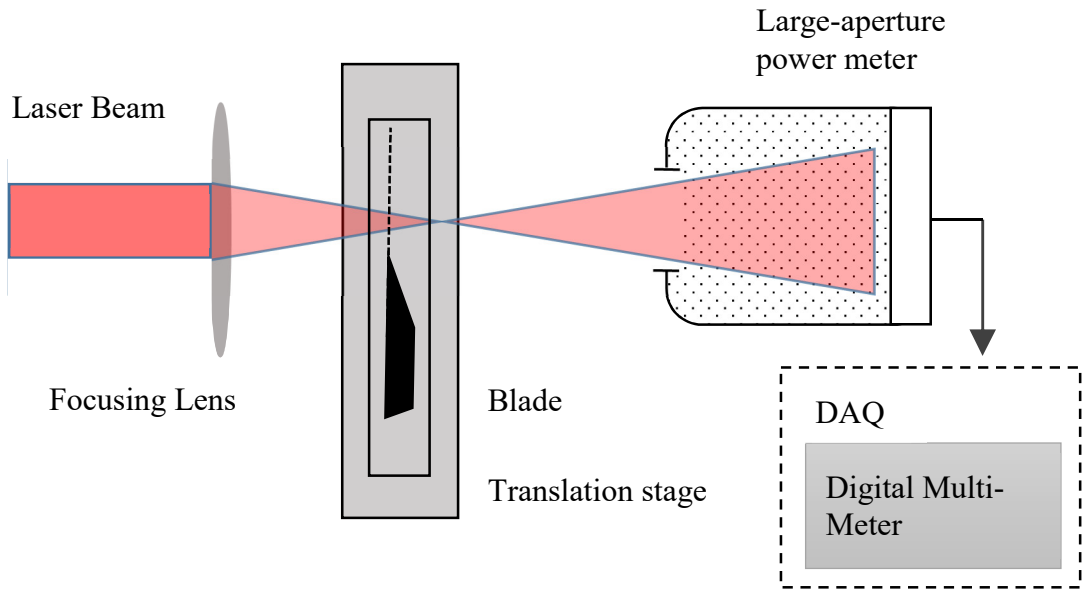

Figure 3.8: Knife-edge technique experimental apparatus for beam shape characterization. Figure adapted from Ref. [112] .

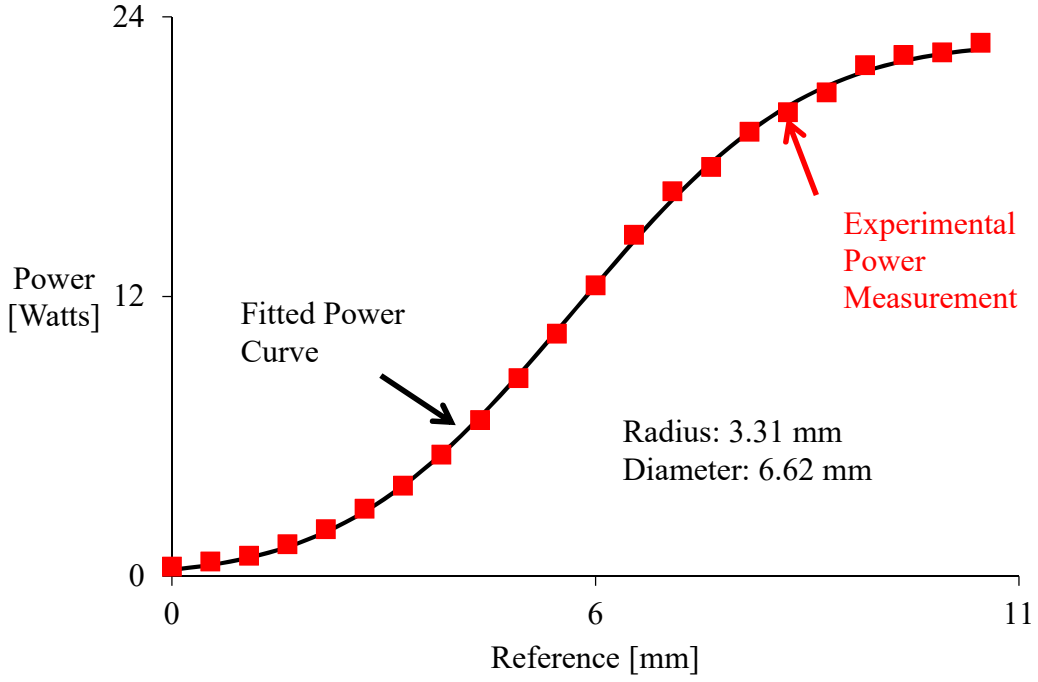

Figure 3.9: Knife-edge measurement for characterizing beam shape and radius using experimental apparatus illustrated in Figure 3.8.

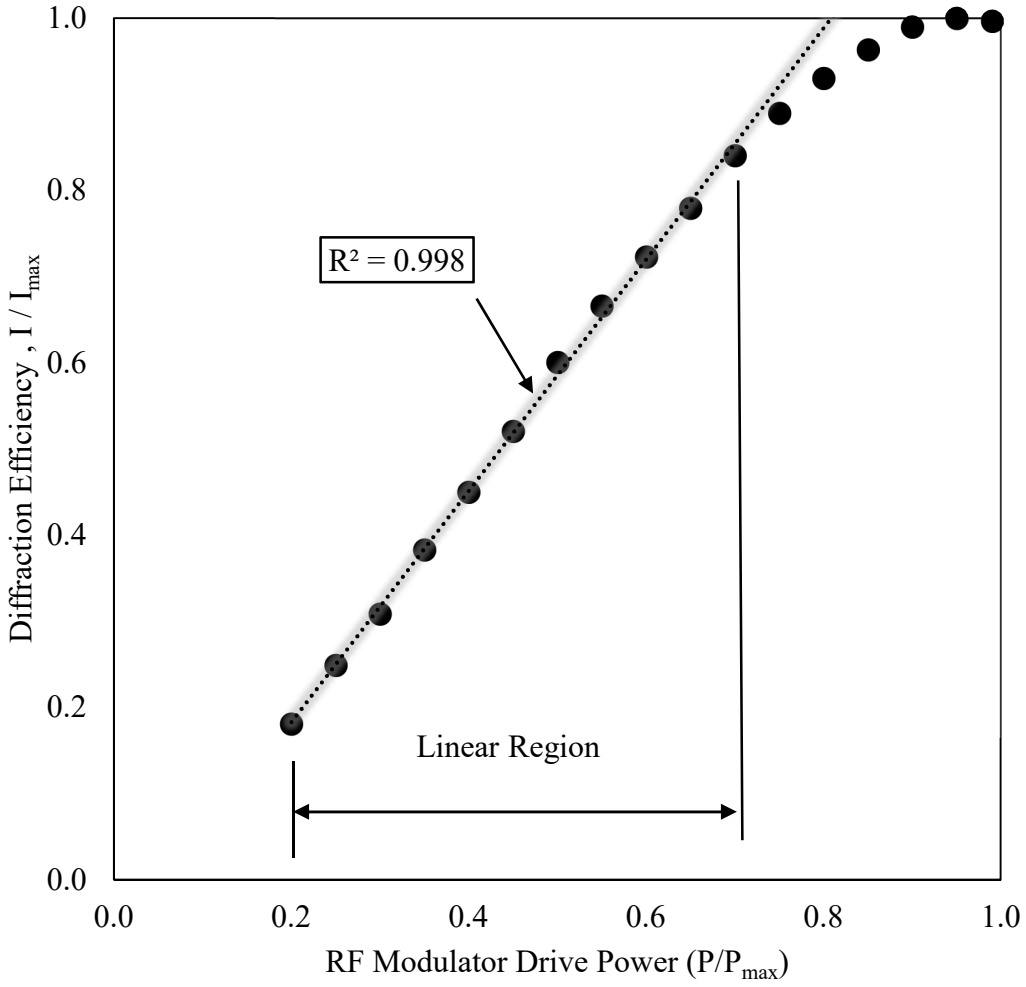

Figure 3.10: AOM Diffraction Efficiency is linear from a modulated drive power of 0.20 V to 0.70 V, evaluated using experimental apparatus illustrated in Figure 3.5.

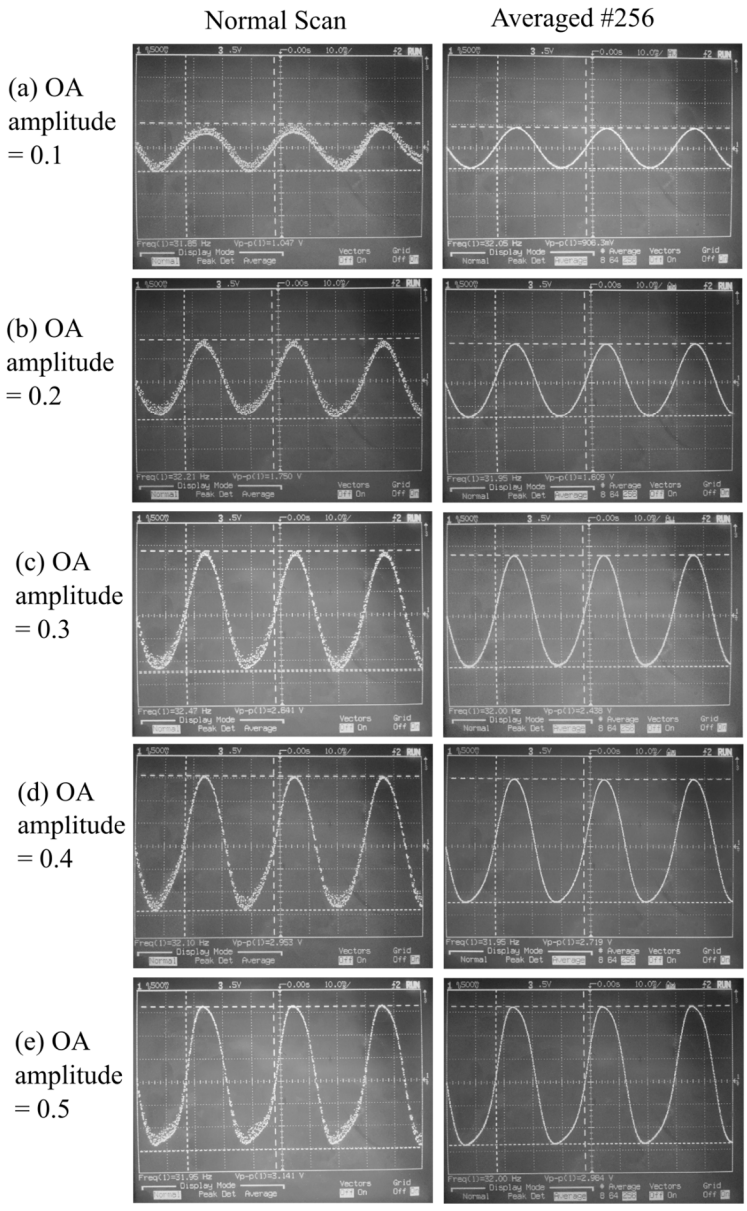

Figure 3.11: AOM nonlinearity affecting sinusoidal waveform was observed using experimental apparatus illustrated in Figure 3.2. The offset was 0.50 V to AOM.

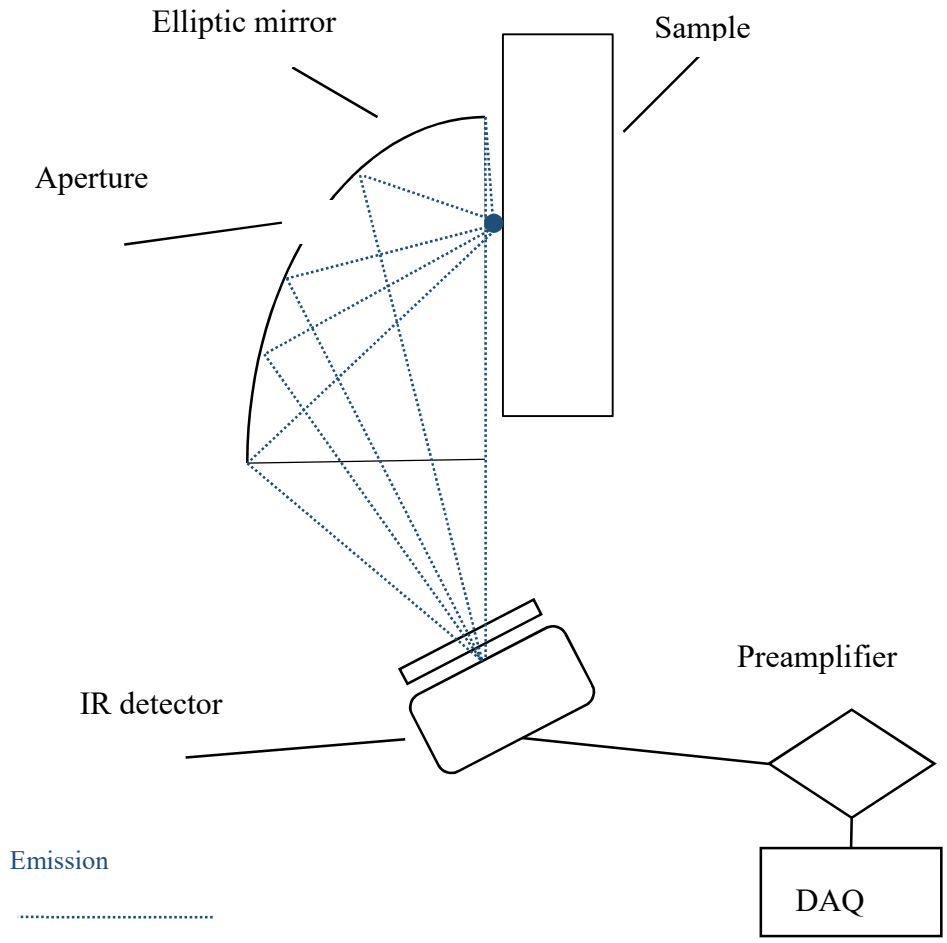

Figure 3.12: Thermal emission detection system using a hemispherical elliptic mirror.

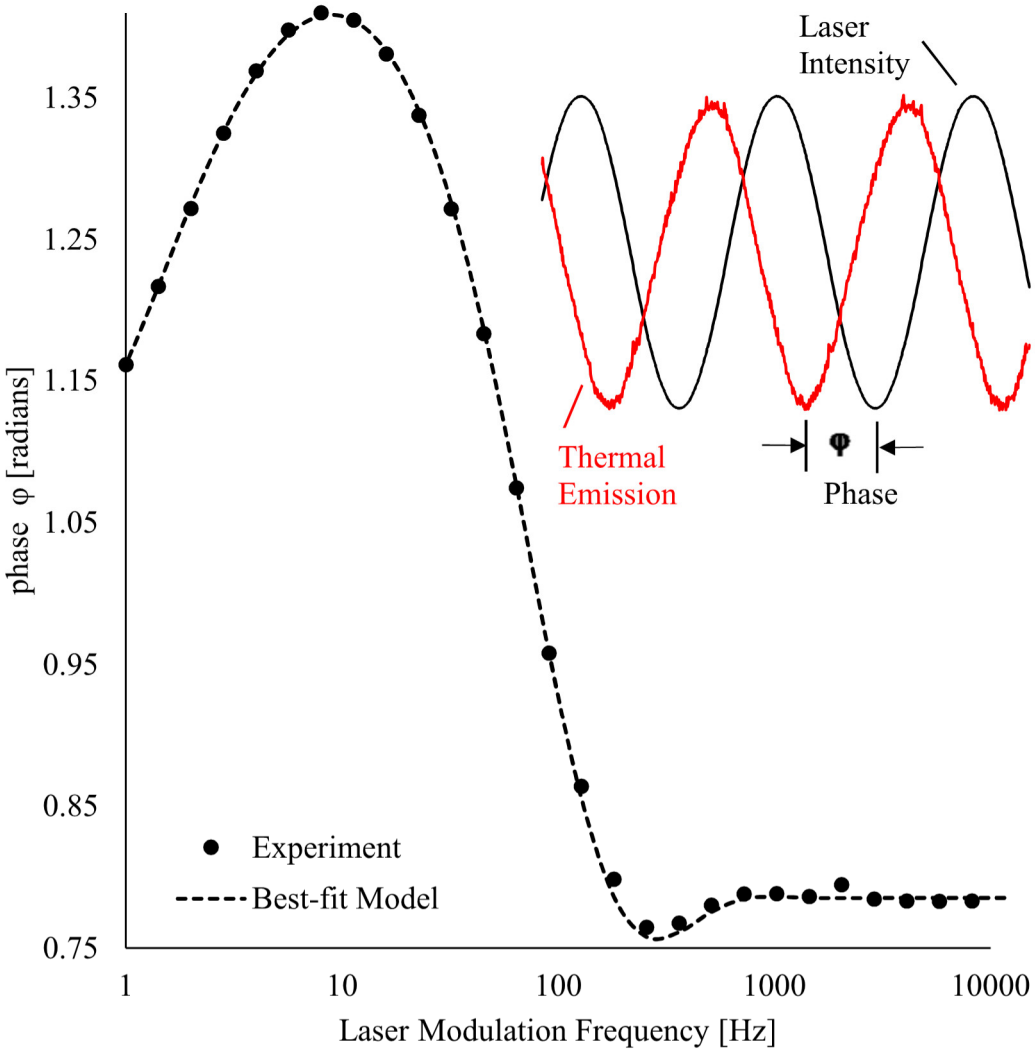

Figure 3.13: Phase spectrum as laser modulation frequency changes.

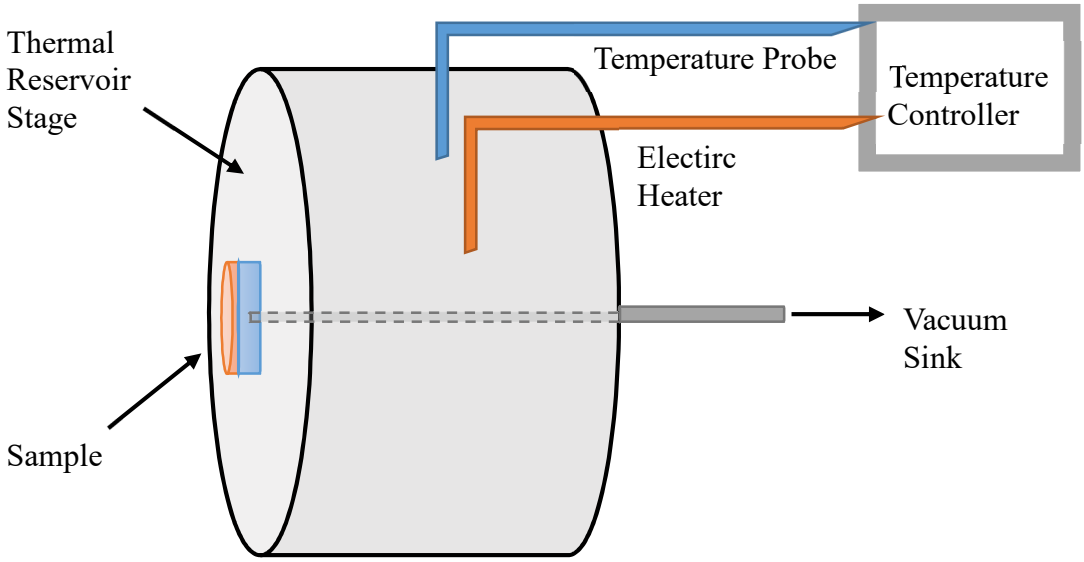

Figure 3.14: Sample mount for a semi-infinite and temperature controlled rear boundary condition.

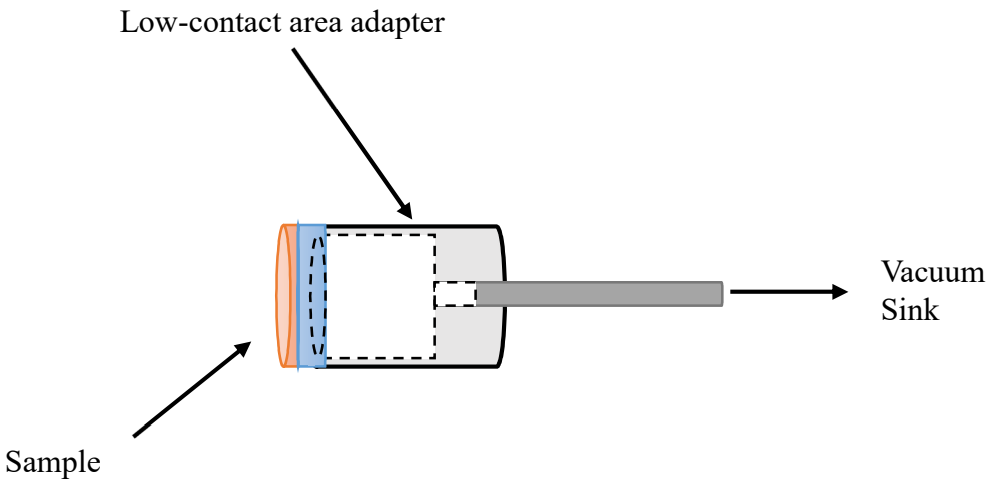

Figure 3.15: Sample mount for an adiabatic rear boundary condition.

Table 3.1: Drop in power level due to an increase in PWM modulation frequency.

PULSE WIDTH MODULATION FREQUENCY	POWER [W]	REDUCTION IN INTENSITY FROM 5 KHZ
5 KHZ	19.23	-
10 KHZ	18.50	3.88%
20 KHZ	13.31	4.80%

Chapter 4 Differential Phase of Photothermal Emission Analysis for Thermal Barrier Coatings

4.1 Introduction

Thermal imaging techniques generally attempt to characterize the thermal properties of materials by using the transient surface thermal emission that results from an applied heat input (often in the form of a pulse). Most applications of these techniques have not entered the realm of quantitative thermal property measurements. Instead, they have focused on seeking qualitative coating information that can reveal "defects" in the subsurface material [85], [118], [119]. However, one application

offering significant reward for overcoming the challenges of making quantitative thermal property measurements is the thermal barrier coating.

Thermal barrier coatings (TBCs) are applied to metallic components in aerospace and power turbines to provide thermal and environmental protection [24]. Typical topcoats for TBCs are zirconia-based ceramics that can be deposited by a variety of methods, including air plasma spray (APS) and electron beam physical vapor deposition (EB-PVD). Coating thicknesses can range from $100\,\mu m$ to greater than $2\,mm$, depending on the application. In turbine engines, the structural metal under these coatings are often superalloys exhibiting excellent mechanical strength and creep resistance at high temperatures [120], [121]. A bond coat, underlying the topcoat, is required to protect the superalloy from oxidation and hot corrosion attack and to form an adherent oxide surface for the topcoat [122].

Achieving and sustaining the designed performance of a TBC is necessary to realizing a predictable life operation or "prime reliance" of the coating [6]. Consequently, the ability to quantitatively characterize the heat transfer performance of coatings is fundamental to the goal of attaining prime reliance. Despite its vital nature, in practice the desired level of thermal characterization in TBC production and service is currently unattained because of the inability of conventional techniques to measure coating thermal properties on engine hardware. Thermal imaging has been employed to detect delamination of coating materials [98]. However, mechanical failure of the coating is only one aspect of a TBC's "health" that indicates approach to

end of life. For prime reliance, a more complete and quantitative picture of the thermal performance of a coating is required that goes beyond detecting imminent catastrophic failure.

Two techniques have recently emerged that address the issue of making quantitative thermal property measurements of TBC topcoats: Pulsed Thermal Imaging (PTI) [123] and Phase of Photothermal Emission Analysis (PopTea) [20]. Both techniques exploit the thermal contrast between the coating and substrate material to measure two independent thermal properties of the coating. This allows both the thermal diffusivity and thermal conductivity (and volumetric heat capacity) to be established. The primary differences between these techniques are that in PTI analysis the thermal response to a heating pulse is conducted in temporal space, while in PopTea the thermal response to periodic heating is measured and analyzed in frequency space. In both measurements, thermal emission is used to evaluate the thermal response of the coating to heating. PTI uses optical coatings to confine radiative heating and emission to the surface of the sample. In contrast, PopTea does not require optical coatings, in which case thermal emission is interpreted as a volumetric signature of thermal transport through the coating system. Although both methods can measure coating properties on coupon samples, measurements on an actual engine blade has only been demonstrated in the open literature with PopTea [102]. Additionally, PopTea has been used to investigate the consequence of service related changes to coatings thermal properties resulting from high temperature exposure [101] and foreign material infiltration [100].

4.2 Need for differential PopTea measurements

In coating property measurements, it is often appropriate to assume that the thickness of the substrate material is significantly greater than the coating material. In the case of conventional PopTea measurements, the critical assumption is that the substrate material behaves as though it is semi-infinite. In practice, this assumption requires that the transient heat transfer does not extend beyond the thickness of the substrate material, and thereby does not interact with any underlying interface. To assess this requirement, there are two measures of thermal penetration depth that must be compared, one in the coating and one in the substrate. The substrate material thermal penetration depth is related to the coating value by a constant multiplier: $\sqrt{\alpha_{sub}/\alpha_{coat}}$, where α_{sub} and α_{coat} are the thermal diffusivities of the substrate and coating, respectively. For typical coating-superalloy combinations, this multiplier is approximately three. Therefore, the assumption of a semi-infinite substrate material will require that the substrate material be at least three times as thick as the TBC topcoat. Some engine parts may not satisfy this requirement. For example, some parts in the high temperature gas stream are hollow and contain cooling channels to support film cooling [124]. Additionally, when the function of the part is not primarily load bearing, coated solid-wall parts may be relatively thin. Therefore, it should be expected that some thermal property measurements of coated parts will involve heat transfer scales that are deeper than a well-defined region of the substrate material.

Unfortunately, it is prohibitively difficult to provide a well-characterized picture of heat transfer beyond a certain thickness associated with the wall of a coated part. To address this issue, a "differential" technique is developed in this paper for PopTea measurements. The goal is to be able to extend thermal property measurements to a wider range of coated part conditions found in gas turbine engines.

Differential techniques applied to thermal property measurements methods incorporates measurements from two thermal systems that are the same except for one distinguishing “differential” thermal element. The first set of measurements serves as a reference system; a change to the thermal system is made and the contrast against a second set of measurements are used to learn from the distinguishing or differential thermal element.

Differential techniques that address unknown characteristics in measurements are ubiquitous to thermal property measurements. For example, a large family of differential scanning calorimetry (DSC) methods have been developed that can be categorized as either heat-flux DSCs or power-compensated DSCs [125], [126]. The heat-flux DSC approach measures the difference in temperature of a reference and a test sample for a given heat flux. The difference in temperature between the sample and a reference is used to resolve the heat capacity of the sample. The power-compensated approach sets a reference and a sample in two different chambers that are maintained at a constant temperature. The difference in thermal power needed to maintain a constant temperature is used to resolve the heat capacity. These two examples illustrate

how differential techniques can be used to make highly sensitive measurements by removing the thermal effects common to both the reference and sample thermal system. External effects such as thermal radiation, convection, any other thermal interactions with the environment can be then encapsulated and accounted for in the modeling.

Use of differential methods have been implemented for modulation-based thermal conductivity measurement methods. The 3ω method requires a metal wire imbedded in the test sample. In the case of semiconducting samples, an additional dielectric insulation layer is sandwiched between the metal wire and the sample to prevent current leakage. Ideally, this layer would be thin enough to be an electrical insulator without contributing to thermal resistance. However, Venkatasubramanian found it necessary to develop the differential 3ω method to account for thermal resistance in measuring the thermal conductivity in superlattice structures, Bi_2Te_3/Sb_2Te_3 [127]. Further use of differential 3ω have been studied by Borca-Tascius [128], [129], Jacquot [130], and Kudo [131].

Likewise, the goal of differential PopTea will be to remove most of the impact of unknown heat transfer characteristics (beyond a critical thermal penetration depth) from the interpretation of measurements used to determine coating properties. Therefore, in differential PopTea measurements, some aspects of heat transfer into the substrate system must be learned through the measurement. This contrasts with conventional PopTea measurements, where it is assumed that there is nothing to be learned about heat transfer into a semi-infinite body underlying the coating.

The development of differential PopTea measurements requires implementation of a "sub-substrate system" (which will be referred to as the "subsystem" for brevity). The subsystem is incorporated into the overall heat transfer model along with strategies for measuring variables associated with this subsystem. The subsystem is defined as the extent of material beyond a well-defined thickness L_{sub} associated with the wall of the coated part. The goal of introducing the subsystem is not to fully describe the heat transfer beyond the length scale of L_{sub}. Rather the goal is to minimize the significance of the heat transfer characteristics associated with thermal penetration depths exceeding the substrate thickness by developing a suitably generic subsystem model.

To this end, a subsystem model illustrated Figure 4.1 is proposed to describe heat transfer in the low frequency limit of PopTea measurements. The subsystem model characterizes a thermal mass beyond the substrate material. This added mass is semi-infinite and has two effective thermal properties that need to be determined in the measurement, thermal conductivity and heat capacity. Additionally, the subsystem model includes a thermal contact resistance R_{SS} which may exist between the substrate and the added mass. Therefore, the subsystem model contains three heat transfer variables that are fitted in differential PopTea measurements. These thermal properties are only “effective” properties associated with the subsystem model because the point of the subsystem is only to mimic the behavior of heat transfer characteristics at scales greater than L_{sub}. The most direct strategy for determining the unknown effective

properties of the subsystem is through two sets of PopTea measurements. The first measurement can be performed on an uncoated sample and the second measurement performed after the coating is applied. This approach decouples the task of determining the unknown thermal transport properties of the subsystem from the coating. For application of this approach to engine hardware, this requires an uncoated part to be available for reference measurements. A second strategy utilizes a single PopTea measurement to determine the variables of the substrate system as part of the task of resolving the coating thermal properties. However, the risk associated with a single PopTea measurement is in the loss of uniqueness with respect to determining the coating thermal properties.

4.3 Model of heat transfer through coating, substrate, and subsystem

In terms of the dimensionless spatial variables, the axisymmetric two-dimensional conduction equation for an anisotropic medium in cylindrical coordinates is:

$$\left(\frac{L_{coat}}{R_{heat}}\right)^2\left(\frac{\partial^2 T}{\partial r^2}+\frac{1}{r}\frac{\partial T}{\partial r}\right)+\frac{\partial^2 T}{\partial z^2}-\frac{L_{coat}^2}{\alpha}\frac{\partial T}{\partial t}+S\left(z,t\right)e^{-r^2}=0 \qquad (4.1)$$

The radial coordinate r is made dimensionless by the $1/e$ 1 radius of the Gaussian heating beam R_{heat}, while the axial coordinate z is made dimensionless by the coating thickness L_{coat}. Far from the source of heat, the temperature field approaches the

ambient value of T_∞. Therefore, to simplify the boundary conditions, the conduction equation will be used to determine the relative temperature T above the ambient, such that the absolute temperature is given by $T+T_\infty$. The heat equation will be used to describe heat transfer in three layers, comprising of: the coating $\left(0\le z<1\right)$, the substrate $\left(1\le z<1+Z_{sub}\right)$ and the subsystem $\left(z\ge 1+Z_{sub}\right)$. The dimensionless substrate thickness is defined as $Z_{sub}=L_{sub}/L_{coat}$. All three layers are assumed to be spatially homogeneous and isotropic. The axial heating function in the conduction eq. (4.1) is given by:

$$S(z,t)=\begin{cases} z<1 & \dfrac{L_{coat}^2}{k_{z,coat}\delta_{opt}}\left[I^+\left(0\right)\cdot e^{\frac{-z}{\delta_{opt}/L_{coat}}}+\Re_1\cdot I^+\left(1\right)\cdot e^{\frac{z-1}{\delta_{opt}/L_{coat}}}\right] \\ z\ge 1 & 0 \end{cases} \tag{4.2}$$

where $I^+(0)$ is the heating radiosity traveling into the coating from the surface, and $I^+(1)$ is the radiosity approaching the interface with the substrate. These radiosities are evaluated from:

$$I^+\left(0\right)=I_o\left(t\right)\cdot\left(1-\Re_0\right)\cdot\left[1+\frac{\Re_0\cdot\Re_1\cdot e^{-\frac{2L_{coat}}{\delta_{opt}}}}{1-\Re_0\cdot\Re_1\cdot e^{-\frac{2L_{coat}}{\delta_{opt}}}}\right] \tag{4.3}$$

$$I^{+}(1)=\frac{I_o(t)\cdot(1-\Re_0)\cdot e^{-\frac{L_{coat}}{\delta_{opt}}}}{1-\Re_0\cdot\Re_1\cdot e^{-\frac{2L_{coat}}{\delta_{opt}}}} \tag{4.4}$$

At the wavelength of heating, the reflectivity of the surface is $\Re_0$, the reflectivity of the substrate is $\Re_1$, and δ_{opt} is the optical penetration depth of heat into the coating material. These radiosities account for multiple reflections between the coating surface, but do not account for interference effects. The first four boundary conditions to be imposed on the relative temperature solution to the heat equation are:

$$\begin{aligned}
\left.\frac{\partial T}{\partial r}\right|_{r=0} &= 0 \\
T(r\to\infty) &= 0 \\
\left.\frac{\partial T_{coat}}{\partial z}\right|_{z=0} &= 0 \\
T_{ss}(z\to\infty) &= 0
\end{aligned} \tag{4.5}$$

The present solution will assume negligible thermal resistance at the interface between the coating and the substrate, such that:

$$\begin{aligned}
T_{coat}(z=1) &= T_{sub}(z=1) \\
(1-\Re_1)\cdot I^{+}(1)\cdot e^{-r^2}-\frac{k_{coat}}{L_{coat}}\left.\frac{\partial T_{coat}}{\partial z}\right|_{z=1} &= -\frac{k_{sub}}{L_{coat}}\left.\frac{\partial T_{sub}}{\partial z}\right|_{z=1}
\end{aligned} \tag{4.6}$$

However, the subsystem model includes a thermal contact resistance R_{ss} for heat transfer from the substrate. Therefore, the interface with the subsystem is described by:

$$\begin{aligned} -R_{ss}\frac{k_{sub}}{L_{coat}}\frac{\partial T_{sub}}{\partial z}\bigg|_{z=1+Z_{sub}} &= T_{sub}\left(z=1+Z_{sub}\right)-T_{ss}\left(z=1+Z_{sub}\right) \\ -\frac{k_{sub}}{L_{coat}}\frac{\partial T_{sub}}{\partial z}\bigg|_{z=1+Z_{sub}} &= -\frac{k_{ss}}{L_{coat}}\frac{\partial T_{ss}}{\partial z}\bigg|_{z=1+Z_{sub}} \end{aligned} \tag{4.7}$$

Temporal heating can be decomposed into the form $I\left(t\right)=\overline{I}_o+re\left\{\tilde{I}_o e^{i\omega t}\right\}$, where $\overline{I}_o$ is a steady offset to the harmonic heat flux $\tilde{I}_o$ and ω is the angular frequency of heating $\left(\omega=2\pi f\right)$. The superposition of steady and transient temperature fields

$$T\left(r,z,t\right)=\overline{T}\left(r,z\right)+T^*\left(r,z,t\right) \tag{4.8}$$

can be used to express a solution to the heat equation and boundary conditions. This decomposition applied to the conduction equation and boundary conditions yields two problems similar in form to the original. However, heating for the transient T^* problem is given by $re\left\{\tilde{I}_o e^{i\omega t}\right\}$ and heating for the steady $\overline{T}$ problem is given by $\overline{I}_o$. For determining the phase of the thermal emission from the coating, only the T^* temperature field needs to be evaluated. Using the method of complex combination, the transient temperature can be expressed in terms of a complex variable $\tilde{T}\left(r,z\right)$

through the relation: $T^*(r,z,t) = re\left\{\tilde{T}(r,z)e^{i\omega t}\right\}$. With this transformation, the conduction equation (4.1) becomes:

$$\left(\frac{L_{coat}}{R_{heat}}\right)^2\left(\frac{\partial^2\tilde{T}}{\partial r^2}+\frac{1}{r}\frac{\partial\tilde{T}}{\partial r}\right)+\frac{\partial^2\tilde{T}}{\partial z^2}-\frac{i\omega L_{coat}^2}{\alpha_z}\tilde{T}+\tilde{S}(z,t)e^{-r^2}=0 \tag{4.9}$$

The definition of the axial heating function $\tilde{S}$ remains similar to that for S except that appearances of $I(t)$ are replaced with $\tilde{I}_o$. The problem for the complex temperature field is made dimensionless with the following definitions:

$$\tilde{\theta} = \frac{\tilde{T}}{L_{coat}\tilde{I}_o(1-\Re_0)/k_{sub}} \tag{4.10}$$

$$\ell = \frac{\sqrt{\alpha_{coat}/\omega}}{L_{coat}} \tag{4.11}$$

$$a = \sqrt{\frac{\alpha}{\alpha_{sub}}} \tag{4.12}$$

$$\gamma = \sqrt{\frac{k\ \rho C}{[k\ \rho C]_{sub}}} \tag{4.13}$$

$$b = \frac{R}{L_{coat}} \tag{4.14}$$

$$\Lambda = \frac{\delta_{opt}}{L_{coat}} \tag{4.15}$$

The variable "ℓ" is a thermal diffusion length scale, or thermal penetration depth, related to the coating diffusivity and made dimensionless by the coating thickness L_{coat}. The variable "a" normalizes the thermal diffusion length scale with that in the substrate, while the variable "γ" normalizes the thermal effusivity with that of the substrate. Note that a and γ have different values in the coating, substrate and subsystem materials. In the substrate $a_{sub} = \gamma_{sub} = 1$. The variable "$b$" normalizes the beam radius by the coating thickness. The variable "Λ" is the heating optical penetration depth in the coating normalized by the coating thickness. In terms of the dimensionless variables, the conduction eq. (4.9) may be expressed as:

$$\frac{1}{b^2}\left(\frac{\partial^2\tilde{\theta}}{\partial r^2} + \frac{1}{r}\frac{\partial\tilde{\theta}}{\partial r}\right) + \frac{\partial^2\tilde{\theta}}{\partial z^2} - \frac{ia_{coat}^2}{a^2\ell^2}\tilde{\theta} + \tilde{s}(z)e^{-r^2} = 0 \tag{4.16}$$

For simplicity it is assumed that $\Re_0 = 0$, such that the axial heating function in the conduction equation becomes:

$$\begin{aligned}\tilde{s} &= \frac{k_{sub}\cdot\tilde{S}}{L_{coat}\cdot\tilde{I}_o\cdot(1-\Re_0)} \\ &= \begin{cases} \dfrac{1}{a_{coat}\gamma_{coat}\Lambda}\left[e^{-\frac{z}{\Lambda}} + \Re_1\cdot e^{\frac{z-2}{\Lambda}}\right] & (z<1) \\ 0 & (z\geq 1) \end{cases}\end{aligned} \tag{4.17}$$

In terms of the dimensionless variables, the boundary conditions are:

$$\left.\frac{\partial\tilde{\theta}}{\partial r}\right|_{r=0}=0$$
$$\tilde{\theta}\left(r\to\infty\right)=0$$
$$\left.\frac{\partial\tilde{\theta}_{coat}}{\partial z}\right|_{z=0}=0 \tag{4.18}$$
$$\tilde{\theta}_{ss}\left(z\to\infty\right)=0$$

At the interface between the coating and the substrate:

$$\tilde{\theta}_{coat}\left(z=1\right)=\tilde{\theta}_{sub}\left(z=1\right)$$
$$\left(1-\Re_1\right)\cdot e^{-1/\Lambda}e^{-r^2}-a_{coat}\gamma_{coat}\left.\frac{\partial\tilde{\theta}_{coat}}{\partial z}\right|_{z=1}=-\left.\frac{\partial\tilde{\theta}_{sub}}{\partial z}\right|_{z=1} \tag{4.19}$$

and at the interface with the subsystem:

$$-R_{ss}^{*}\left.\frac{\partial\tilde{\theta}_{sub}}{\partial z}\right|_{z=1+Z_{sub}}=a_{coat}\gamma_{coat}\left[\tilde{\theta}_{sub}\left(z=1+Z_{sub}\right)-\tilde{\theta}_{ss}\left(z=1+Z_{sub}\right)\right]$$
$$\left.\frac{\partial\tilde{\theta}_{sub}}{\partial z}\right|_{z=1+Z_{sub}}=a_{ss}\gamma_{ss}\left.\frac{\partial\tilde{\theta}_{ss}}{\partial z}\right|_{z=1+Z_{sub}} \tag{4.20}$$

The contact resistance in the subsystem model has been nondimensionalized by the thermal resistance of the coating, such that:

$$R_{ss}^{*} = R_{ss}\left(\frac{k_{coat}}{L_{coat}}\right) \tag{4.21}$$

The heat diffusion equation can be solved semi-analytically through the use of the Hankel transform defined by:

$$\tilde{h}(z) = \int_0^{\infty} \tilde{\theta}(r,z)\cdot J_0(\nu r)\cdot r\cdot dr \tag{4.22}$$

Applying this transformation to the heat eq. (4.16) yields:

$$0 = \frac{d^2\tilde{h}}{dz^2} - \tilde{\nu}^2\tilde{h} + \frac{1}{2}e^{\frac{-\nu^2}{4}}\tilde{s}(z) \tag{4.23}$$

where

$$\tilde{\nu} = \sqrt{\left(\frac{c\nu}{b}\right)^2 + i\left(\frac{a_{coat}}{a\ell}\right)^2} \tag{4.24}$$

Eq. (4.23) may be integrated for the result:

$$\tilde{h} = \frac{1}{2\left(\tilde{\nu}^2 - \frac{1}{\Lambda^2}\right)}e^{-\frac{\nu^2}{4}}\tilde{s}(z) + C_A e^{\tilde{\nu}\cdot z} + C_B e^{-\tilde{\nu}\cdot z} \tag{4.25}$$

where C_A and C_B are integration constants. The transformed boundary conditions (4.18) through (4.20) become, for the surface and far-fields:

$$\left.\frac{\partial \tilde{h}}{\partial r}\right|_{r=0} = 0$$

$$\tilde{h}\left(r \to \infty\right) = 0$$

$$\left.\frac{\partial \tilde{h}_{coat}}{\partial z}\right|_{z=0} = 0 \tag{4.26}$$

$$\tilde{h}_{ss}\left(z \to \infty\right) = 0$$

for the interface between the coating and substrate:

$$\tilde{h}_{coat}\left(z=1\right) = \tilde{h}_{sub}\left(z=1\right)$$

$$\frac{\left(1-\Re_1\right)}{2} e^{-\frac{1}{\Lambda}} e^{-\frac{\nu^2}{4}} - a_{coat}\gamma_{coat}\left.\frac{\partial \tilde{h}_{coat}}{\partial z}\right|_{z=1} = -\left.\frac{\partial \tilde{h}_{sub}}{\partial z}\right|_{z=1} \tag{4.27}$$

and for the interface between the substrate and the subsystem:

$$-R_{ss}^{*}\left.\frac{\partial \tilde{h}_{sub}}{\partial z}\right|_{z=1+Z_{sub}} = a_{coat}\gamma_{coat}\left[\tilde{h}_{sub}\left(z=1+Z_{sub}\right) - \tilde{h}_{ss}\left(z=1+Z_{sub}\right)\right]$$

$$\left.\frac{\partial \tilde{h}_{sub}}{\partial z}\right|_{z=1+Z_{sub}} = a_{ss}\gamma_{ss}\left.\frac{\partial \tilde{h}_{ss}}{\partial z}\right|_{z=1+Z_{sub}} \tag{4.28}$$

The solution for $\tilde{h}$ in the coating can be expressed in the form:

$$\tilde{h}_{coat}(z) = \frac{e^{-\frac{\nu^2}{4}}}{2\left(\tilde{\nu}_{coat}^2 - \frac{1}{\Lambda^2}\right)}\left(\tilde{s}(z) - \frac{1-\Re_1 e^{-\frac{2}{\Lambda}}}{a_{coat}\gamma_{coat}\tilde{\nu}_{coat}\Lambda^2}e^{-\tilde{\nu}_{coat}z}\right) + 2C_1\cosh\left(\tilde{\nu}_{coat}z\right) \tag{4.29}$$

where the integration constants C_1 is determined as a part of satisfying the boundary conditions (4.26) through (4.28). The evaluation of C_1 is provided in Appendix A. The complex temperature solution for the coating can be found from the inverse transformation:

$$\tilde{\theta}(r,z) = H^{-1}\left[\tilde{h}(z)\right] \text{ or } \tilde{\theta} = \int_0^\infty \tilde{h}\cdot J_0(\nu\cdot r)\cdot\nu\cdot d\nu \tag{4.30}$$

Using a linear approximation for the relationship between changes in thermal emission and temperature, the thermal emission originating from the coating as a function of radiation position is given by:

$$\begin{aligned}\int_0^1 \tilde{I}_{\lambda b}(z)\,dz &\sim \int_0^1 \tilde{\theta}(z)\,dz \\ &= \int_0^1\int_0^\infty \tilde{h}(z)J_0(\nu\cdot r)\cdot\nu\cdot d\nu\,dz \\ &= \int_0^\infty\left(\int_0^1 \tilde{h}(z)\cdot dz\right)J_0(\nu\cdot r)\cdot\nu\,d\nu\end{aligned} \tag{4.31}$$

If the emission detector views an area of πr_e^2 centered on the heated area of the coating, the total emission from the coating is determined from:

$$\int_0^{r_e}\int_0^{\infty}\left(\int_0^1 \tilde{h}(\nu,z)\cdot dz\right)J_0(\nu\cdot r)\cdot\nu\cdot d\nu\cdot 2\pi r\cdot dr$$
$$= 2\pi r_e\int_0^{\infty}\left(\int_0^1 \tilde{h}(\nu,z)\cdot dz\right)J_1(\nu\cdot r_e)\,d\nu \tag{4.32}$$

Further details of the radiation model used to detect the temperature field in the coating are given by Bennett and Yu [22].

4.4 Application of subsystem model to dPopTea measurements

To investigate differential PopTea (dPopTea) measurements, the three configurations shown in Figure 4.2 were studied. The TBC/substrate/subsystem are axisymmetric with respect to the centerlines shown in the illustration. Dimensions and materials associated with these configurations are provided in Table 4.1. Configurations (i) and (ii) show measurement conditions where heat transfer beyond the length scale of the substrate L_{sub} is characterized by the "ill-defined" subsystem. The subsystem is comprised of a composite layer of finite thickness L_1 overlying a semi-infinite material (material-2). The composite layer contains a void space with surrounding material (material-1). Configuration (i) of Figure 4.2 has a 323 μm APS coating whose thermal properties are to be determined. Configuration (ii) illustrates conditions where heat transfer into the substrate/subsystem is characterized in the absence of the TBC. Finally, configuration (iii) defines the standard measurement conditions for PopTea, where heat transfer into the substrate/subsystem is "well-defined." This means that the substrate and subsystem are a continuous semi-infinite

body with negligible thermal contact resistance. In the current investigation, the thin substrate material allows thermal penetration depths into material-2. This is not ideal for standard PopTea because of the additional interface. However, in the present investigation, care is taken to provide good thermal contact (with silicon thermal paste) between the substrate and material-2, such that heat transfer into the substrate/subsystem satisfies the "well-defined" semi-infinite requirement.

In order to determine the thermal properties of the coating, dPopTea measurements are performed using configurations (i) and (ii) shown in Figure 4.3. For configuration (ii), where the topcoat is absent, an optical coating of carbon is applied to the metal surface in order to achieve satisfactory coupling of radiant energy with the surface. For validation of the differential measurements, the traditional PopTea measurement is performed for configuration (iii).

Initially the strategy was to establish the five thermal parameters: a_{coat}, γ_{coat}, a_{ss}, γ_{ss} and R_{ss}^{*} (as well as unknown optical parameters) from the measurements. However, investigations of configuration (ii) demonstrated that determining a value of an effective heating beam radius b is also necessary. Despite a priori knowledge of the true heating beam radius, an effective value is necessary because of the influence of the void region behind the substrate layer. The underlying metal sublayers predominately account for the heat spreading that occurs within the system; the presence of the void region reduces the degree of transient heat spreading on the TBC system.

Compensation for this factor can be achieved by artificially increasing the heating beam radius; thereby reducing the effects of heat spreading on the phase of thermal emission. Therefore, the parameters associated with fitting the model to experimental data of the two configurations are:

$$\begin{array}{lccccccc} config.\,(i): & \{a_{coat}\} & \{\lambda_{coat}\} & \{a_{ss}\} & \{\gamma_{ss}\} & \{R_{ss}^{*}\} & & \{\ b\ \} \\ & & & || & || & || & and & || \\ config.\,(ii): & & & \{a_{ss}\} & \{\gamma_{ss}\} & \{R_{ss}^{*}\} & & \{\ b\ \}. \end{array}$$

The thermal parameters of the subsystem (ss) and beam radius are common to both configurations. Therefore, these parameters are constrained to be identical between the two measurement conditions during fitting.

Figure 4.3 shows the dPopTea spectra obtained for a pair of differential measurements, corresponding to configurations (i) and (ii) shown in Figure 4.2. The phase of thermal emission is shown as a function of two dimensionless thermal penetration depths. For configuration (i) the dimensionless thermal penetration depth has the standard interpretation $\ell^{(i)} = \ell$, while for configuration (ii) the thermal penetration depth $\ell^{(\mathrm{ii})} = \sqrt{\alpha_{z,sub}/\omega}\,/L_{sub}$ reflects heat transfer in the substrate material. Notice that there is a one-to-one correspondence between the two measurements throughout the test frequency range, as indicated for the 2 Hz measurement in Figure 4.3. It is significant that for the current TBC system to achieve the required range of thermal penetration depths through the coating, the resulting range of dimensionless

thermal penetration depths through the substrate is nearly identical. This indicates that transient heat transfer will penetrate through the well-defined substrate material. For ordinary PopTea measurements, the dimensionless thermal penetration depth in the substrate should be significantly smaller than unity to avoid the effects of transient heat transfer into the subsystem.

Figure 4.3 shows the best fit of the heat transfer model (solid lines) to the experimental data (open symbols) for configurations (i) and (ii). The fit for configuration (i) is noticeably better than for configuration (ii), in which the importance of the subsystem model is greater. This is expected since the subsystem model is clearly an imprecise idealization of the heat transfer conditions below the substrate. It is noteworthy that the model predicts a frequency limit of $\pi/4$ for configuration (ii), corresponding to the situation where the substrate appears to be semi-infinite to the scales of heat transfer. This asymptotic behavior also requires that the optical penetration for heating and emission be vanishingly small. This limit is not fully realized experimentally because of the influence of the carbon layer used to achieve good energy coupling between the heating radiation and the surface. Nevertheless, the experimental data for configuration (ii) suggests a departure from the semi-infinite substrate behavior (approach to the $\pi/4$ limit) as the dimensionless thermal penetration depth exceeds 0.2 in the substrate. This implies that the influence of the adiabatic boundary created by the void space is felt when the penetration depth into the substrate exceeds as little as 20% of the substrate thickness. By definition, the "thermal

penetration depth" is a distance over which the amplitude of thermal transients diminishes to $1/e$ of the peak value. Therefore, it is inaccurate to interpret the penetration depth as defining a clear cutoff after which the effects of transient heat transfer are no longer influential.

As previously mentioned, a second approach to performing dPopTea measurements may be considered, where determining the variables of the subsystem is undertaken as part of the task of resolving the coating thermal properties from a single dPopTea measurement taken for configuration (i), shown in Figure 4.2. This approach alleviates the need for making a separate measurement of the uncoated substrate system. This provides a significant benefit to measurements on engine components removed from service, where the possibility of making measurements on the uncoated part is more remote.

A comparison of results between the differential measurements made on the poorly characterized subsystem and the traditional PopTea measurement are shown in Table 4.2. The differential measurements are analyzed using configuration (i) alone, and with configuration (i) and (ii) measurements coupled. The differential measurements can be contrasted with the traditional PopTea measurement corresponding to configuration (iii). Measured values of thermal diffusivity, thermal conductivity and volumetric heat capacity all fall within approximately 10% for the three measurement conditions, as shown in Table 4.2. Agreement with the traditional PopTea measurement demonstrates that dPopTea measurements can be used to successfully measure the TBC thermal

properties, even when the coating is in close thermal proximity to poorly defined heat transfer conditions.

4.5 Conclusion

In this chapter, differential phase of photothermal analysis (dPopTea) was developed with the goal of extending the utility of PopTea measurements to a wider range of engine parts. The need for the differential technique arises in coating measurements when transient heat transfer extends beyond a length scale over which the substrate material is well-defined. A subsystem model was developed to characterize heat transfer beyond the extent of a finite substrate thickness. It was demonstrated that the parameters of the subsystem model could be determined through an independent measurement of the substrate system (in the absence of the TBC) or simultaneously to a measurement of the TBC system. Comparison of both differential measurement strategies with traditional PopTea measurements of thermal properties suggest that dPopTea measurements of a coating in close proximity to ill-defined heat transfer conditions can be achieved to within 10%.

Figures and Tables

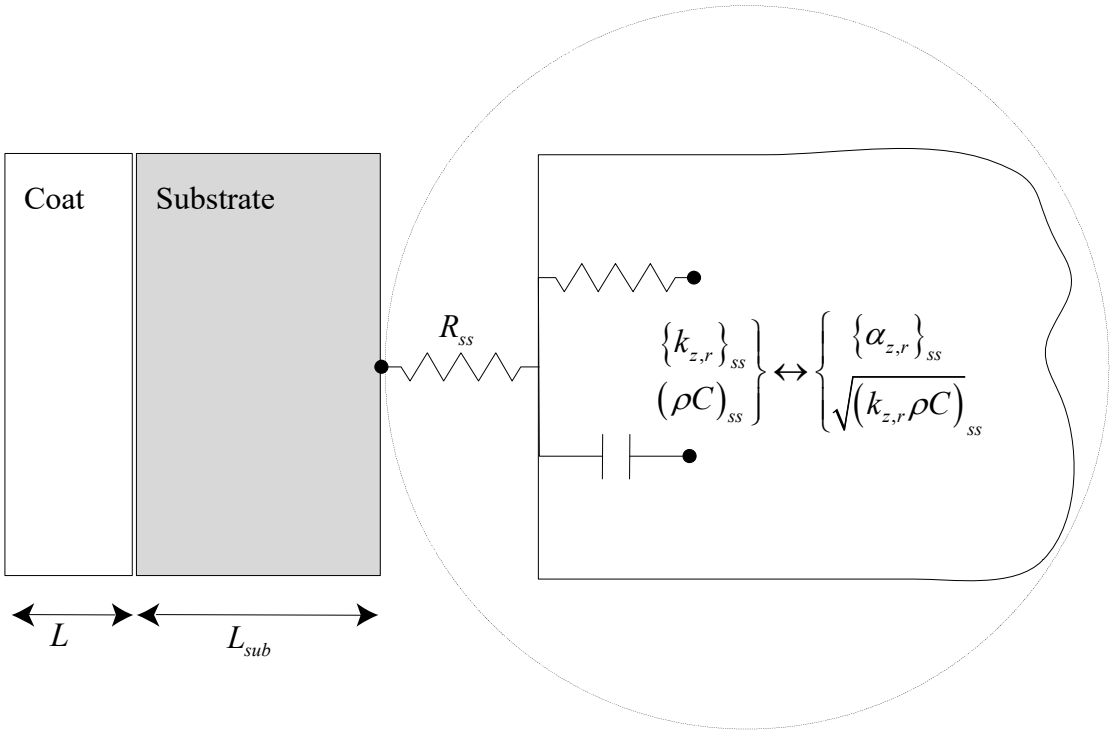

Figure 4.1: Subsystem model for the differential PopTea measurement

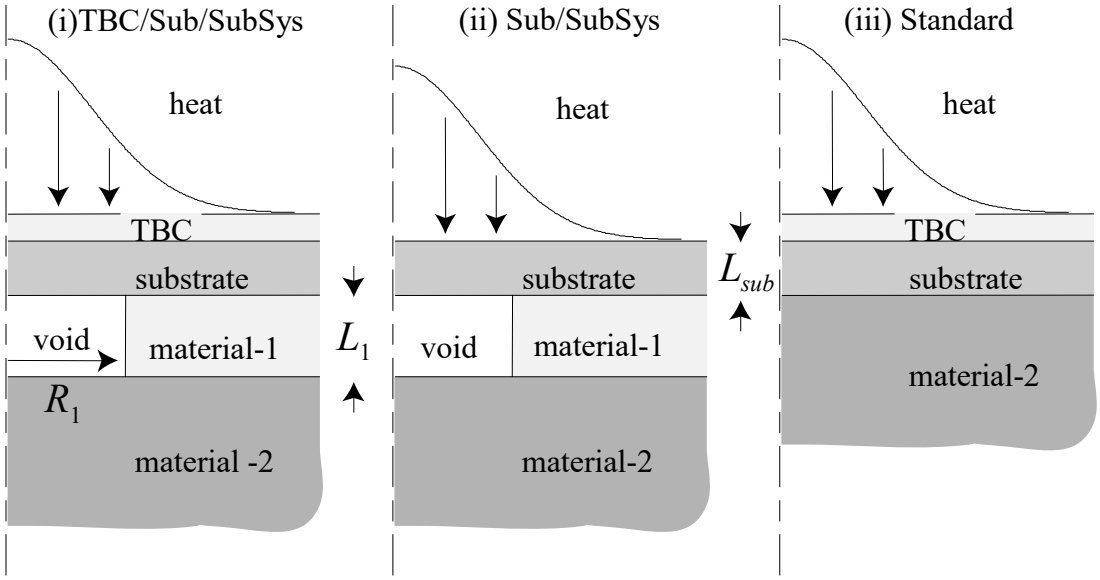

Figure 4.2: Three configurations of the PopTea measurement

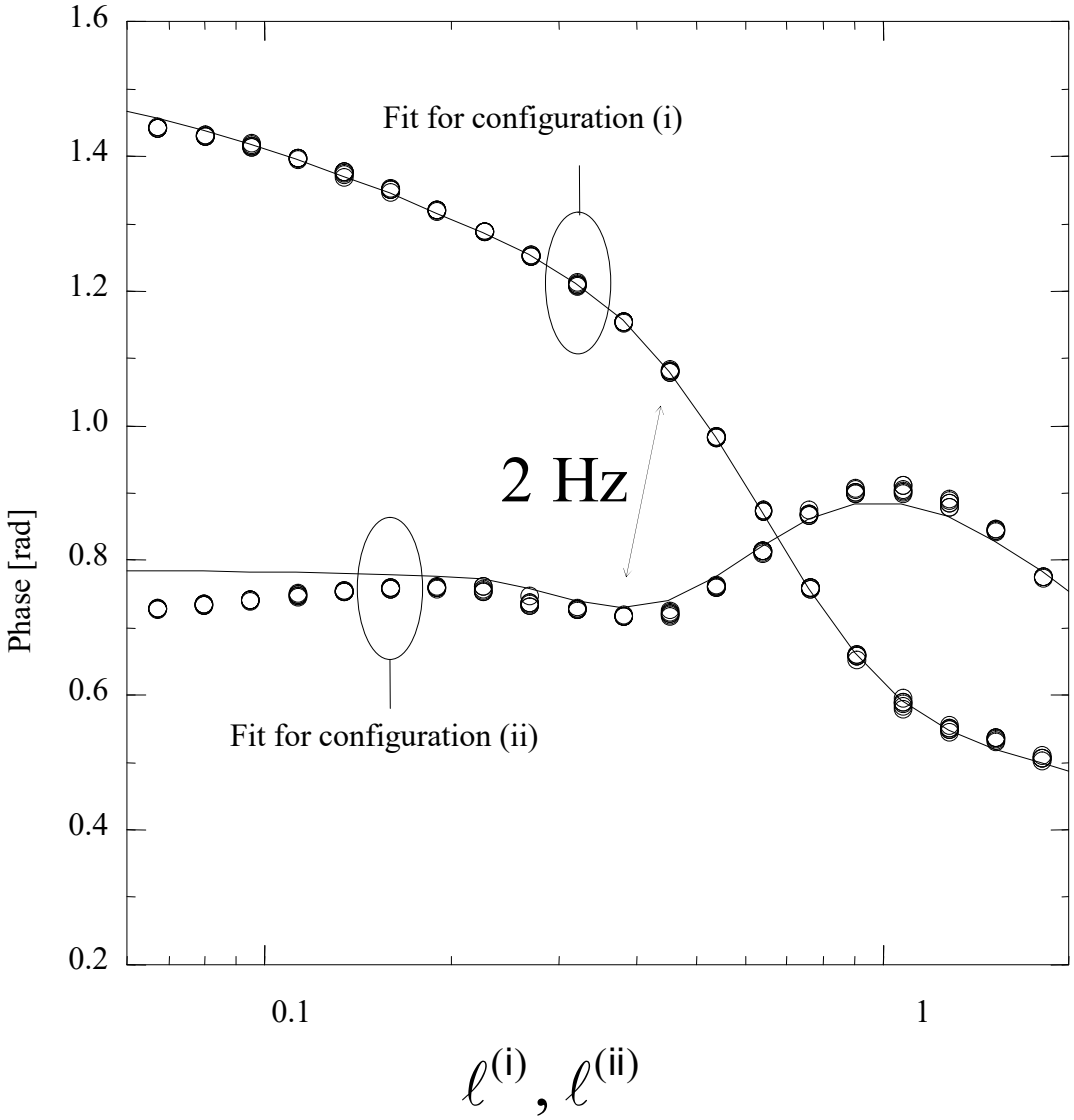

Figure 4.3: PopTea spectra for differential measurements

Table 4.1: Properties of the substrate/subsystem

		substrate	material-1	material-2
L	$[\mathrm{m}]$	0.0014	0.0030	---
k	$\left[\frac{\mathrm{W}}{\mathrm{m}^2 \cdot \mathrm{K}}\right]$	9.8	180	15
ρC	$\left[\frac{\mathrm{J}}{\mathrm{kg} \cdot \mathrm{K}}\right]$	3.6 x10^6	2.4 x10^6	3.8 x10^6
R_1	$[\mathrm{m}]$	---	0.0033	---

Table 4.2: Results of differential and standard measurements

		dPopTea (i)	dPopTea (i) & (ii)	PopTea (iii)
α	$\left[\frac{m^2}{s}\right]$	2.65 x10^{-7}	2.78 x10^{-7}	2.57 x10^{-7}
k	$\left[\frac{W}{m^2 \cdot K}\right]$	0.726	0.768	0.786
ρC	$\left[\frac{J}{kg \cdot K}\right]$	2.74 x10^{6}	2.76 x10^{6}	3.06 x10^{6}

Chapter 5 Coating Thermal Diffusivity and Effusivity Measurement Optimization using Regression-based Sensitivity

5.1 Introduction

In general, thermophysical properties are determined from the temperature response of a material to an applied heat load. A model is required to establish the mathematical relationship between material properties and this temperature response. Material properties are often determined through regression analysis [47], [132]–[139].

The sensitivity of a measurement to the properties of interest can be established with the following definition offered by Beck [139]: Suppose that a temperature measurement T_i is taken at a specific time and location in the material; the sensitivity of a material property x_j to this measurement is defined by the slope $\partial T_i / \partial x_j$. Ideally, the magnitude of this slope is large, corresponding to a high sensitivity that minimizes the uncertainty in measurement results. For example, if a single unknown property x_1 is obtained from a single measurement T_1 having uncertainty $T_{1,u}$, the uncertainty in property value is given by

$$x_{1,u} = \frac{T_{1,u}}{\dfrac{\partial T_1}{\partial x_1}} \tag{5.1}$$

When two or more material properties are determined from a set of measurements, the measurement conditions must contain sufficient information to uniquely establish these properties. In Beck's analysis of an experiment by Hsu [140], observational data from five equally spaced thermocouples embedded in a slab was used to determine the volumetric heat capacity ρC and thermal conductivity k of nickel. In Beck's study, regression analysis utilized a Gauss-Newton algorithm for minimizing the sum of squares differences between the observational data and the temperature response of the model based on candidate thermophysical properties. Although a minimum of two thermocouples is required to collect sufficient observational data for determining the

two unknowns, analysis of five widely spaced thermocouples provides better uniqueness of the temperature response and helps mitigate the influence of random errors. It is well known that the effects of random error on the uncertainty of parameter estimates can be statistically reduced by signal averaging with a redundancy of measurements [134], [141], [142].

To optimally design a measurement requires investigating what measurement set will yield the greatest sensitivity to the desired material properties. This investigation can be done with the model used for the measurement. An optimal set requires a "spread" in measurement conditions that reflects a separation of data points in either space or time. However, practical limits always curtail the extent to which measurements can be separated, which in turn affects the uncertainty of results. Additionally, and perhaps of even greater concern, these practical limits may not always be respected in the collection of data. This can lead to a situation in which measurements become biased by a discrepancy between the conditions assumed in a model and the actual physical situation arising in the experiment. Biased data can severely degrade the performance of a measurement. The erroneous interpretation of data can lead to poor accuracy of results and high uncertainty caused by the eroded quality of the fit between the model and experimental data.

In general, it is difficult to address the effects of bias-error without first identifying the nature of this error. For this reason, little guidance is found in the literature concerning disciplined approaches to reducing the effects of bias-error. This chapter

addresses an approach for contending with the presence of non-systematic bias-error in experimental data. Here, the label “non-systematic” refers to a source of bias-error that affects only a portion of a complete data set. Although Beck’s analysis did not present any form of bias-error, non-systematic bias-error is ubiquitous to experimental measurements designed around a physical model.

To illustrate non-systematic bias-error, consider a simple experiment designed to measure a constant rate of fluid discharge from a pipe. Suppose the fluid is collected using a bucket, and the height of the fluid in the bucket is measured with respect to time. Multiple measurements over the course of the discharge can be made, and the volume discharge rate can be determined from the slope of a fitted linear line through the measured fluid heights in the bucket. However, suppose some of the height measurement data was collected after the fluid began to overflow the bucket. That subset of the data would suffer from a source of bias-error not present in the preceding data, and including this erroneous data would clearly be detrimental to the results of regression analysis. This example illustrates that non-systematic bias-error can result from a failure of the model to reflect the true physical process for some, but not all, conditions of data collection.

The bucket example illustrates two competing factors in the task of minimizing uncertainty in the results of regression analysis. First, the further apart in time measurements can be made, the less uncertainty will exist in determining the slope of the height data. However, this is true only so long as the experimental data is consistent

with the model being used. At some point in time, the non-systematic bias-error of the bucket overflowing starts. Further collection of data beyond this point will degrade the ability of the model to fit the experimental data, which leads to increased uncertainty in the perceived slope as well as a loss of accuracy in the measurement. Therefore, without eyes to observe the event of the bucket overflow, the task of determining the discharge rate with the least amount of uncertainty entails using the model to help identify the occurrence of non-systematic bias-error in the data set. When done correctly, this allows reporting of the highest precision in measurement results, which hopefully is accompanied by the greatest possible accuracy of results.

A framework for assessing and minimizing uncertainty in parameter estimation using experimental data that suffers from non-systematic bias-error is developed in the context of Phase of Photothermal Emission Analysis (PopTea). PopTea was developed to nondestructively measure thermal properties of thermal barrier coatings (TBC). The measurement of TBC thermal properties is of wide interest in the scientific community involved in improving the overall performance of turbine systems used in propulsion, power generation, and diesel engines [6], [7], [24], [143]–[147].

5.2 PopTea

A detailed understanding of the PopTea method is not required for the goals of the present investigation. It is sufficient to understand that the measurement is based on a heat transfer model of a coating and substrate system undergoing periodic heating from

a laser. A radiative model is required to describe thermal emission from the TBC as viewed by a photodetector directed at the surface of the coating. The PopTea experimental setup is shown in Figure 5.1. The observational data consists of phase measurements that represent the peak-to-peak phase difference between the heating laser modulation and the volumetric thermal emission. The phase lag in emission is a consequence of the physical principles of heat transfer, in which the thermal diffusivity of the coating and thermal effusivity contrast between the coating and the substrate are in play. These parameters are introduced as dimensionless variables in the thermal model with the definitions:

$$\gamma = \frac{[e]_{substrate}}{[e]_{coating}} \tag{5.2}$$

where,

$$e = \sqrt{k\rho C} \tag{5.3}$$

and

$$a = \frac{[\alpha]_{substrate}}{[\alpha]_{coating}} \tag{5.4}$$

Notice, that from the thermal diffusivity and effusivity values, it is possible to independently evaluate the thermal conductivity, $k = e\sqrt{a}$, and volumetric heat capacity, $\rho C = e/\sqrt{a}$, of the coating.

Interpretation of PopTea measurements is complicated by the role that optical properties contribute to the heat transfer and emission models. In terms of the dimensionless variables of the model, the unknown optical properties determined as part of the regression analysis are:

$$\Lambda = \frac{\delta_{optical}}{L} \tag{5.5}$$

$$E_1 = \frac{\varepsilon_\lambda}{a_\lambda L} \tag{5.6}$$

The optical penetration of the laser into the coating is $\delta_{optical}$, and has been cast in nondimensional form by scaling with the coating thickness, L. The thermal emission fraction, E_1, is proportional to the substrate emissivity, ε_λ, and inversely proportional to the optical thickness of the coating, $a_\lambda L$; both are dependent on the detector wavelength λ. The final optical property relevant to the model is the fraction of laser energy reflected from the interface back into the coating, R_1. If the laser penetration into the coating is small $(\Lambda < 1)$ the value of R_1 is unimportant to model predictions [97] (and is assigned the value of 0.8 in the current analysis).

More than one PopTea model has been developed to address some of the specific measurement conditions that have been investigated [21], [97], [99]. For relatively thin coatings, the one-dimensional thermal model and emission model are discussed in references [21], [99]. The four unknown parameters for this model include the two thermal parameters (γ, a), and two optical parameters (Λ, E_1) as described above. With the one-dimensional thermal model (model C of reference [99]) the measured phase lag of thermal emission, ϕ, is related to the optical and thermal properties of the coating by the analytic solution:

$$\phi = \arg\left[\left(\frac{E_1 \cdot \left(\frac{\sqrt{i}}{\ell}\right) - 4\gamma}{2\left(1-\hat{\Lambda}^2 i\right)}\right)\left(\begin{array}{l}\left(1+R_1\right)\left(1-e^{-\frac{2}{\Lambda}}\right)\tilde{M}\left(\sqrt{i}\hat{\Lambda}\right) \\ +\left(1-R_1\right)\left(1+e^{-\frac{2}{\Lambda}}\right)\tilde{N}\left(i\hat{\Lambda}^2\right)\end{array}\right)\right. \\ \left. +4\left(1-R_1 e^{-\frac{2}{\Lambda}}\right)\right] - \frac{\pi}{2} \tag{5.7}$$

where,

$$\tilde{M}\left(x\right) = \left(1 - \frac{x\sinh\left(\frac{\sqrt{i}}{\ell}\right)}{\sinh\left(\frac{1}{\Lambda}\right)}\right)\left(\gamma\cosh\left(\frac{\sqrt{i}}{\ell}\right) + \sinh\left(\frac{\sqrt{i}}{\ell}\right)\right)^{-1} \tag{5.8}$$

$$\tilde{N}(x) = \frac{1 - x\cosh\left(\frac{\sqrt{i}}{\ell}\right) \Big/ \cosh\left(\frac{1}{\Lambda}\right)}{\gamma\cosh\left(\frac{\sqrt{i}}{\ell}\right) + \sinh\left(\frac{\sqrt{i}}{\ell}\right)} \tag{5.9}$$

and $\hat{\Lambda} = \Lambda/\ell$. The thermal penetration is a function of the modulation frequency of the laser coating f and the thermal diffusivity, and can be nondimensionalized by the coating thickness:

$$\ell = \frac{1}{L}\sqrt{\frac{[\alpha]_{coating}}{2\pi f}} = \frac{1}{L}\sqrt{\frac{[\alpha]_{substrate}}{2\pi a\, f}} \tag{5.10}$$

Thermal penetration describes the depth of transient thermal probing of heat into the coating. Eq. (5.2) through eq. (5.10) reflect the model that has been used for the analysis in this investigation. However, the methodology developed in this chapter can be used with any model to establish the minimal uncertainty in property measurements from regression analysis.

5.3 Regression Analysis and Parameter Interval Estimates

This section describes a method to determine the uncertainty of best-fit parameter estimates established with regression analysis using a model and a set of experimental observations. The methodology is extended to minimizing the uncertainty in parameter estimates by identifying and removing non-systematic bias-error in the observational

data. This leads to a procedure by which the parameter estimation analysis can be optimized to report the lowest possible uncertainty in the best-fit estimates.

A metric for the conformity between model predictions and observational data is used to quantify how well the model is fitted to the system. In the present analysis, this conformity is defined to be the biased sample variance. Let $\hat{\boldsymbol{\phi}}$ be a set of observational experimental measurements and $\boldsymbol{\phi}(\boldsymbol{x})$ be the corresponding model predictions that are based on the set of parameter estimates, $\boldsymbol{x}$. Then the sample variance, S, is defined by:

$$S(\boldsymbol{x}) = \frac{1}{N}\sum_{i=1}^{N}\left(\hat{\phi}_i - \phi_i(\boldsymbol{x})\right)^2 , \tag{5.11}$$

where the i-index reflects the individual data points that comprise a set of measurements. Regression analysis using the model and observational values will find the best-fit parameter estimates, $\boldsymbol{x}_{\mathbf{bf}}$, where the minimum of eq. (5.11) exists.

If an alternate set of parameter estimates, $\boldsymbol{x}'$, can be found that produces essentially the same model results as $\boldsymbol{x}_{\mathbf{bf}}$, then the fit is not unique. Uncertainty bounds on $\boldsymbol{x}_{\mathbf{bf}}$ can be developed based on identifying the parameter intervals over which the model results corresponding to $\boldsymbol{x}'$ cannot be confidently distinguished from the results of $\boldsymbol{x}_{\mathbf{bf}}$. By individually perturbing each of the k parameters away from its best-fit-value, and then performing regression analysis on the remaining $k-1$ parameters, alternate sets

$\boldsymbol{x}'$ that exhibit a minimal change from the model results based on $\boldsymbol{x}_{\mathbf{bf}}$ can be found. The regression analysis performed during the perturbation allows the other estimated parameters of $\boldsymbol{x}'$ to compensate for the forced perturbation of an individual parameter estimate (to the extent allowed by the model). The sample variance between the model results for $\boldsymbol{x}_{\mathbf{bf}}$ and $\boldsymbol{x}'$ is used as the metric for quantifying this change:

$$S(\boldsymbol{x}) = \frac{1}{N}\sum_{i=1}^{N}\left(\phi_i(\boldsymbol{x}') - \phi_i(\boldsymbol{x}_{\mathbf{bf}})\right)^2 \tag{5.12}$$

The extent to which individual parameter estimates can be perturbed (upward and downward) before the sample variance defined by eq. (5.12) exceeds the original sample variance between the observational data and the best-fit model results defined by eq. (5.11) defines the parameter interval estimates (PIE). This range establishes the uncertainty associated with the best-fit values. The percent uncertainty in each parameter can be defined as:

$$x_u = \frac{x'_{\text{upper bound}} - x'_{\text{lower bound}}}{x_{\text{bf}}} \times 100 \tag{5.13}$$

The magnitude in uncertainty associated with each variable is influenced by two factors. The first is the uniqueness with which a variable is constrained by the comparison between the model and experimental data. If the value of a variable can be changed without significantly changing this comparison, then the uniqueness of the

best-fit value is not good. The second factor influencing the assignment of uncertainties is the quality of the original best-fit results defined by eq. (5.11). If the model results using best-fit estimates $\boldsymbol{x}_{\mathbf{bf}}$ exhibits a large variance from the experimental data, it becomes possible to perturb the parameter estimates further before the sample variance given by eq. (5.12) becomes comparable. However, if a large sample variance given by eq. (5.11) is due to non-systematic bias-error, then it may be possible to find best-fit estimates with smaller uncertainty by a reduction of the experimental data. However, care must be taken not to excessively reduce the observational dataset because the parameters will increasingly lose sensitivity to the model response and begin to lose uniqueness due to insufficient information in the dataset. Balancing these two needs is its own optimization problem, where the objective function for this minimization task is based on eq. (5.13). The observational dataset can now be reduced in a way that minimizes the uncertainty in parameter estimates. Using these ideas, a search for the optimal subset from the original observational dataset can be sought using a minimization algorithm.

5.4 Application to thermal diffusivity measurements

The thermal modeling and analysis of the PopTea method were all carried out using the authors' custom written C++ code. To illustrate the analysis, observational data sets were generated using the thermal model. Generation of data is preferred in the present study to eliminate any uncertainty about the "true" thermal properties of the TBC. Each

dataset was created by sampling from a wide range of laser modulation frequencies. This creates a range of independent observational values that vary with respect to the thermal penetration depth, as given by eq. (5.10). Sources of error were added to the data in the form of random Gaussian noise and non-systematic bias-error. In PopTea, non-systematic bias-error typically occurs at the high and the low limits of thermal penetration depths. Such sources of bias-error are associated with heat transfer interacting with scales of the coating system that are not accurately reflected in the model. For example, at shallow thermal penetration depths, heat diffusion begins to interact with near surface scales of the coating. This can reflect physical characteristics such as surface roughness and contamination that are not accounted for in the thermal model. At long thermal penetration depths, heat transfer can interact with scales that are larger than the well-defined substrate thickness. Since the model assumes a semi-infinite substrate this would also lead to bias-error.

Figure 5.2 illustrates a dataset with random noise and bias-error at both high and low thermal penetration depths. The true thermal properties of the coating system are given in Table 5.1. Notice that the dataset shown in Figure 5.2 spans a range of thermal penetration depths from $0.01 \leq \ell \leq 10$. To explore the effect of bias-error and noise on the regression analysis, four observational data sets were constructed using different combinations of error. Each dataset has random Gaussian error; the first dataset (random) has no bias-error. There are two more data

sets for which bias-error is added to either the short (bias-L) or long (bias-R) thermal penetration depths. Finally, the fourth dataset exhibits bias-error on both short and long (bias-LR) thermal penetration depths. The model was fitted to the four observational data sets using the Levenberg-Marquardt Algorithm (LMA), which was adopted from the MINPACK implementation. The minimization or objective function for the LMA was eq. (5.11) using the observational data and the model predictions. Since the true coating properties are known, it is possible to contrast the best-fit results with the true values for the different cases of data error. Note that in these baseline fittings, the unknown parameters were estimated using the full-range of observational data, $0.01 \le \ell \le 10$. In addition to the best-fit values, x_{bf}, the parameter uncertainty, x_u, was also reported as calculated using the PIE analysis and eq. (5.13). The results from the best-fit and PIE analysis are shown in Table 5.2.

Inspecting the results in Table 5.2 for the best-fit and PIE analysis shows several clear trends. In general, addition of bias-error broadens the uncertainty associated with the measurements. With the exception of the thermal effusivity, γ, the increase in uncertainty is associated with a decrease in precision but not accuracy in the nominal best-fit. The values for the thermal diffusivity and optical properties did not stray significantly from their true values with the addition of bias-error. However, thermal effusivity exhibited a significant increase in uncertainty and drift from the true value. The ability to measure the thermal effusivity is dependent on the observational data that probes the interface between the coating and the substrate. Therefore, it is then not

surprising to see large increases in uncertainty of thermal effusivity for the Bias-R and Bias-LR scenarios since both cases degrade the quality of measurements having thermal penetration depths sufficient to probe the interface condition $\ell \geq 1$.

The only way to improve the results of regression analysis is to reduce the effects of bias-error in the observational data. To this end, the use of subsets of the observational data is explored as a means of reducing fitting uncertainties. To emphasize the importance of thermal parameter estimates, an average uncertainty of the thermal diffusivity, thermal effusivity, and optical penetration is defined by:

$$S_{\text{PopTea}} = \frac{1}{3}\left(x_{u,a} + x_{u,\gamma} + x_{u,\Lambda} \right) \tag{5.14}$$

Subsets of the observational data can be defined by a range of thermal penetration depths $\ell_{\min}$ to $\ell_{\max}$, where $0.01 < \ell_{\min} < \ell_{\max} < 10.0$. For each subset of observational data, regression analysis is performed to determine the best fit and PIE analysis is performed to determine the average uncertainty defined by eq. (5.14). The average uncertainty may be contoured as a function of the subset range, with the goal of identifying an optimal subset that minimizes the uncertainty in parameter estimates.

Figure 5.3 shows the results in subset analysis when only random noise is applied to the observational data. The minimum in average uncertainty can be achieved so long as the subset of data is roughly bounded by a thermal penetration minimum of $\ell_{\min} \leq 0.157$ and thermal penetration maximum of $\ell_{\max} \geq 1.5$. This means that taking

any data subset that meet these constraints will yield a similar level of uncertainty in the PopTea measurement. This region is indicated with hatch marks in the contour plot. When values of $\ell_{\min}$ exceed 0.157 the dataset begins to lack sufficient information to correctly resolve all of the fitted variables. In particular, it is difficult to determine the correct optical penetration depth without sufficiently short thermal penetration depth data. Likewise, when $\ell_{\max}$ falls below 1.5, the amount of information in the data set that resolves the thermal properties concerning the interface begins to suffer. Since the full dataset shown in Figure 5.4 does not have bias noise, the model is able to fit perfectly through the random noise. Trimming the outer bounds of this dataset will not reduce the effect of random noise.

The Bias-L observational data case has short thermal penetration bias-error added to the random noise. The S_{PopTea} mapping to the data subsets is shown in Figure 5.5 and best-fit model predictions after dataset optimization is shown in Figure 5.6. Notice that there is a range of observational data subsets that have a similarly low level of mean uncertainty given by S_{PopTea}. The results show that any dataset with a minimum thermal penetration in the range of $0.018 \leq \ell_{\min} \leq 0.16$ and a maximum thermal penetration $\ell_{\max} \geq 1.42$ will yield comparably low values of S_{PopTea}. $\ell_{\min}$ now exhibits a finite range of acceptable values because for values less than 0.018 the dataset is afflicted by the presence of bias-error, and for values greater than 0.16 the dataset begins to lack sufficient information to correctly resolve the fitted variables.

Notice that the fitted range demarcated by cross-hatch in Figure 5.6 effectively rejects the biased data.

The Bias-R dataset has bias-error added to the random noise at long thermal penetration depths. The S_{PopTea} mapping to the data subsets is shown in Figure 5.7 and best-fit model predictions after dataset optimization is shown in Figure 5.8. Since the bias-error only affects the right hand side of the observational data, there is no penalty for using all of the observational data at shorter thermal penetration depths. The minimum thermal penetration is bounded by $\ell_{\min} \leq 0.16$, as required for acquiring sufficient short thermal penetration depth data to resolve the fitted parameters. However, now the maximum thermal penetration for the optimized dataset is bounded by $1.3 \leq \ell_{\max} \leq 3.4$. $\ell_{\max}$ now exhibits a finite range of acceptable values because for values less than 1.3 the dataset begins to lack sufficient information to correctly resolve the interface condition, and for values greater than 3.4 the dataset is afflicted by the presence of bias-error.

The final biased observational data set, Bias-LR, has bias-error for both short and long thermal penetration depths, in addition to random noise. The S_{PopTea} mapping to the data subsets is shown in Figure 5.9 and a model predictions corresponding to best-fit results for the optimized data subset is shown in Figure 5.10. Now the optimized data subset is required to have a minimum thermal penetration that is roughly bounded by $0.024 \leq \ell_{\min} \leq 0.15$ and the

maximum thermal penetration that is bounded by $1.6 \le \ell_{max} \le 3.8$. Both short and long thermal penetration depths of the optimized dataset are bounded by the competing requirements of having sufficient information in the data set to resolve the fitted parameters, and having minimal bias-error.

In general, an optimization algorithm that minimizes S_{PopTea} given by eq. (5.14) can be implemented as part of regression analysis without investigating the complete mapping of S_{PopTea}. This dataset optimization procedure can be implemented with the Levenberg-Marquardt Algorithm using ℓ_{min} and ℓ_{max} as the unknown parameters. In Figure 5.3 through Figure 5.10 the marker $\otimes$ shows optimal values of ℓ_{min} and ℓ_{max} as determined from the S_{PopTea} minimization procedure. The best-fits and PIE uncertainties from using these data subsets are shown in Table 5.3. Notice that for the three datasets with bias-error, the optimized data subsets coincide with a range of thermal penetration depths that are minimally affected by bias-error.

The results of the PIE uncertainty analysis of the optimal data subsets in Table 5.3 can be compared with the benchmark PIE analysis results from the full data sets in Table 5.2. The results from the optimal data subsets showed remarkable improvement in reducing the uncertainty of the parameter estimates for the three data sets exhibiting non-systematic bias-error. Although, it is not possible to ensure that the accuracy of the parameter estimates will improve without knowing the exact values a priori. The premise of the current uncertainty minimization method is that the bias-error is non-

systematic that affects a small but non-negligible portion of the observational data. The systematic biases are typically resolved by experimental calibration or by adding an error contribution to the model. Reducing this non-systematic bias-error results in data and parameter estimates that best describe the physical system. Therefore, it is not surprising that not only did the uncertainty in the parameter estimates decrease, but also the accuracy of the estimates for the thermal effusivity were now much closer to their true values. After dataset optimization, the parameter uncertainties corresponding to the datasets with bias-error were comparable to parameter uncertainties determined from the data set with only random noise. This is possible because the dataset optimization procedure reduced the dataset in a way that increases conformity of the model to the data without sacrificing too much information needed to make parameter estimates. Most importantly, the optimization procedure resulted in the exclusion of most of the bias-error in the observational data subsets that can reduce the accuracy of the measurement.

As a final note, the parameter uncertainties corresponding to the dataset with only random Gaussian noise are simply dependent on the model sensitivity to the thermal penetration range and not errors in the observational data. As long as the observations include sufficient data for both shallow and deep thermal penetration measurements, there cannot be a significant improvement in the results of regression analysis by using a subset of the observational data. Nevertheless, the dataset optimization procedure may reject some of the non-bias random-noise data at both limits of the range. This is

a consequence of the diminishing sensitivity of the estimated parameters to the observational data associated with the limiting cases of $\ell \ll 1$ and $\ell \gg 1$.

5.5 Summary and Conclusion

An approach has been presented to determine the uncertainty of a parameter estimation method. The approach was expanded to determine the minimal uncertainty in fitted parameters by searching for an optimal subset in the observational data that reduces the effect of non-systematic bias-error at the limits of the observational data. The expanded approach searched for the optimal data subset by treating the data measurement span as two independent variables to manipulate, $\ell_{\min}$ and $\ell_{\max}$. This uncertainty minimization approach effectively uses the model for the experimental data to help identify and eliminate non-systematic bias-error in the observational data. The uncertainty minimization was designed for the a priori known characteristics of the bias-error, endemic to the ends of the observational data; however, the procedure should be adapted to the types of error expected in their specific applications. An example of an alternative approach would be for a system that has random outliers or errors throughout the observational data. This type of system may benefit from an uncertainty minimization algorithm that is based on cycling through the observational data and eliminating those data values that lead to reduced uncertainty in the parameter estimates.

An illustrative example was carried out on the PopTea method for simultaneous measurements of thermal diffusivity and thermal effusivity of a thermal barrier coating. It was found that the effects of bias-error in the data can be greatly reduced by the appropriate selection of a subset of the observational data. Mapping parameter uncertainties showed that a wide-range of data subsets may exist having a similar level of minimal parameter uncertainty. By eliminating bias-error with the use of a data subset, the uncertainty in parameter estimates can be made comparable to the results of a dataset having only random Gaussian noise. However, if there is only random Gaussian noise in the full dataset, then no significant benefit results from trying to find an optimal subset of the observational data.

Figures and Tables

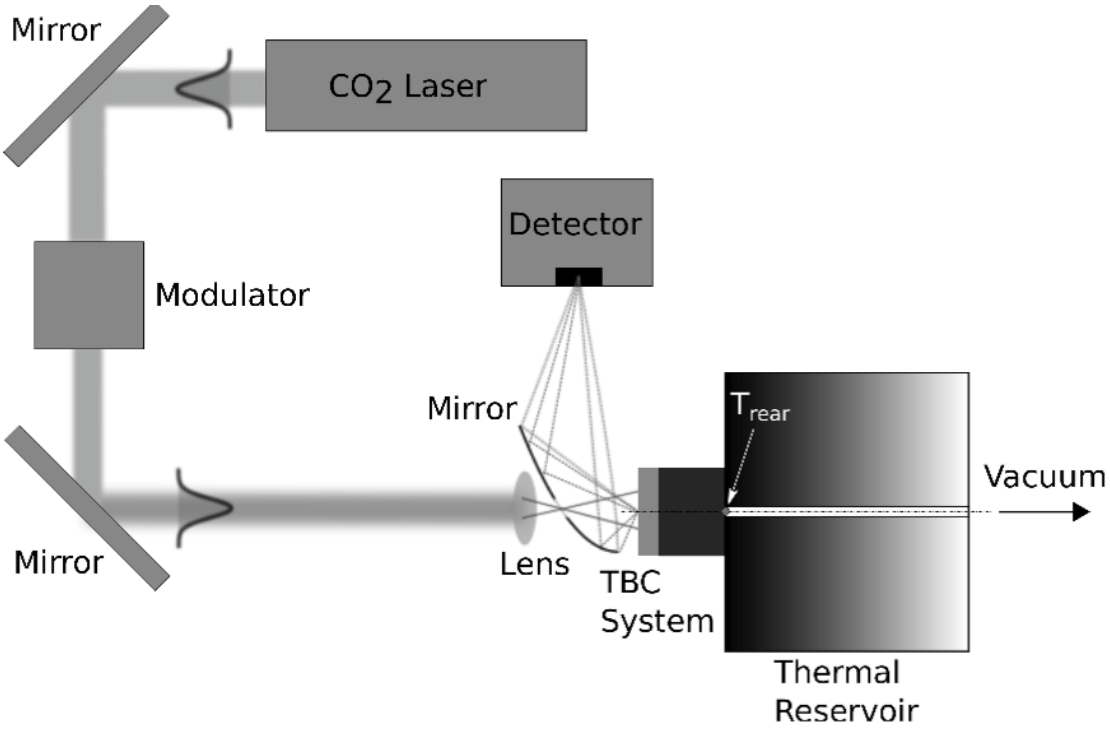

Figure 5.1: Experimental design of the non-destructive thermal diffusivity and thermal effusivity measurement technique, PopTea. The laser heating is modulated using an opto-acoustic modulator and the thermal response is measured using an In-Sb detector. The thermal reservoir maintains the coating and substrate at a constant temperature.

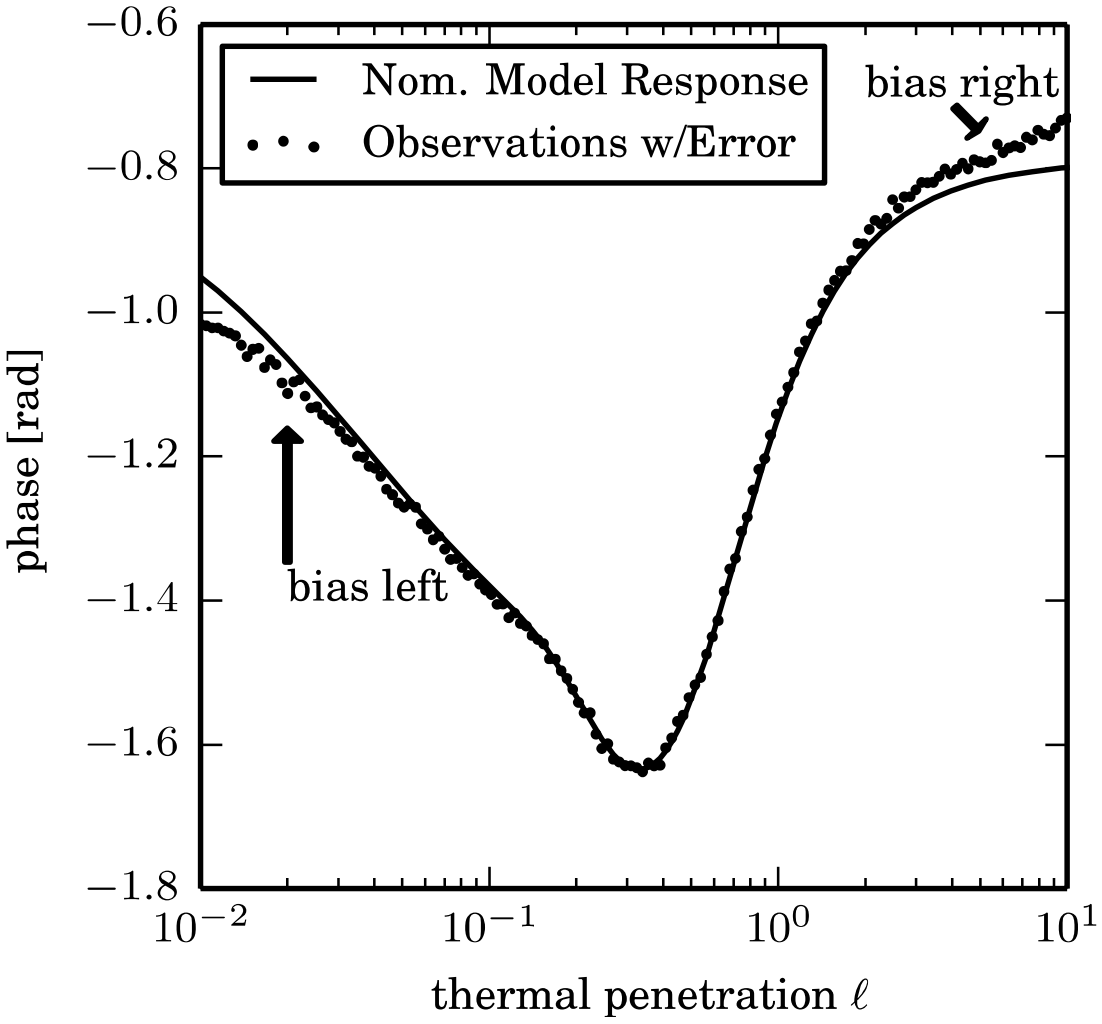

Figure 5.2: The bias-error (left and right ends) and random noise was added to a nominal model response to create the observational data

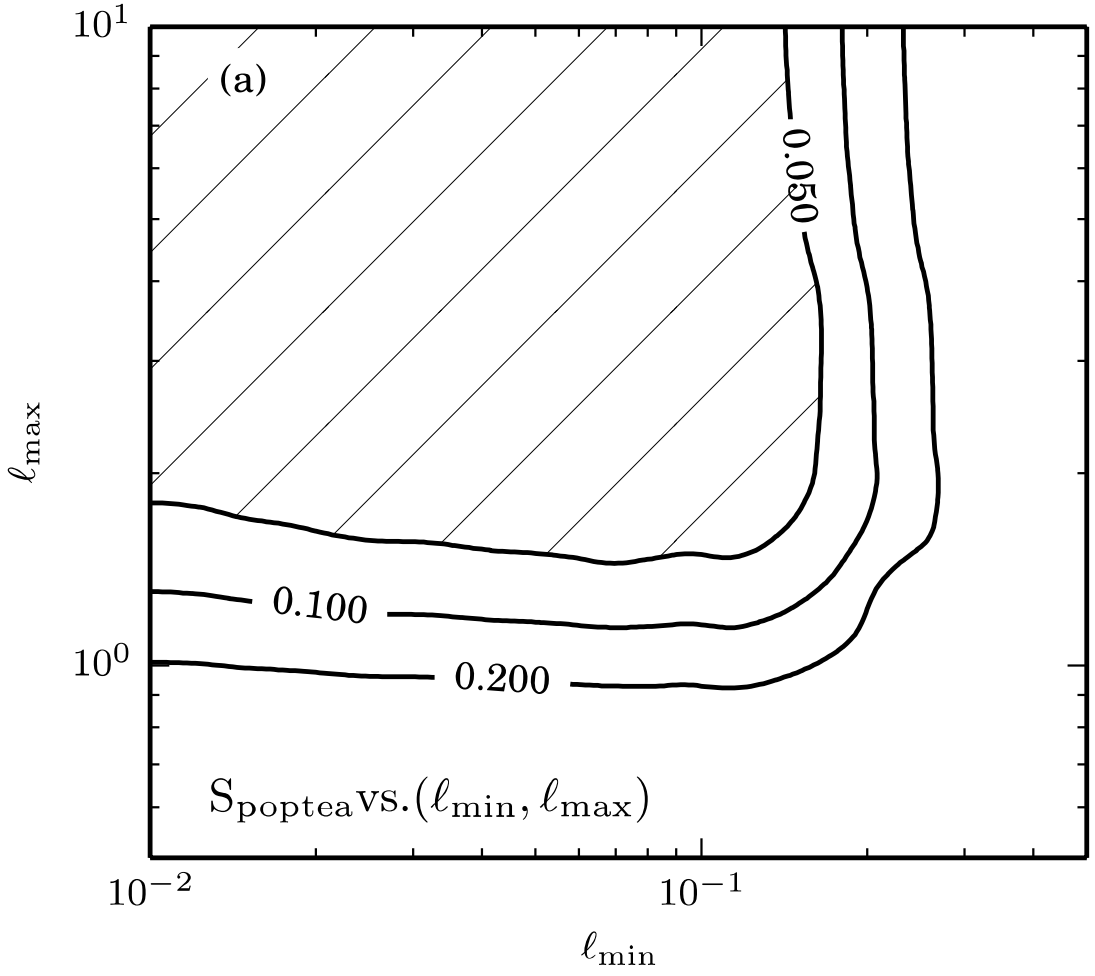

Figure 5.3: The contour plot shows the overall fitting uncertainty as a function of the Bias-R observational data subsets. The hatched area illustrates the spread of data subsets that have a similar low level of uncertainty in the fitted parameters.

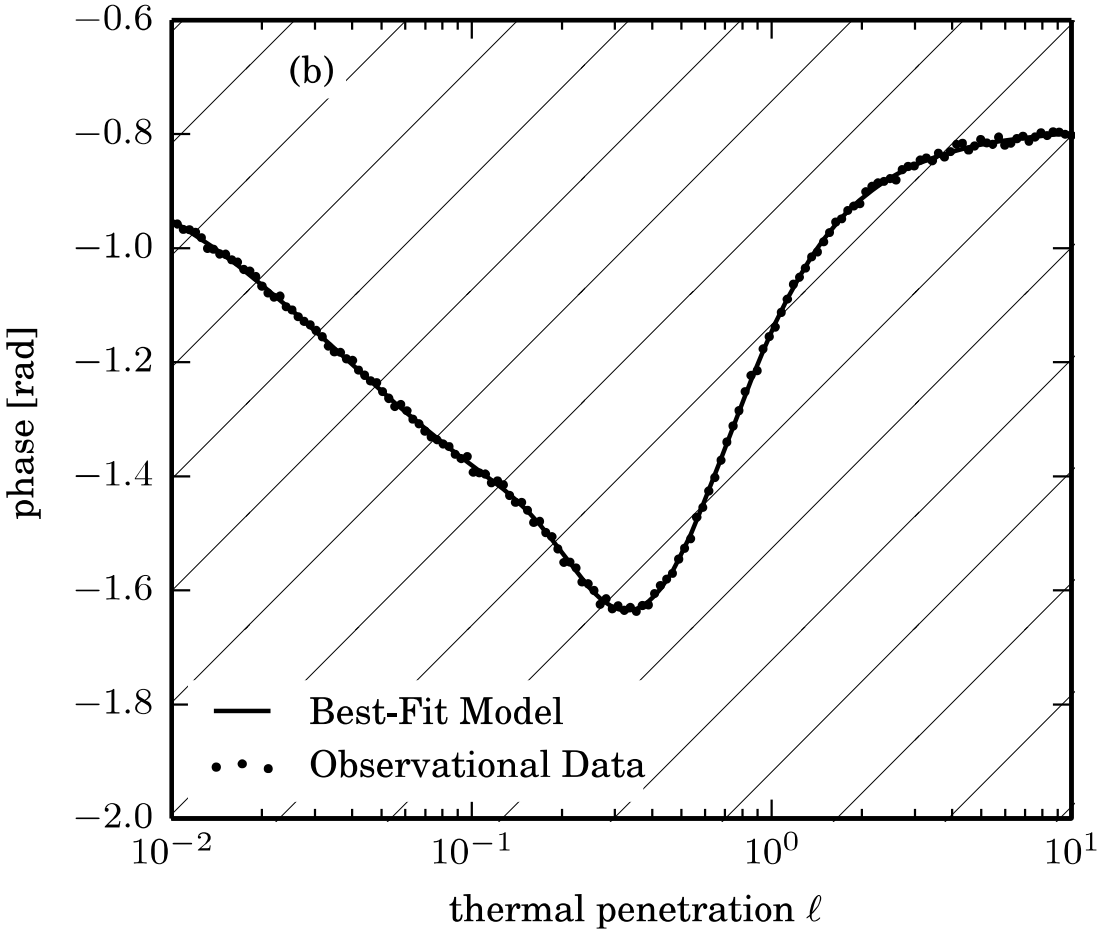

Figure 5.4: The Bias-R observational data is shown with an optimal best-fit result from the full data set. The single hatch represents the maximum extents of the data with the same level of low uncertainty.

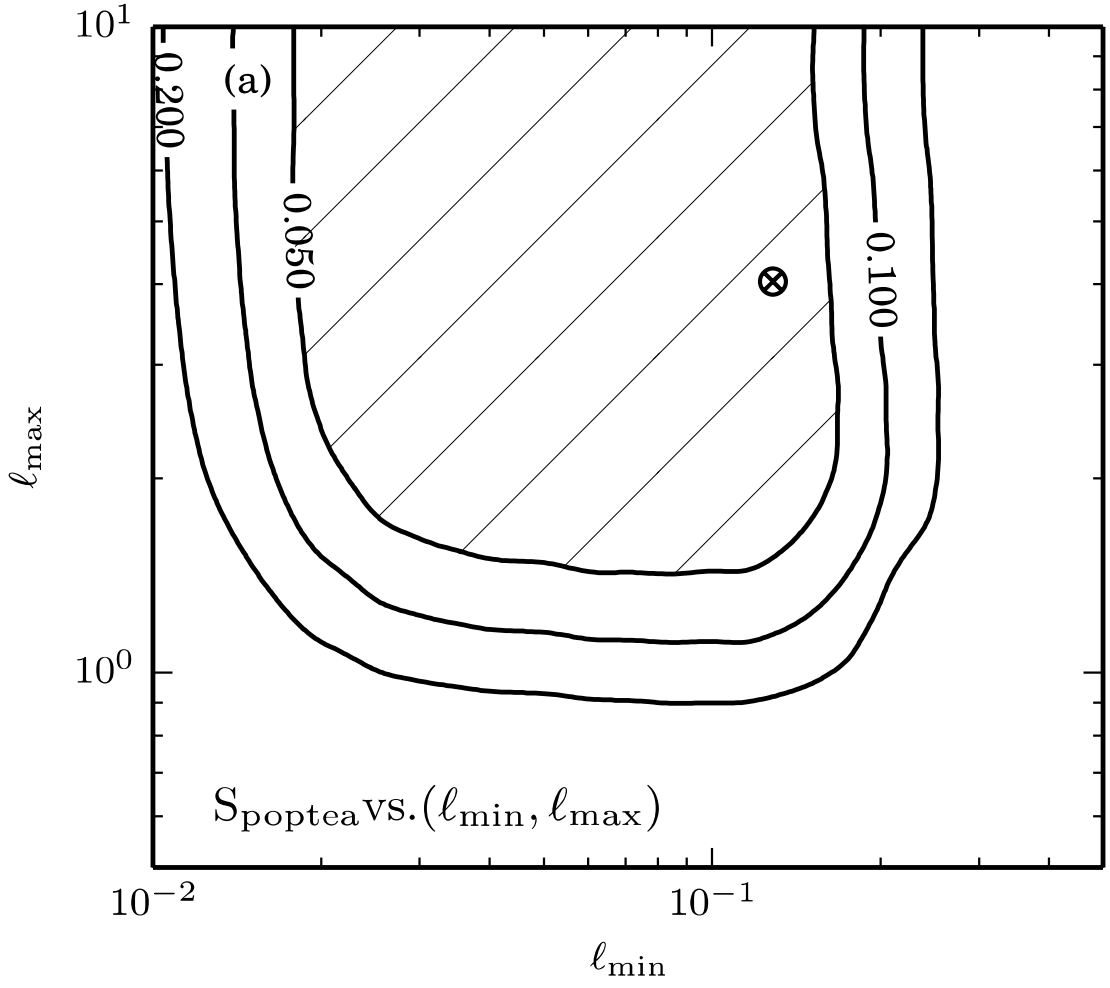

Figure 5.5: The contour plot shows the overall fitting uncertainty as a function of the Bias-L observational data subsets. The hatched area illustrates the spread of data subsets that have a similar low level of uncertainty. The optimal data subset ⊗ was found by minimizing S_{PopTea}.

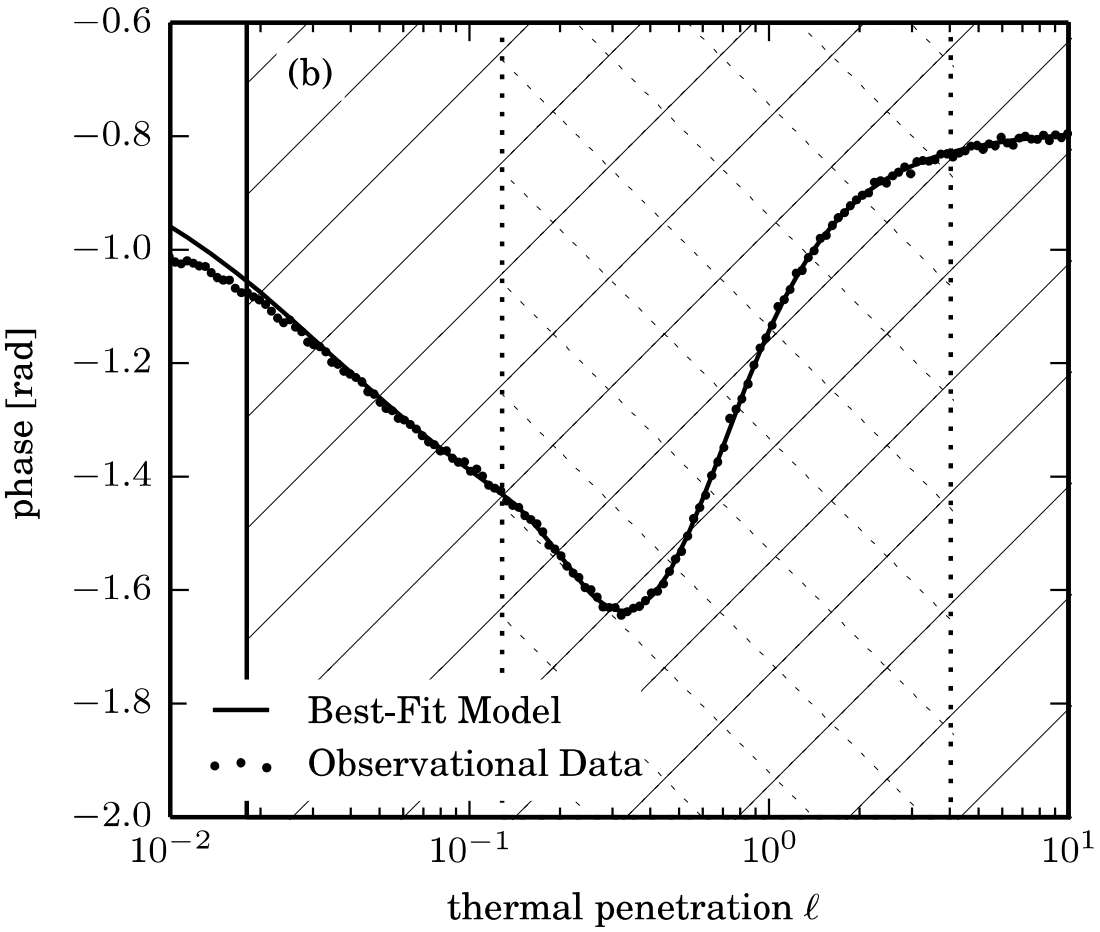

Figure 5.6: Bias-L observational data shown with the model results for best-fit parameters estimates obtained from the optimized ⊗ data subset (as demarcated by cross-hatch). The single hatch represents the maximum extents of the data with the same level of low uncertainty.

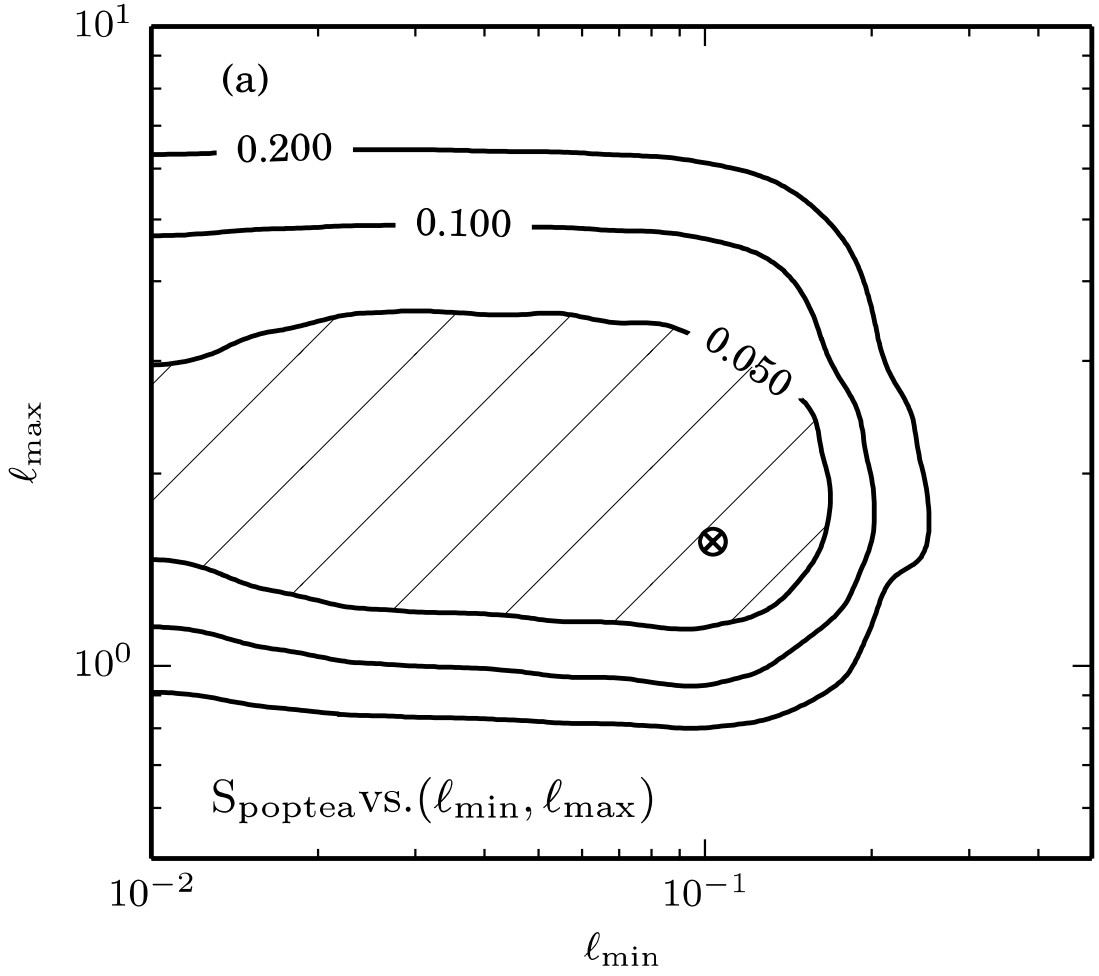

Figure 5.7: The contour plot shows the overall fitting uncertainty as a function of the Bias-R observational data subsets. The hatched area illustrates the spread of data subsets that have a similar level of uncertainty. The optimal data subset ⊗ was found by minimizing S_{PopTea}.

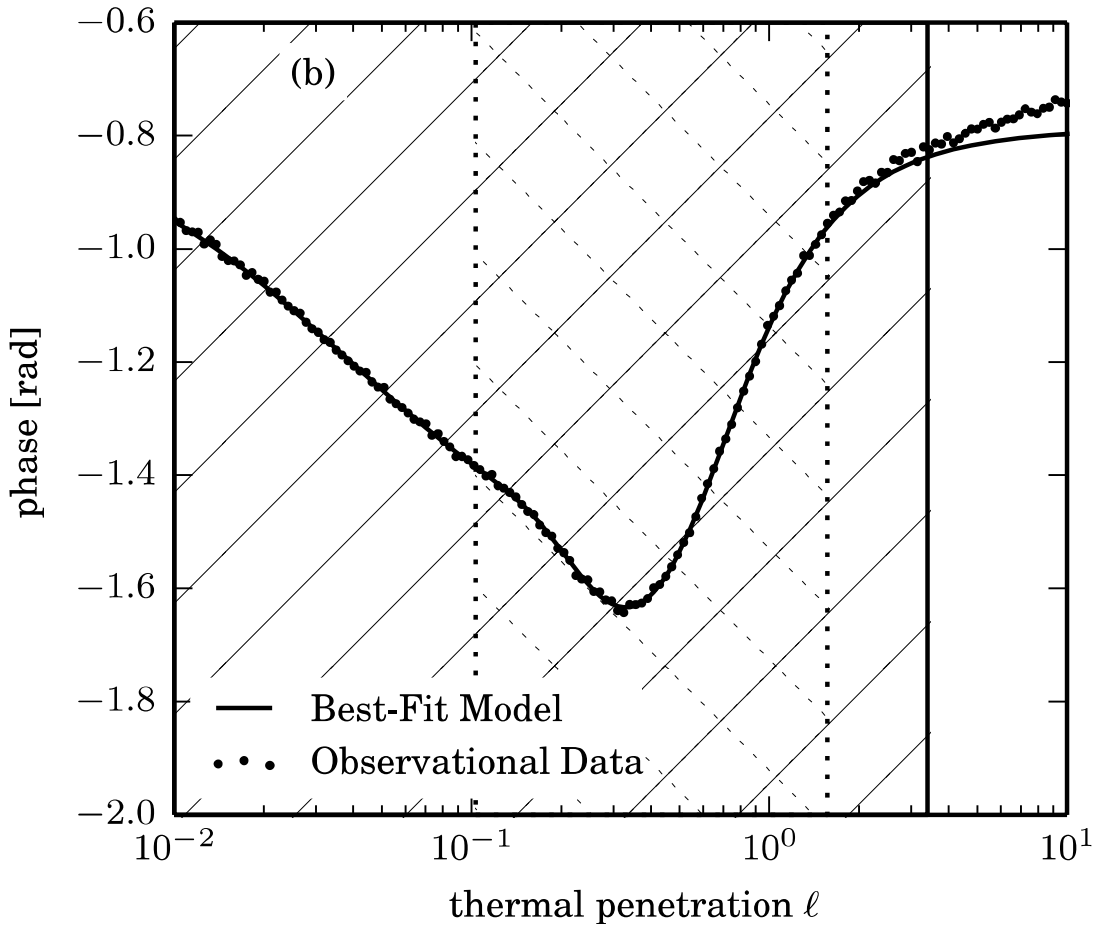

Figure 5.8: Bias-R observational data shown with the model results for best-fit parameters estimates obtained from the optimized ⊗ data subset (as demarcated by cross-hatch). The single hatch represents the maximum extents of the data with the same level of low uncertainty.

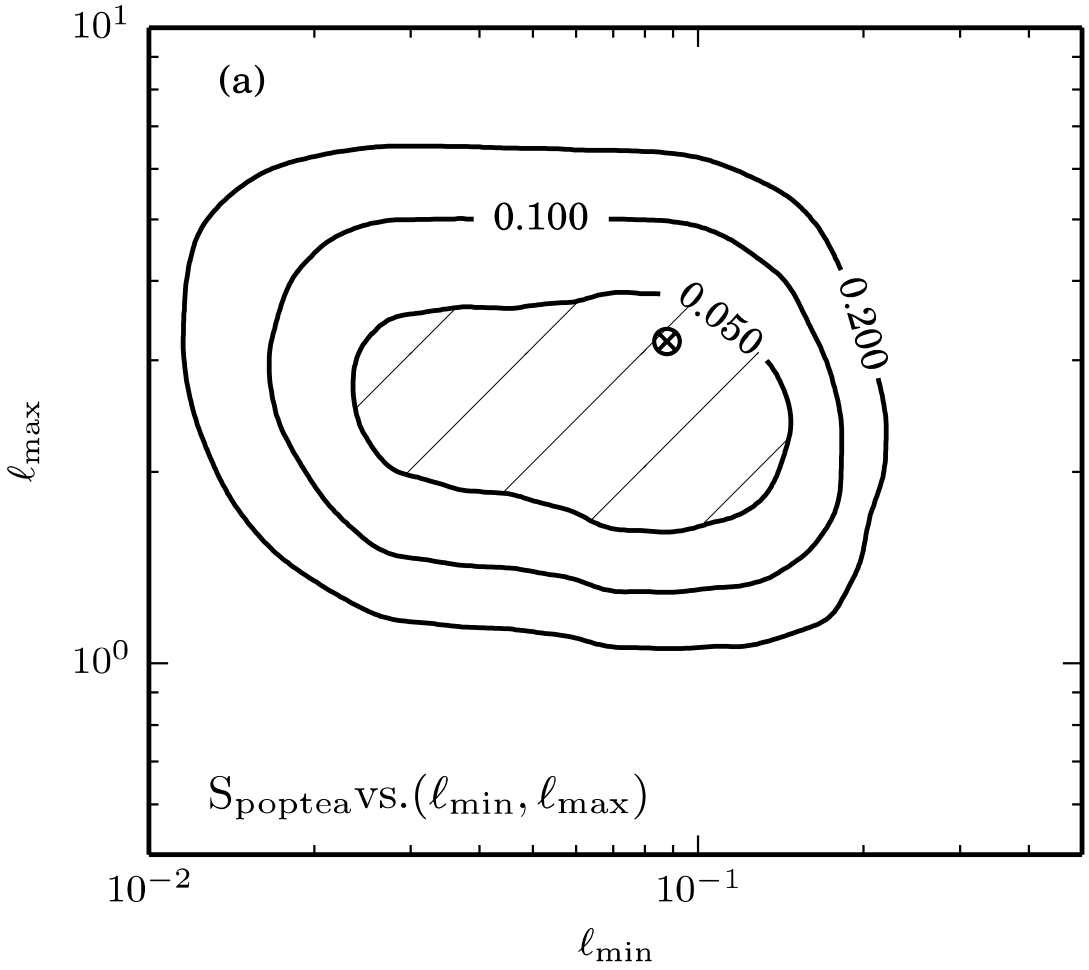

Figure 5.9: The contour plot shows the overall fitting uncertainty as a function of the Bias-LR observational data subsets. The hatched area illustrates the spread of data subsets that have a similar level of uncertainty. The optimal data subset ⊗ was found by minimizing ⊗ .

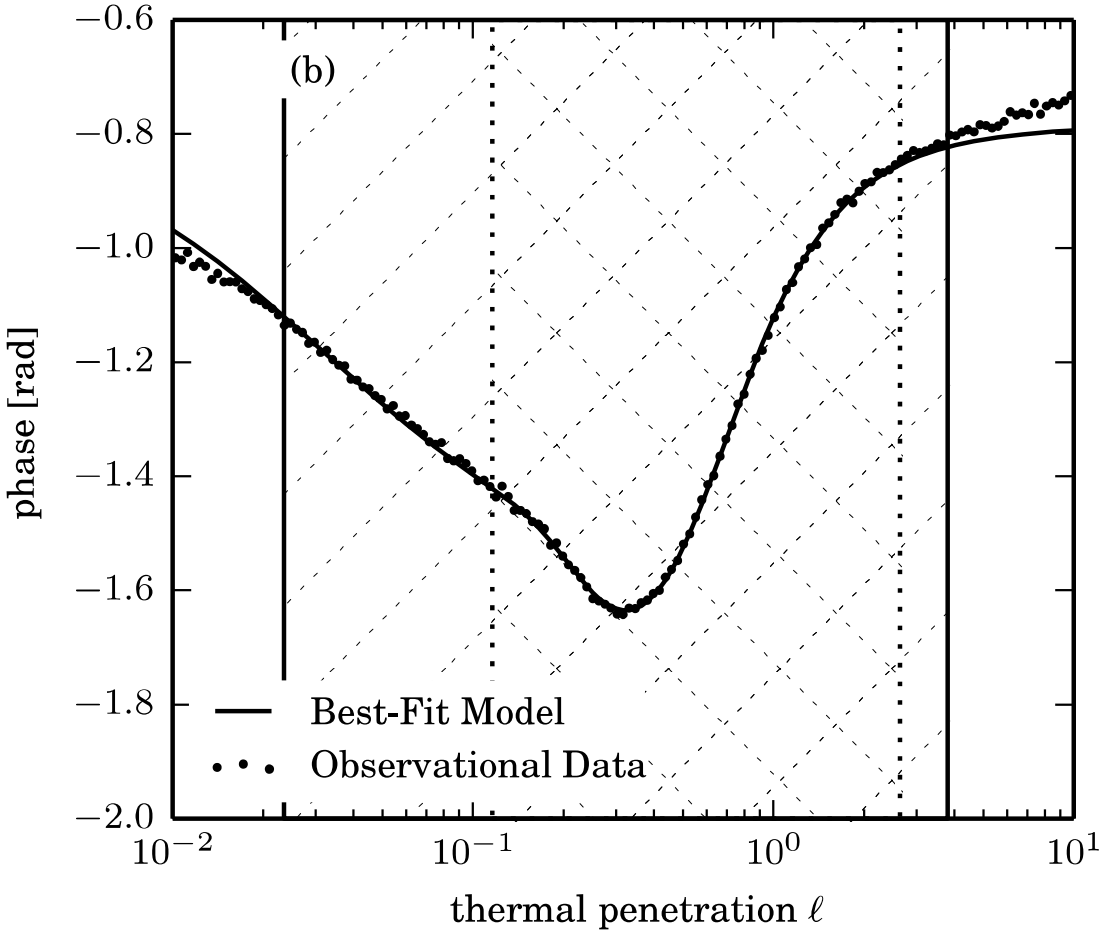

Figure 5.10: Bias-LR observational data shown with the model results for best-fit parameters estimates obtained from the optimized data subset ⊗ (as demarcated by cross-hatch). The single hatch represents the maximum extents of the data with the same level of low uncertainty.

Table 5.1: Thermophysical properties of the TBC system. The emission ratio is $E_1 = 42$. The coating has perfect thermal contact with the substrate.

Layer	$L\,(\mu\mathrm{m})$	$k\left(\frac{\mathrm{W}}{\mathrm{m}\cdot\mathrm{K}}\right)$	$\rho C\left(\frac{\mathrm{J}}{\mathrm{cm}^3\cdot\mathrm{K}}\right)$	Λ [a b]	a [b]	γ [b]
Coating	71.70	1.44	2.10	0.57	2.320	3.801
Substrate	∞	12.70	3.44	-	-	-

[a]The laser optical penetration depth $\delta = 40.9\,\mu\mathrm{m}$ is nondimensionalized by the coating thickness.

[b]Dimensionless unit.

Table 5.2: Best-fit results and PIE uncertainty analysis. The observational data consists of the full range of thermal penetration depths: $0.01 \le \ell \le 10$.

Obs.error	$a_{sub}\left(x_{\mathrm{bf}}, x_u\right)$	$\gamma\left(x_{\mathrm{bf}}, x_u\right)$	$\Lambda\left(x_{\mathrm{bf}}, x_u\right)$	$E_1\left(x_{\mathrm{bf}}, x_u\right)$
Random	2.33 : 7.4%	3.81 : 35.6%	0.569 : 5.2%	42.03: 35.2%
Bias-L	2.38: 16.3%	3.75: 80.3%	0.545: 11.4%	34.48: 77.4%
Bias-R	2.39: 20.3%	5.72: 203%	0.560: 14.9%	56.94: 190%
Bias-LR	2.45: 23.6%	5.48: 233%	0.535: 16.9%	45.41: 220%

Table 5.3: These are the best-fit and PIE uncertainty results using an optimal observational data subset. The recommended thermal penetration sweep is given based on the observational data subsets that give a similarly level of uncertainty. The uncertainty is calculated using eq. (5.13) and does not reflect any asymmetries in the uncertainty bounds.

Obs. error	a_{sub} (x_{bf}, x_u)	$\gamma\ (x_{\mathrm{bf}}, x_u)$	$\Lambda\ (x_{\mathrm{bf}}, x_u)$	$E_1\ (x_{\mathrm{bf}}, x_u)$	$\ell_{\min}, \ell_{\max}$ (optimal)
Random	2.33 : 7.4%	3.79: 24.1%	0.569: 10.1%	41.73: 59.3%	0.010, 10.
Bias-L	2.34: 7.2%	3.83: 23.5%	0.557: 10.0%	39.44: 56.3%	0.018, 10.
Bias-R	2.32: 6.2%	4.20: 32.3%	0.569: 6.6%	45.39: 37.2%	0.010, 3.4
Bias-LR	2.38: 8.3%	4.52: 35.2%	0.547: 10.9%	41.73: 60.3%	0.024, 3.8

Chapter 6 Two Color Pyrometry for Thermal Di usivity and Thermal Conductivity Measurements

6.1 Introduction

In many thermal diffusivity measurements, analysis of the temperature response is limited to the phase-response because of the difficulty in calibrating the absolute temperature scale [98], [148]. However, temperature scales measurements have long been used to determine thermal conductivity [149] through Fourier's Law [59], [64]:

$$k \sim Q\frac{\Delta x}{\Delta T} \tag{6.1}$$

where Q is the heat flow and Δx is a characteristic spatial scale over which there occurs a characteristic temperature drop ΔT. Therefore, just as the phase-response may be used to resolve thermal diffusivity, observing the amplitude-response may be used to resolve thermal conductivity, if temperature measurements are calibrated.

Surface temperatures can be determined by pyrometry from thermal emission measurements if the surface emissivity of a sample is known [150]. However, the variability of surface conditions makes it difficult to know the emissivity of the surface *a priori*. Two-color pyrometry can be used to eliminate the emissivity dependency of the measurement, if the two emission wavelengths selected for measurement are sufficiently close [151]. In this study, an approach to using two-color pyrometry is developed to determine the steady-state temperature and harmonic temperature amplitudes of the sample during harmonic heating. The goal is to be able to exploit additional information from the amplitude-response of the sample to heating, to better inform thermal property measurements. In this manner, it should be possible to determine both the thermal diffusivity and thermal conductivity of the sample in a single set of measurements, even when the sample is monolithic.

In order to implement and test the utility of making two-color amplitude-response measurements in the poptea method, this study develops a thermal and emission model

for a finite disk harmonically heated by a surface absorbing Gaussian laser beam. Experimental measurements were carried out on Poco graphite disks of different thickness.

6.2 Photothermal Modeling

6.2.1 Model for temperature field

A parameter estimation algorithm to determine the thermal diffusivity and thermal conductivity of a sample requires a model to interpret experimental observations. The model presented in this section describes thermal transport through a disk heated by a harmonically modulated optical beam. The model solves for the phase and amplitude of the harmonically sustained temperature field in which the phase is measured with respect to the modulated heating source.

The heat conduction equation in cylindrical coordinates is used to describe sample heating by an optical beam centered on the axis of symmetry. It is assumed that the thermal conductivity is not temperature-dependent and is isotropic with respect to the radial and axial directions. The time dependent temperature field $T(r,z,t)$ is described by the heat equation, which is expressed in spatially dimensionless coordinates as:

$$\frac{\partial^2 T}{\partial z^2}+\left(\frac{1}{r}\frac{\partial T}{\partial r}+\frac{\partial^2 T}{\partial r^2}\right)=\frac{R_{heat}^2}{\alpha}\frac{\partial T}{\partial t} \tag{6.2}$$

The radial coordinate r and the axial coordinate z have been made dimensionless by the $1/e$ radius of the Gaussian heating beam R_{heat}. The model assumes that moving radially away from the heating beam, the temperature field approaches the steady-state value of T_o, that the front optically heated surface and peripheral edge of the sample are exposed to convection, and that the back surface of the sample is adiabatic. Therefore, the four boundary conditions to be imposed on the heat equation for a disk with a finite thickness L and radius R are:

$$\begin{aligned} \left[\frac{\partial T}{\partial z} + Bi_1\left(T - T_o\right)\right]_{z=w} &= \frac{Q_{heat}}{\pi R_{heat} k} e^{-r^2} \\ \left.\frac{\partial T}{\partial r}\right|_{r=0} &= 0 \\ \left.\frac{\partial T}{\partial z}\right|_{z=0} &= 0 \\ \left[\frac{\partial T}{\partial r} + Bi_2\left(T - T_o\right)\right]_{r=s} &= 0 \end{aligned} \tag{6.3}$$

where w and s are the nondimensional thickness and radius of the disk and the heat absorbed by the sample is Q_{heat}. Note, that $z = w$ is the surface of the disk heated by the optical beam centered at $r = 0$. Convective heat transfer is described by a coefficient h, as presented in terms of the Biot numbers,

$$Bi_1 = \frac{h_1 R_{heat}}{k} \tag{6.4}$$

at the heating surface and

$$Bi_2 = \frac{h_2 R_{heat}}{k} \tag{6.5}$$

at the peripheral edge. See Figure 6.1 for an illustration of the heat conduction problem.

The temporal absorbed heating Q_{heat} rate can be decomposed into a steady-state and harmonic components using the expression:

$$Q_{heat} = \bar{Q}_{heat} + re\left\{\frac{m}{2-m}\bar{Q}_{heat}e^{i\omega t}\right\} \tag{6.6}$$

where $\bar{Q}_{heat}$ is the steady heating power absorbed by sample, m is the modulation depth $(0 \le m \le 1)$ and ω is the angular frequency of heating $(\omega = 2\pi f)$.

Heat conduction is described by a linear differential equation, which allowed the temperature field to be decomposed into steady-state and harmonically sustained fields using the method of superposition [152]:

$$T(r,z,t) = \bar{T}(r,z) + T^*(r,z,t) \tag{6.7}$$

So long as the resistance to heat spreading is small, the steady-state temperature solution can be taken as a constant $\bar{T}(r,z) = T_o$ that depends on the steady-state heat losses due to heat convection and radiation.

The harmonically sustained temperature field can be expressed in terms of a complex variable $\tilde{T}(r,z)$ using the method of complex combination [153], through the relation:

$$T^*(r,z,t) = re\left\{\tilde{T}(r,z)e^{i\omega t}\right\} \tag{6.8}$$

The problem for the complex temperature field can be made dimensionless with the following definition:

$$\tilde{\theta} = \frac{R_{heat}k}{\bar{Q}_{heat}}\tilde{T} \tag{6.9}$$

In this manner, the conduction equation, eq. (6.2) becomes:

$$\frac{\partial^2\tilde{\theta}}{\partial z^2} + \left(\frac{1}{r}\frac{\partial\tilde{\theta}}{\partial r} + \frac{\partial^2\tilde{\theta}}{\partial r^2}\right) = \frac{i}{\ell^2}\tilde{\theta} \tag{6.10}$$

and the boundary conditions becomes:

$$\begin{aligned}
\left[\frac{\partial\tilde{\theta}}{\partial z}+Bi_1\tilde{\theta}\right]_{z=w} &= \frac{m}{2-m}\frac{\exp\left(-r^2\right)}{\pi} \\
\left.\frac{\partial\tilde{\theta}}{\partial r}\right|_{r=0} &= 0 \\
\left.\frac{\partial\tilde{\theta}}{\partial z}\right|_{z=0} &= 0 \\
\left[\frac{\partial\tilde{\theta}}{\partial r}+Bi_2\tilde{\theta}\right]_{r=s} &= 0
\end{aligned} \tag{6.11}$$

where a radial thermal penetration depth has been defined by:

$$\ell = \frac{\sqrt{\alpha/2\pi f}}{R_{heat}} \tag{6.12}$$

The governing equation, eq. (6.10), with boundary conditions, eq. (6.11), can be integrated using separation of variables. Furthermore, assuming

$$\int_0^{\infty}\exp\left(-r^2\right)J_0\left(\lambda_n r\right)rdr = \int_0^{s}\exp\left(-r^2\right)J_0\left(\lambda_n r\right)rdr \tag{6.13}$$

the complex temperature field solution is found to be:

$$\tilde{\theta}\left(r,z\right) = \sum_n^{\infty} C_n J_0\left(\lambda_n r\right)\cosh\left(\tilde{\lambda}_n z\right) \tag{6.14}$$

where the coefficients are expressed by

$$C_n = \frac{1}{\tilde{\lambda}_n \sinh\left(\tilde{\lambda}_n w\right) + Bi_1 \cosh\left(\tilde{\lambda}_n w\right)} \frac{m}{(2-m)} \frac{\exp\left(-\frac{\lambda_n^2}{4}\right)}{\pi s^2 \left[J_0^2\left(\lambda_n s\right) + J_1^2\left(\lambda_n s\right)\right]}$$

with (6.15)

$$\tilde{\lambda}_n = \sqrt{\frac{i}{\ell^2} + \lambda_n^2}$$

where the transcendental equation for λ_n is given by:

$$\lambda_n s J_1\left(\lambda_n s\right) - Bi_2 s \cdot J_0\left(\lambda_n s\right) = 0 \tag{6.16}$$

6.2.2 Model for thermal emission

The thermal emission from a harmonically sustained temperature field must be interrogated to interpret detector measurements. The sample is assumed to be optically thick to the detector wavelength. The detector views a spot which is centered on the optical heating beam $(r = 0, z = w)$ and that has a radius

$$r_e = \frac{R_e}{R_{heat}} \tag{6.17}$$

Hemispherical emission from the heated area viewed by the detector can be integrated for the result:

$$\left\langle E_\lambda \right\rangle = \pi \int_0^{r_e} I_\lambda \cdot 2\pi r \cdot dr \tag{6.18}$$

The radiative intensity from the sample can be described by a Taylor series expansion about the steady-state temperature $\bar{T}$ such that

$$I_\lambda = \varepsilon_\lambda \left[I_{\lambda b}\left(\bar{T}\right) + \left.\frac{dI_{\lambda b}}{dT}\right|_{\bar{T}} T^* + \ldots \right] \tag{6.19}$$

where ε_λ is the surface emissivity, and λ is the emission wavelength. For simplicity of presentation, it is useful to adopt Wien's approximation of the Plank function to approximate the black body radiative intensity:

$$I_{\lambda b}\left(\bar{T}\right) \approx \frac{C_1}{\pi\lambda^5} e^{-\frac{C_2}{\lambda \bar{T}}} \quad \left(\frac{C_2}{\lambda \bar{T}} \gg 1\right) \tag{6.20}$$

where $C_1 = 3.7418\text{e-}16\ \mathrm{W \cdot m^2}$ and $C_2 = 0.01439\ \mathrm{m \cdot K}$ [150]; however, use of Wien's approximation is discretionary. Additionally, it is assumed that the amplitude of the temperature fluctuations $\left|\tilde{T}\right|$ is sufficiently small compared to $\bar{T}$ that only the first two terms in the Taylor series equation, eq. (6.19), are needed to describe the radiative intensity. Substituting in Wien's approximation, eq. (6.20), into the linearized radiative intensity, eq. (6.19), yields

$$I_\lambda = \varepsilon_\lambda I_{\lambda b}\left(\bar{T}\right)\left[1 + \frac{C_2}{\lambda \bar{T}^2} T^*\right] \quad \left(\left|\tilde{T}\right| \ll \bar{T}\right) \tag{6.21}$$

Using the radiative intensity, eq. (6.21), the complex hemispherical emission from the sample surface is found to be:

$$\left\langle E_\lambda \right\rangle = \varepsilon_\lambda \int_0^{r_e} \overline{I}_{\lambda,b} \cdot \left(1 + \frac{C_2}{\lambda \overline{T}^2} \tilde{T}\left(r, z = w\right) \right) \cdot 2\pi r \cdot dr \tag{6.22}$$

By virtue of the Taylor series linearization, total emission from the sample can be decomposed into the steady-state $\left\langle \overline{E}_\lambda \right\rangle$ and harmonic $\left\langle \tilde{E}_\lambda \right\rangle$ contributions:

$$\left\langle E_\lambda \right\rangle = \left\langle \overline{E}_\lambda \right\rangle + \left\langle \tilde{E}_\lambda \right\rangle \tag{6.23}$$

where

$$\left\langle \overline{E}_\lambda \right\rangle = r_e^{\,2} \pi^2 \varepsilon_\lambda \overline{I}_{\lambda,b} \tag{6.24}$$

and

$$\left\langle \tilde{E}_\lambda \right\rangle = r_e^{\,2} \pi \varepsilon_\lambda \overline{I}_{\lambda,b} \left(\frac{C_2}{\lambda \overline{T}^2} \left\langle \tilde{T}_{r_e} \right\rangle \right) \tag{6.25}$$

where the average harmonic component of the surface temperature viewed by the detector is defined as

$$\left\langle \tilde{T}_{r_e} \right\rangle = \left(\frac{\overline{Q}_{heat}}{R_{heat} k} \right) \frac{1}{r_e^{\,2}} \int_0^{r_e} \tilde{\theta}(r, z = w) \cdot 2r \cdot dr \tag{6.26}$$

The detector measurements of the phase and the amplitude of harmonically-sustained thermal emission can be related to the surface temperature conditions of the sample during measurements using eq. (6.25). In the limited case where the detector view radius is much smaller than the beam radius, the phase of thermal emission can then be evaluated in the limit of $r_e \ll 1$, for which the average harmonic surface temperature, eq. (6.26), becomes:

$$\left\langle \tilde{T}_{r_e \ll 1} \right\rangle = \left(\frac{\bar{Q}_{heat}}{R_{heat} k} \right) \tilde{\theta}(r = 0, z = w) \tag{6.27}$$

For the limit of $r_e \ll 1$, the phase of emission may be evaluated from:

$$\phi_{phase} = \arg\left[\left\langle \tilde{E}_\lambda \right\rangle \right] = \arg\left[\tilde{\theta}\left(r = 0, z = w \right) \right] \tag{6.28}$$

the temperature amplitude may be evaluated from:

$$abs\left[\left\langle \tilde{E}_\lambda \right\rangle \right] = \Delta \cdot abs\left[\tilde{\theta}(r = 0, z = w) \right] \tag{6.29}$$

and the temperature scale, Δ

$$\Delta = \frac{\bar{Q}_{heat}}{R_{heat} k} \tag{6.30}$$

It is important to note that the thermal diffusivity of the sample α influences both the phase and the amplitude of the harmonic temperature through the variable describing thermal penetration depth. However, the thermal conductivity k affects only the amplitude of harmonic temperature, not phase.

6.3 Harmonically-Sustained Two-Color Pyrometry

6.3.1 Model for Surface Temperature Observations

Although the thermal diffusivity can be determined solely from the phase of thermal emission of the sample with eq. (6.28), it should be possible to also estimate the thermal conductivity using the harmonic temperature amplitude with eq. (6.29).

To perform pyrometry of the sample surface without knowledge of the emissivity ε_λ, two-color pyrometry is employed. When two wavelengths of emission detection are sufficiently close, such that $\varepsilon_{\lambda 1} \approx \varepsilon_{\lambda 2}$, the signal ratio becomes independent to the emissivity. The ratio of emission signals is expressed by:

$$SR(t) = \frac{I_{\lambda 2}(t)}{I_{\lambda 1}(t)} \tag{6.31}$$

For the limiting case of $\left|\tilde{T}\right| << \overline{T}$, substituting in the radiative intensity, eq. (6.21), into the signal ratio, eq. (6.31) ,yields

$$\frac{\ln\left(SR(t)\right)-5\ln\left(\frac{\lambda_1}{\lambda_2}\right)}{\frac{C_2}{\lambda_1}-\frac{C_2}{\lambda_2}}=\frac{1}{\overline{T}}-\frac{re\left\{\tilde{T}e^{i\omega t}\right\}}{\overline{T}^2} \tag{6.32}$$

For the special case of $\left|\tilde{T}\right|=0$, the result given by the pyrometry equation, eq. (6.32), is the well-known two-color pyrometry equation [151]. For the case of harmonic heating, this pyrometry equation can be applied to determine the amplitude of surface temperature fluctuations $\left|\tilde{T}\right|$, in addition to the steady-state temperature $\overline{T}$, from two-color pyrometry measurements. For a harmonically-sustained temperature source, the LHS of eq. (6.32) is the normalized signal ratio and is obtained from a temporal measurement of surface emission; it is fitted to a function of the form $A+B\cos\left(\omega\cdot t\right)$ where

$$A=\frac{1}{\overline{T}} \tag{6.33}$$

and

$$B=-\frac{\left|\tilde{T}\right|}{\overline{T}^2} \tag{6.34}$$

In this way, the harmonic amplitude $\left|\tilde{T}\right|$ and steady-state temperature $\overline{T}$ can be resolved; see Figure 6.2 for an illustration of a fitted signal ratio.

6.4 Illustrative Experiments

6.4.1 Experimental Apparatus

The experimental implementation of a two-color pyrometer is illustrated in Figure 6.3. An ellipsoidal mirror collects the hemispherical emission from a small focused spot on the sample and redirects it to a Judson J10D Indium Antimonide (In-Sb) photodiode thermal detector. A Judson transimpedence current-to-voltage preamplifier provided a gain to the detector signal and the data were recorded using data acquisition software.

Although the photodiode has a peak detector wavelength at $5\,\mu m$, it is sensitive to IR radiation over the range of $2\,\mu m$ to $5.5\,\mu m$. In comparing the current photodetection system to the implementations described in [101], [154], the current setup filters emission reaching the detector with a Spectrogon bandpass filter having a center wavelength at either $4.081\,\mu m$ or $5.228\,\mu m$. These filters are interchanged to make thermal emission measurements at two wavelengths.

The samples were mounted on a minimal-contact area steel vacuum chuck and positioned as described in the experimental apparatus in Figure 6.4. The optical heating was provided by a Synrad Firestar t60 CO_2 laser at an operating wavelength of 10.6μm. From the data acquisition software, a Stanford Research Systems DS345 function generator controlled the IntraAction AGM-406B acoustic-optical modulator (AOM) driver. This allowed for precise control of the laser beam harmonic modulation

frequency f, and the modulation depth $m = 0.7143$. The laser power was characterized using a Scientech Large-Aperture Calorimeter (model 380402) and represents a 2-minute time-averaged laser power output, $Q_{laser} = 10.34\ \mathrm{W} \pm 5\%$. The actual heat absorbed by the samples was calculated after making separate reflectivity measurements.

The temperature amplitudes were measured using the experimental apparatus described in this section and the two-color pyrometry method described in Section 6.3.1. The emission from the sample was isolated by recording and subtracting the background emission. The true sample SR was measured after calibrating for the thermal detector SR gain (g)

$$SR_{\text{true}} = g \cdot SR_{\text{detector}} \tag{6.35}$$

which was determined by making measurements against a known black-body source

$$g = \frac{SR_{BB}}{SR_{\text{detector}}} \tag{6.36}$$

where SR_{BB} was evaluated using the steady state simplification of eq. (6.32), the filter wavelengths, and the source temperature. The detector gain used for this investigation was $g = 0.7886 \pm 1.1\%$.

6.4.2 Samples

Poco graphite was chosen to demonstrate the two-color pyrometry and thermal property measurements based on the following criteria: it is a material with extensive literature references, it remains stable after repetitive measurements for a prolonged period (below the 450°C oxidation threshold), and has full compatibility with our thermal modeling. As oppose to pyrolytic graphite, ultra-fine graphite is the ideal material because it has highly isotropic thermal properties due to a lack of grain orientation. The graphite material has high emittance at the detector wavelengths, high absorption at the laser wavelength, and is optically thick in the IR spectrum. This ensures that the laser optical heating occurs at the surface of the sample and the emission viewed by the detector is also from the surface.

This work uses a Poco Graphite EDM-3 that is manufactured by Entegris Inc. The thermal properties for EDM-3 were available by the Entegris Inc. literature [155] and these were summarized by Maradia et al. [156] and used for electron discharge machining thermal modeling. However, a literature review also found an international round-robin set of thermal diffusivity measurements (9 investigators, various modulated and pulse heating methods) and thermal conductivity measurements (5 investigators, 5 methods) performed on Poco Graphite grade AXM-5Q. Both Poco grades are ultra-fine and highly isotropic graphites that are made with particle sizes of $5\,\mu m$. Since AXM-5Q has been extensively characterized, it was desirable to use this grade as a reference for the EDM-3 PopTea thermal property measurements.

Graphite has high electrical conductivity, the Wiedemann-Franz law [157] has been used to relate thermal conductivity k to the electrical resistance σ of graphite [158]–[162] and is

$$k = \sigma T \Lambda \tag{6.37}$$

where the evaluation temperature is T and the Lorenz Ratio is Λ. To estimate the difference in thermal conductivity between the two graphite grades, assume a constant Lorenz ratio at a given temperature

$$\frac{k_{\text{EDM-3}}}{k_{\text{AXM-5Q}}} = \frac{\sigma_{\text{EDM-3}}}{\sigma_{\text{AXM-5Q}}} \tag{6.38}$$

The electrical resistance of the two grades is provided by the manufacturer's literature [155] and is presented in Table 6.1. Evaluating eq. (6.38) yields a thermal conductivity and a thermal diffusivity $(\alpha = k/\rho C_p)$ difference of approximately 4%. Since this is well within the expected thermal conductivity scatter $\pm 7.5\%$ and thermal diffusivity scatter $\pm 5.7\%$ reported by Minges [163] in the round-robin investigation, AXM-5Q was selected as the reference material for this work's thermal property evaluation.

The sample preparation procedure was as followed: All samples were cut from a POCO Graphite EDM-3 diameter rod. Once cut from the rod, each one was ultrasonically cleaned for 5 minutes in de-ionized (DI) water. The samples were then polished using 600-grit, 800-grit, 1200-grit fine-grained sandpaper; between each

polishing step, the sample was ultrasonically cleaned in 5 minutes of DI water. After polishing, a final ultrasonic cleaning to remove surface oils was done using fresh methanol in three 5-minute intervals. The samples were then dehydrated in air using a furnace at atmospheric pressure. Using this process, three disk-shaped samples were prepared with a $25.4\ \text{mm}$ diameter and thicknesses 0.424 mm, 0.894 mm, 1.620 mm.

6.4.3 Measurement Results and Discussion

A set of measurements for each sample was performed by varying the modulation frequency of the laser over a wide range of frequencies ($1.0\ \text{Hz}$ to $11585.2\ \text{Hz}$). Each frequency corresponds to a different thermal penetration depth for heating. At each laser modulation frequency, the phase of emission ϕ and the temperature amplitude $\left|\tilde{T}\right|$ was measured. Figure 6.5, Figure 6.6 and Figure 6.7 shows the temperature amplitudes and phase of emission measured from the three disk samples and Table 6.2 reports the measured steady-state temperatures $\overline{T}$.

The extended range of laser modulation frequencies results in an axial thermal penetration

$$\ell_z = \frac{\sqrt{\alpha / 2\pi f}}{L} \tag{6.39}$$

that probes from the near surface to the through-thickness length scale of the disks. For the three samples tested, the phase of emission approaches $\pi/4$ in the high frequency

limit as $\ell_z \ll 1$. For very shallow thermal penetration measurements, the far boundary condition effectively moves infinitely away from the source of heat and a sample will appear to behave as a semi-infinite disk or slab. In this limit, the phase of emission loses sensitivity to thermal diffusivity as the axial length scale is obscured. For very thin samples, a higher frequency is needed in order to approach the semi-infinite behavior so that the axial thermal penetration, eq. (6.39), satisfies $\ell_z \ll 1$. A discussion on the radial thermal penetration and its interaction with the peripheral boundary is reserved for Appendix D.

Thermal diffusivity was measured by regression analysis on experimental phase of emission measurements and thermal conductivity measured by regression analysis on the temperature amplitudes. The model used for the analysis was developed in Section 6.2.2. To interpret the experimental data, the small detection area model, eq. (6.28), was used because the detector view radius was much smaller than the heating beam radius. For the model evaluations a Biot number equal to zero was used to represent the heated surface and radial boundaries; a discussion on the Biot number is provided in Appendix C. The phase of emission is only a function of thermal penetration, eq. (6.12), in which thermal diffusivity is the only unresolved parameters; however, this investigation also resolved heating radius as part of the fitting process. The physical depth w and radius s of the disks were known *a priori*.

The phase regression analysis was carried out using a Levenberg-Marquardt nonlinear parameter estimation algorithm to estimate thermal diffusivity and the heating beam radius. The model conformity between the model predictions ϕ_i and the observational phases $\hat{\phi}_i$, defined as the biased sample variance, was the minimization function:

$$S(\boldsymbol{x}) = \frac{1}{N}\sum_{i=1}^{N}\left(\hat{\phi}_i - \phi_i(\boldsymbol{x})\right)^2 \tag{6.40}$$

where the i-index reflects the N unique modulation laser frequencies that comprise a set of measurements. Figure 6.5, Figure 6.6 and Figure 6.7 and Table 6.2 has the fitting result for which thermal diffusivity, and the beam radius were fitted. The regression-based sensitivity method described in [164] and similarly used by Yu and Bennett [21] determined confidence intervals (CI) for the fitted parameters. Assuming a 90% confidence level, an estimate of the standard error is derived from the CI [165]. This uncertainty approach identifies the confidence intervals by exploring the uniqueness of the fit with respect to varying the unknown parameters around their best-fit and reevaluating the regression analysis. The three samples tested achieved a steady state temperature of $210.4°\mathrm{C}$, $203.6°\mathrm{C}$, $189.5°\mathrm{C}$ for the 0.424 mm, 0.894 mm, and 1.620 mm samples, respectively. Although the samples were tested with same laser heat flow and modulation, the temperature difference should represent the small differences in heat losses to the environment and sample mount. These temperatures were used to

calculate the expected thermal diffusivity based on Minge's round-robin measurement summary [163]. Minge summarized the results of the round-robin measurements by developing a temperature-dependent experimental correlation for thermal diffusivity with a consistent uncertainty of 5.7%. The thermal diffusivity and uncertainty measurements are in close agreement with Minge's summary and the results are presented in Table 6.2.

The temperature amplitude regression analysis was also carried out using the Levenberg-Marquardt parameter estimation algorithm. The minimization function was reformulated as a weighted least squares by normalizing the residuals based on the model temperature scales:

$$S(\boldsymbol{x}) = \frac{1}{N}\sum_{i=1}^{N}\left(\frac{\hat{\tilde{T}}_i - \tilde{T}_i(\boldsymbol{x})}{\tilde{T}_i(\boldsymbol{x})}\right)^2 \tag{6.41}$$

so that each residual is weighted equally. The model evaluations used the thermal diffusivity and beam radius that were estimated from the phase of emission in addition to the other model parameters. This decoupled the thermal diffusivity and thermal conductivity estimation algorithms. The unknown parameter to be fitted was the temperature scale $\Delta = \left(\bar{Q}_{heat} / R_{heat} k\right)$ from eq. (6.30). The absorbed steady-state heat flow was found by measuring the laser power using a calibrated Scientech Large Aperture Calorimeter and making reflectivity measurements of the sample surface,

$$\bar{Q}_{heat} = (1-\Re)\bar{Q}_{laser} \tag{6.42}$$

The reflectivity measurements were made by using the ratio of the power readings reflected by a mirror and the highly polished samples,

$$\Re = \frac{Q_{sample}}{Q_{mirror}} \tag{6.43}$$

A measured reflectivity $\Re = 28.6\% \pm 2.6\%$ was used for this study; this reflectivity value is consistent with 25% reflectivity of a CO_2 laser on graphite coatings reported by Kruetz et al [166] and reflects a heat absorption of $\bar{Q}_{heat} = 7.383\ \mathrm{W} \pm 5.1\%$

The uncertainty for the thermal conductivity was calculated by first normalizing the temperature amplitudes by the best-fit predicted values

$$\breve{T}_i = \log\left(\frac{\hat{\tilde{T}}}{\tilde{\tilde{T}}_{i\,i}}\right) + 1 \tag{6.44}$$

From the normalized temperature amplitudes, the mean, standard deviation and number of measurements were used to calculate the 90% confidence limits; the confidence limits were used as the uncertainty of the temperature scale Δ. The uncertainty in the temperature scale u_Δ was then propagated through to thermal conductivity uncertainty using eq. (6.30) and the propagation of uncertainty [167]:

$$u_k = \sqrt{\left(\frac{(\Re-1)Q_{laser}}{R_{heat}\Delta^2}\right)^2 u_\Delta^2 + \left(\frac{(\Re-1)Q_{laser}}{R_{heat}^2\Delta}\right)^2 u_{R_{heat}}^2 + \left(\frac{1-\Re}{R_{heat}\Delta}\right)^2 u_{\bar{Q}_{heat}}^2 + \left(\frac{-Q_{laser}}{R_{heat}^2\Delta}\right)^2 u_\Re^2} \tag{6.45}$$

Figure 6.5, Figure 6.6, and Figure 6.7 has the best-fit temperature amplitudes and the resolved thermal conductivity and uncertainty is reported in Table 6.2. The thermal conductivity was found to be within the uncertainty scatter predicted by Minge's thermal conductivity summary. The overall uncertainty for thermal conductivity was $8.8\% - 13.8\%$ and it is higher than 7.5% uncertainty scatter observed by Minges [163].

The uncertainty for the two-color pyrometry measurements was also evaluated for the 0.892 mm sample by making eight steady state and harmonic emission measurements at a laser modulation frequency 64 Hz. The measured temperature was $476.3\ \mathrm{K} \pm 5.2\ \mathrm{K}$ and the temperature amplitude was $0.0929\ \mathrm{K} \pm 0.0268\ \mathrm{K}\left(28.8\%\right)$, the temperature amplitudes are shown in Figure 6.8. The thermal emission was collected as the sum of steady state and transient components; the thermal emission steady component had an uncertainty of approximately 0.8% and the emission amplitudes approximately 3.8%. An uncertainty analysis was developed in Appendix D to explain the large uncertainty in temperature amplitude. The propagation of uncertainty for steady state temperature is available as eq. (D.8), and temperature amplitudes as eq. (D.12). It was found that the large increase in temperature amplitude uncertainty is

driven, in part, by an uncertainty amplification factor that scales with the square of the steady state temperature, $\overline{T}^2$.

6.5 Conclusion

Harmonically-sustained two-color pyrometry has been presented as a technique for evaluating steady-state and surface temperature amplitudes from a harmonically-sustained thermal emission field. A photothermal analysis method for determining two independent thermal properties was developed by modeling a harmonically-sustained heat conduction and thermal emission model for single-layer disks. First, we showed how to solve for thermal diffusivity from the experimental phase of emission measurements; then, we used those results and the measured temperature amplitudes to resolve the thermal conductivity. The uncertainty associated with thermal diffusivity measurements are consistent with values reported in the literature; however, the uncertainty associated with thermal conductivity measurements had an uncertainty higher than the values reported in the literature for graphite.

This work demonstrates the effectiveness performing photothermal analysis on bulk specimens. The benefits of our approach is that it is a non-contact, nondestructive that only requires access to one side of the sample. These results demonstrate that it could be used in place of the thermal flash technique for making diffusivity measurements, however, reducing the noise in the temperature amplitudes would be

necessary in order to reduce overall uncertainty in the thermal conductivity measurements.

Figures and Tables

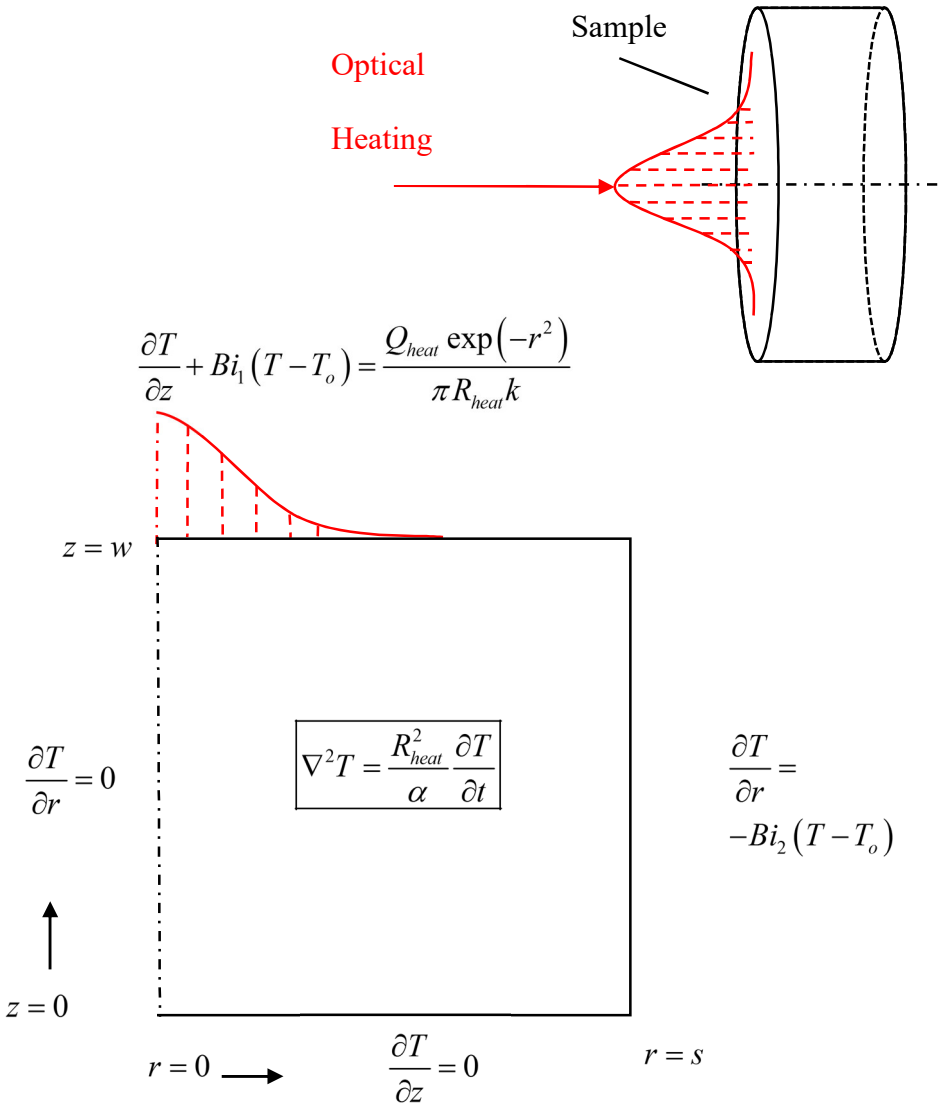

Figure 6.1: Nondimensional heat conduction model of a sample heated by a centered Gaussian optical heating beam.

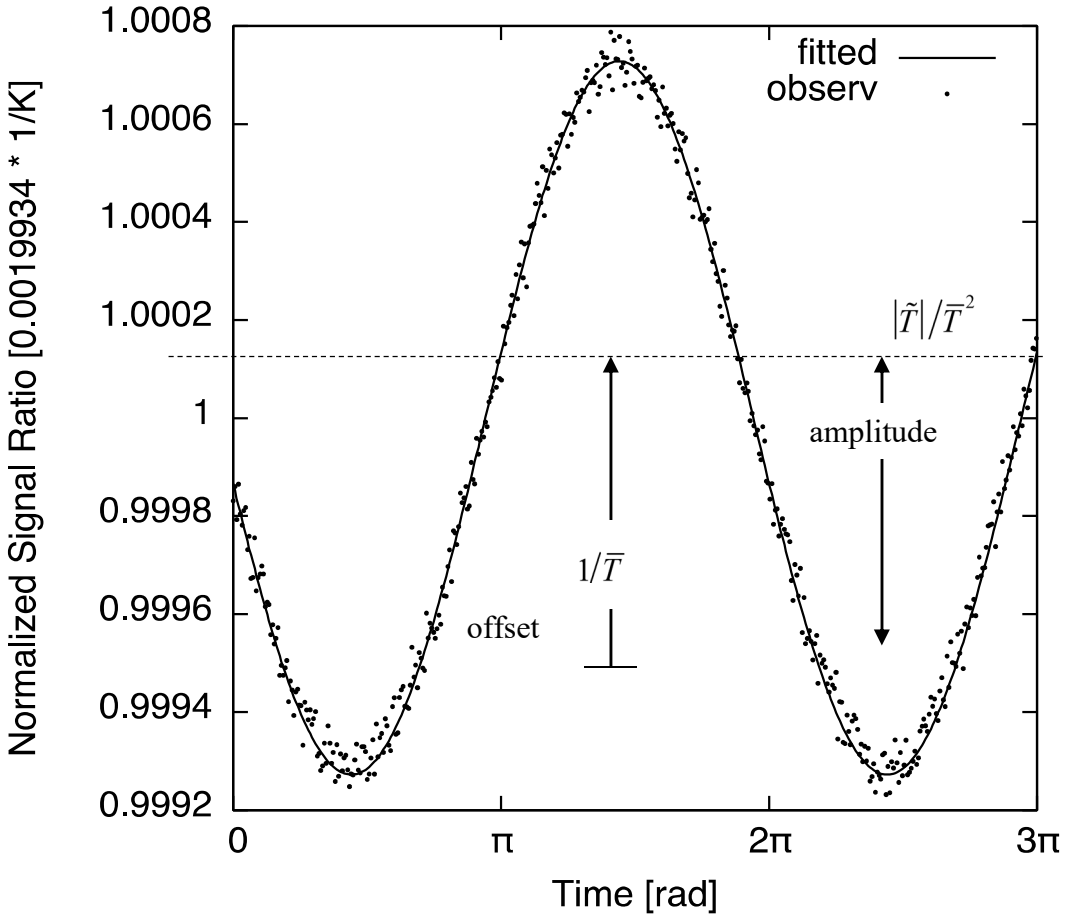

Figure 6.2: A sample pyrometry measurement to measure steady and temperature fluctuations at $16\,\mathrm{Hz}$. The steady-state temperature is resolved to $\bar{T} = 501.7\ K\ (228.5°\mathrm{C})$ and the harmonic temperature amplitude was $|\tilde{T}| = 0.365\ K$.

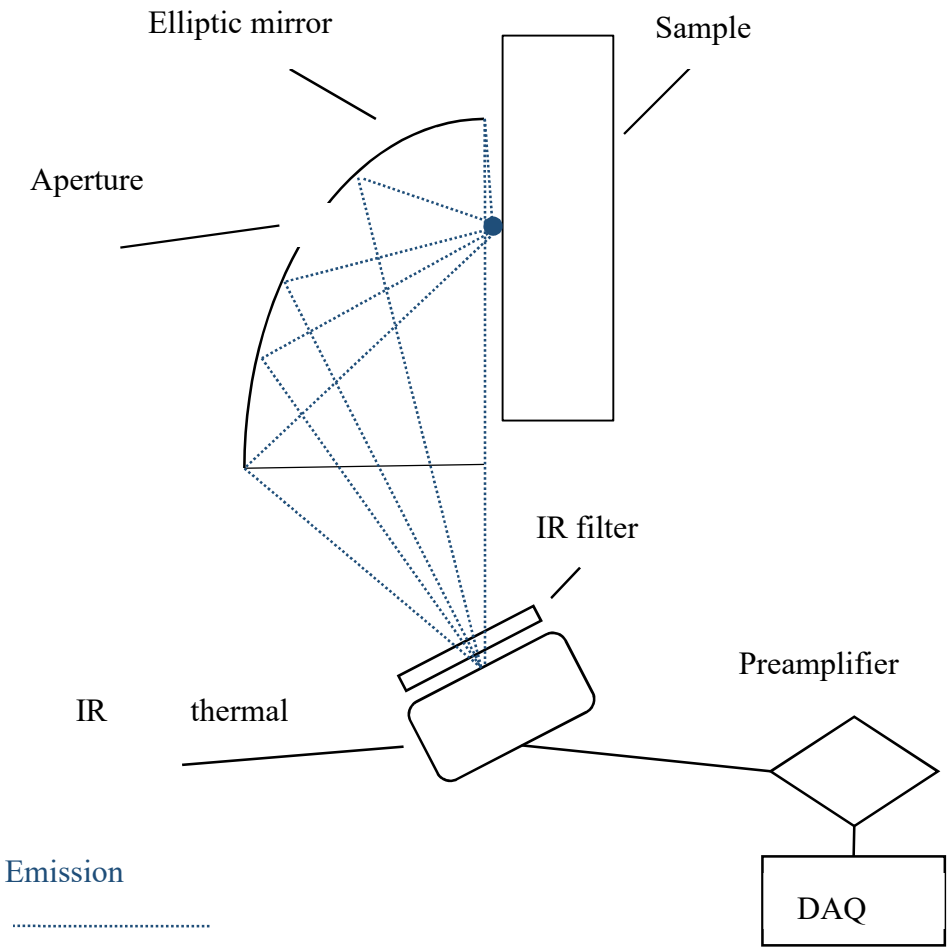

Figure 6.3: Two-color pyrometry experimental apparatus.

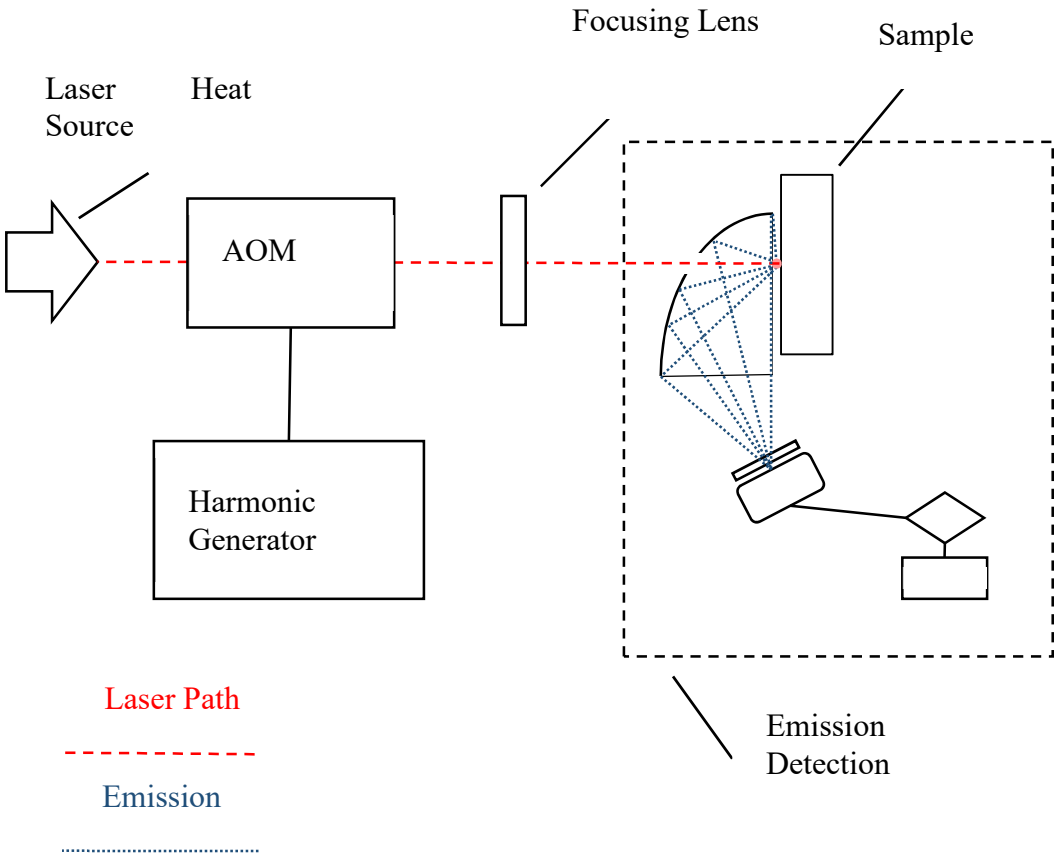

Figure 6.4: Experimental apparatus for harmonic heating of a specimen using a laser heat source.

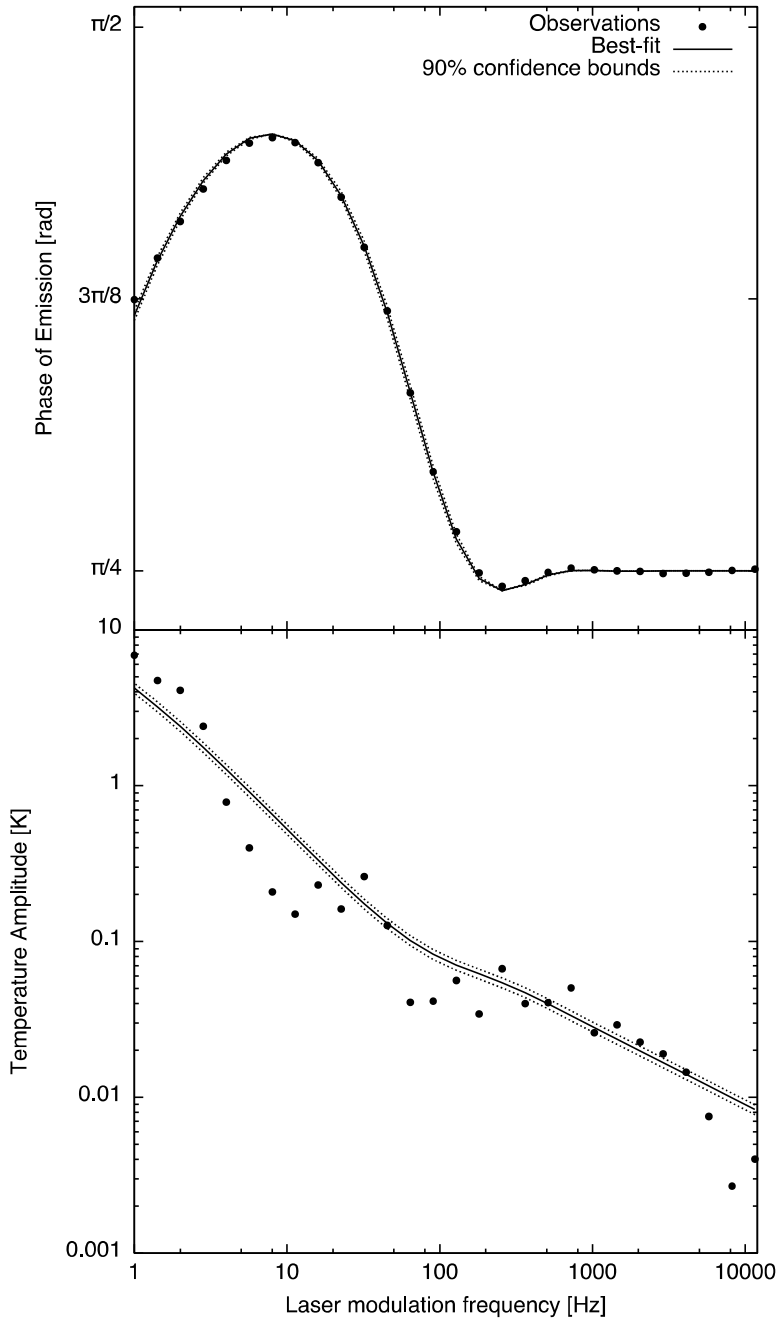

Figure 6.5: Phase and amplitude fitting with uncertainty bounds shown for the $L = 0.424$ mm sample.

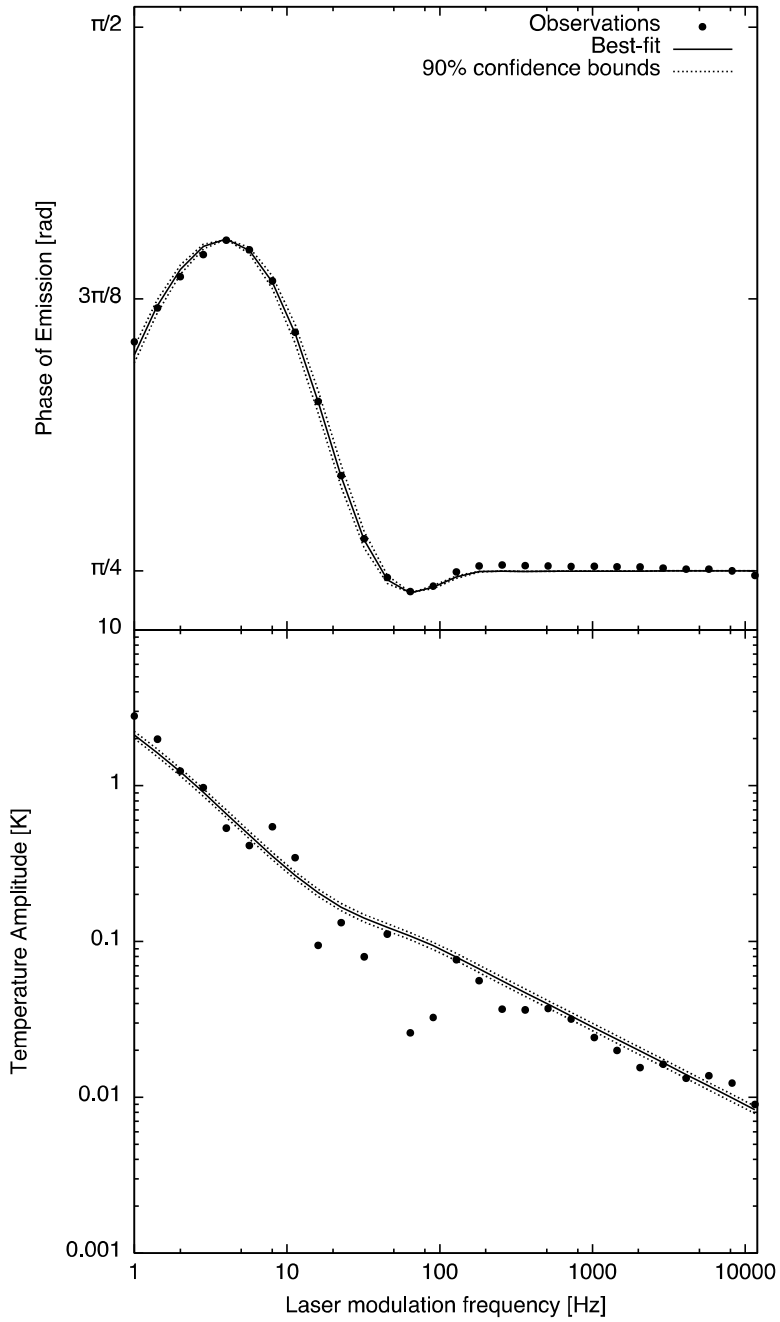

Figure 6.6: Phase and amplitude fitting with uncertainty bounds shown for the $L = 0.892$ mm sample.

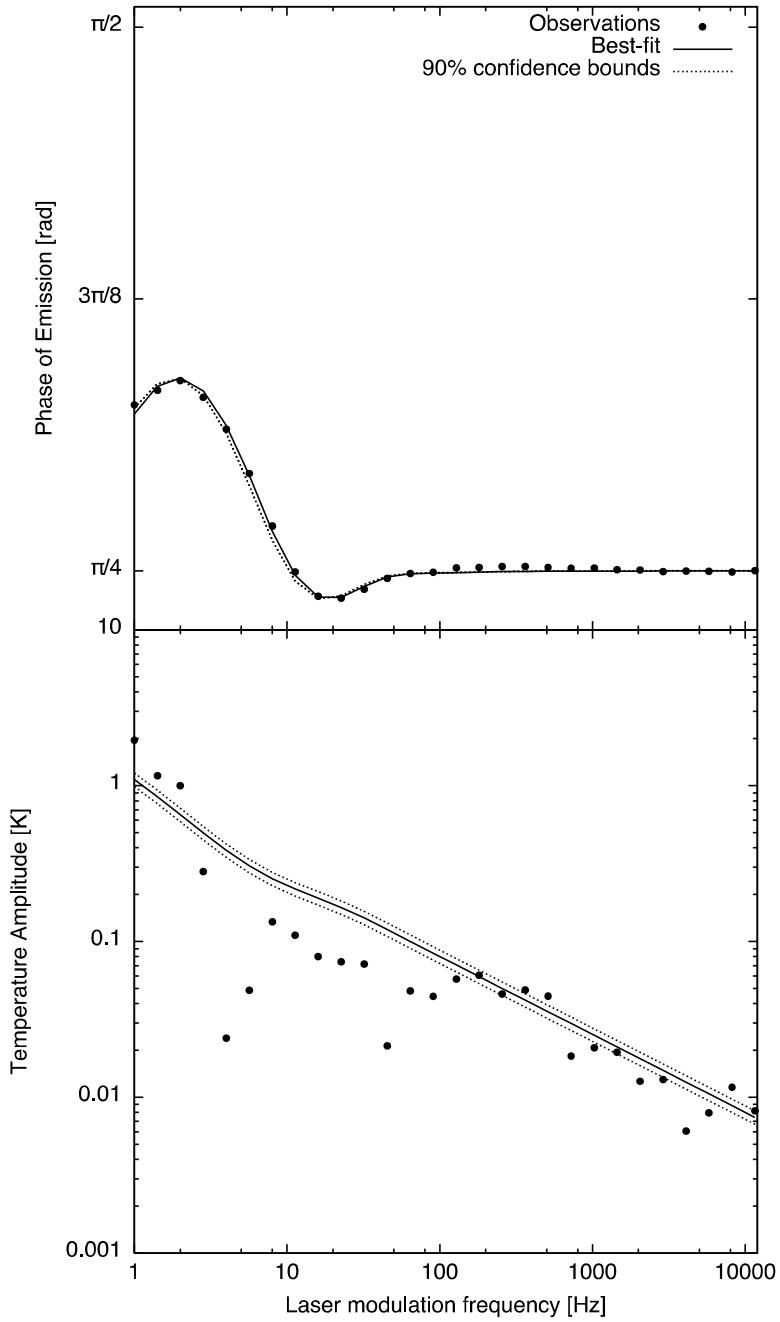

Figure 6.7: Phase and amplitude fitting with uncertainty bounds shown for the $L = 1.620$ mm sample.

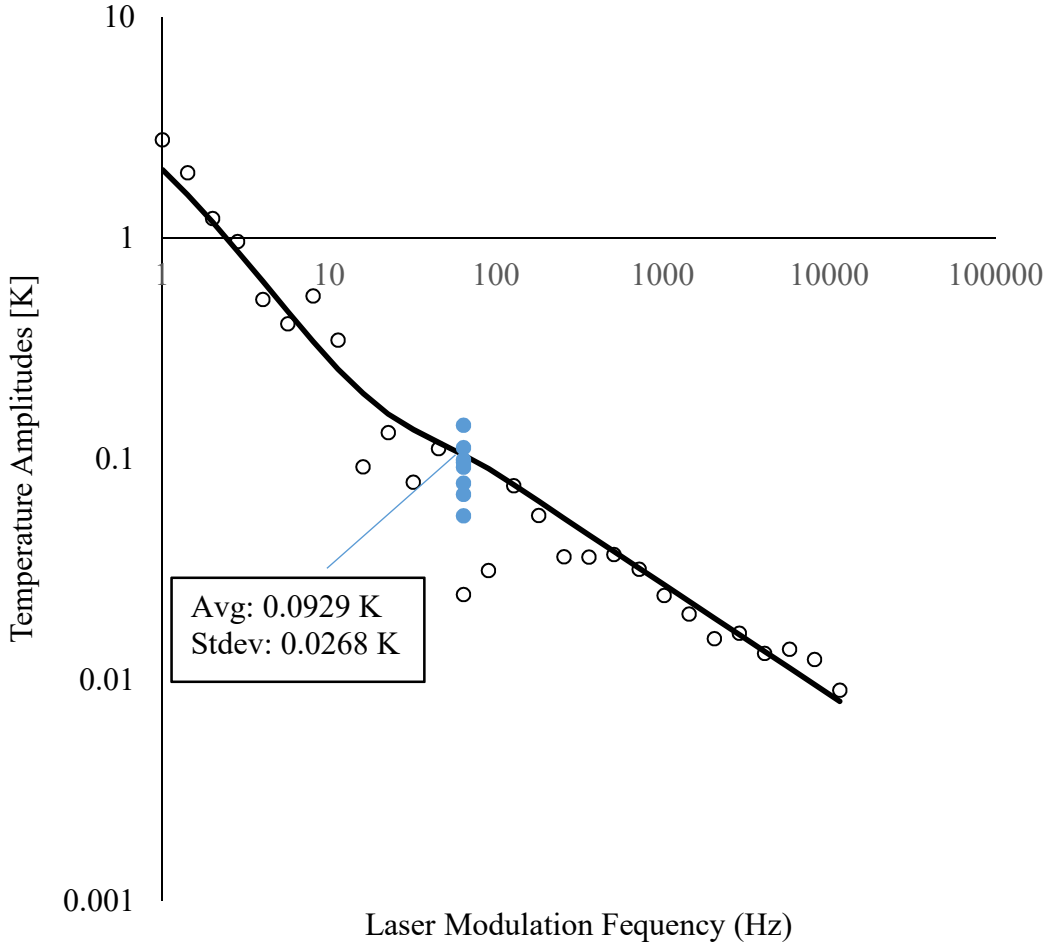

Figure 6.8: Temperature amplitudes for the 0.892 mm. The solid line is the best-fit model and the empty circles are the experimental measurements. The blue circles represent additional measurements taken at 64 Hz.

Table 6.1: Poco graphite grade comparison at room temperature.

Characteristic	**AXM-5Q**	**EDM-3**	
Apparent Density	1.757[a]	1.774[b]	$g \cdot cm^{-3}$
Average Particle Size	5[c]	5[d]	μm
Electrical Resistivity	1601[c]	1538[d]	μ·ohm·cm
Heat Capacity	721.4[c]	721.4[d]	$J/kg \cdot K$

[a] Reference [163]

[b] The bulk density was measured from several rods.

[c] Manufacturer Specification POCO AXM-5Q

[d] Manufacturer Specification POCO EDM-3

Table 6.2: Fitted parameters and literature reference comparison.

Sample		$\phi - fit$			$\tilde{T} - fit$	
Length	T_o	R_{heat}	α	α_{Ref} [e]	k	k_{Ref} [e]
mm	°C	mm	$\text{mm}^2 \cdot \text{s}^{-1}$	$\text{mm}^2 \cdot \text{s}^{-1}$	$\text{W} \cdot \text{m}^{-1}\text{K}^{-1}$	$\text{W} \cdot \text{m}^{-1}\text{K}^{-1}$
0.424	210.4	$6.3^{+2.9\%}_{-2.7\%}$	$38.1^{+3.0\%}_{-2.9\%}$	$40.8 \pm 5.7\%$	$91.4^{+10.5\%}_{-10.5\%}$	$90.6 \pm 7.5\%$
0.894	203.6	$6.3^{+2.5\%}_{-2.4\%}$	$43.2^{+3.3\%}_{-3.2\%}$	$41.7 \pm 5.7\%$	$94.9^{+8.8\%}_{-8.8\%}$	$91.5 \pm 7.5\%$
1.620	189.5	$6.3^{+2.0\%}_{-1.9\%}$	$42.2^{+3.8\%}_{-3.6\%}$	$43.5 \pm 5.7\%$	$104.1^{+13.8\%}_{-13.8\%}$	$93.3 \pm 7.5\%$

[e] Evaluated at the steady-state temperature, T_o, error shown is based on accuracy of experimental correlation from Reference [163]

Chapter 7 Conclusions

This dissertation examines fundamental issues underpinning robust thermal property measurements that are adaptive to non-specific, complex, and evolving sample characteristics using the Phase of Photothermal Emission Analysis (PopTea) method. This is part of the goal to make reliable thermal property measurements of intact and serviceable thermal barrier coatings systems (TBCs) on turbine hardware necessary to characterizing the degradation of TBC performance due to in-service conditions.

The PopTea method has a basis in modeling heat transfer through a coating perfectly adhered to a semi-infinite substrate and thermal models formulated with this assumption were found to lead to large uncertainties in measured thermal properties when making measurements on coatings deposited on substrates where transient heat transfer extended

beyond a well-defined substrate layer. It was found that using a generic subsystem model beyond the substrate layer allowed for the characterization of heat transfer beyond the extent of a finite substrate thickness. Experiments were carried out on a 323 μm thick air plasma spray (APS) TBC for conditions of a semi-infinite substrate and a 1.4 mm substrate with internal voids beyond the well-defined layer. It was demonstrated that the "thermal parameters" of the generic subsystem reflecting the heat transfer beyond the 1.4 mm substrate layer could be independently measured and used in differential PopTea measurement of the TBC to resolve the thermal conductivity and thermal diffusivity of a TBC coating. The results suggested the uncertainty of the differential PopTea measurements, with respect to conventional PopTea, can resolved thermal conductivity and thermal diffusivity to within 10% of each other.

The motivation for developing and experimentally supporting the differential PopTea approach was to increase the robustness of PopTea by reducing the uncertainty of thermal property measurements on gas turbine engine hardware. Since TBCs may be deposited on gas turbine engine components that have complex or unknown internal hardware configuration, this approach now makes it possible to create a set of independent reference measurements against a "bare" engine component and use those for differential PopTea measurements of a TBC on the same engine hardware configuration. The differential model developed in this dissertation would also facilitate multi-layer measurements on complex engine hardware by using a single unified thermal model for the analysis.

The need to address transient heat transfer beyond a well-defined substrate was due to the mismatch in the thermal modeling assumption of a semi-infinite substrate and the actual experimental conditions. In cases of high thermal conductive samples, the mismatch in the thermal modeling assumption of a semi-infinite radial dimension can also contribute modeling errors when radial thermal penetration begins to interactive with "ill-defined" heat transfer paths; it is recommended that future work investigate adaptive modeling to address this type of mismatch. Finally, additional mismatch between the thermal model and the coating system can occur at near surface length scales where surface roughness and contaminants can influence the behavior of the TBC system. This motivated an investigation of regression-based sensitivity analysis to address the generic mismatches between modeling and experimental data.

Use of poorly-fitted experimental data was shown to lead to large uncertainties in estimated thermal properties. The uncertainty in the thermal properties was accessed using a developed regression-based sensitivity analysis that combines the regression analysis and thermal modeling to report uncertainty in the parameters. This led to a measurement optimization method to minimize uncertainty by selectively filtering out experimental observations that deviated from a well-defined thermal model and selecting an optimal subset of the experimental observations for analysis. This was numerically tested by simulating a set of experimental measurements with bias-error at either end of the phase-spectra frequency sweep and evaluating the best-fit uncertainty. It was found that even in the presence of significant non-systematic bias-error, the algorithm was able to reduce

uncertainty to the level of random noise. The advantage of the measurement optimization method is that it does not depend on the development of any new thermal modelling to address model discrepancies and does not depend on a precise description of the type of experimental error. However, if characteristics of the experimental error are known *a priori* they should be used to adapt this method to a specific application in order to expedite the optimal data subset search. The implications of this method is that the model can be used to filter out "poor" data to increase measurement confidence. This means as a TBC system evolves, for example, with changing service conditions, small deviations from the thermal model can be minimized or errors in the experimental apparatus can be minimized for maximum confidence in the results. It is recommended that future experimental investigations that have non-systematic bias-error can demonstrate the efficacy of the data subset optimization search.

The PopTea method is able to make thermal diffusivity and thermal conductivity measurements, in part, by the thermal effusivity contrast between the coating and substrate interface. Obscuring this interface reduces the ability of the PopTea method to resolve thermal conductivity. An extension of two-color pyrometry was developed to make surface measurements of both the steady-state and the harmonically fluctuating component of temperature during PopTea measurements. This was an important first-step because it was demonstrated that thermal conductivity can be resolved by the temperature scales measured with pyrometry. However, experimental measurements carried out graphite samples revealed that very small uncertainties in the thermal detector signal propagated to large

uncertainties in the temperature measurements. This was supported by an uncertainty analysis on the measurements and recommendations were provided to reduce this uncertainty propagation. The temperature measurements used a thermal emission model that assumed surface emittance; it is recommended that future work to develop a thermal emission model that that incorporates the translucent nature of the TBCs be used to eliminate the need for any optical coatings.

The work presented in this dissertation has provided considerable insight into reducing uncertainty in thermal property measurements under uncertain physical conditions that occur when the theoretical thermal modeling deviates from the experimental measurements by using adaptive and generic modeling and data reduction techniques. As part of the broader goal of reducing uncertainty in measurements, a first step towards using temperature amplitudes in addition to the thermal emission phase is demonstrated as a way to make thermal conductivity measurements. These advances facilitate and simplify nondestructive thermal property measurements on complex systems by reducing the *a priori* characterization needed for the system. It is recommended that future work towards reducing model characterization should be possible by using a tightly-focused beam to exploit the radial-heating thermal penetration scale to resolve thermal diffusivity; which can be combined with surface temperature measurements to determine thermal conductivity. Measurements made using this approach, and aided by filtering out non-conforming measurements using the data reduction technique developed in this dissertation, should be able to reduce the required knowledge of coating thickness.

Appendix A: Differential PopTea Solution

The general solution of the transformed governing equation eq. (4.25) in the coating, substrate, and subsystem may be applied to the boundary conditions eq. (4.26)-(4.28) to solve for the unknown coefficients. The solution for $\tilde{h}_{coat}(z)$ may be put into the form of

$$\tilde{h}_{coat}(z) = \frac{\exp(-\nu^2/4)}{2(\tilde{\nu}_{coat}^2 - 1/\Lambda^2)}\left(\tilde{s}(z) - \frac{1-\Re_1\exp(-2/\Lambda)}{a_{coat}\gamma_{coat}\tilde{\nu}_{coat}\Lambda^2}\exp(-\tilde{\nu}_{coat}z)\right) + 2C_1\cosh(\tilde{\nu}_{coat}z) \tag{A.1}$$

The remaining integration constant can be evaluated from:

$$C_1 = \det\begin{pmatrix} d_1 & b_{12} & b_{13} & 0 \\ d_2 & b_{22} & b_{23} & 0 \\ 0 & b_{32} & b_{33} & b_{34} \\ 0 & b_{42} & b_{43} & b_{44} \end{pmatrix} \Bigg/ \det\begin{pmatrix} b_{11} & b_{12} & b_{13} & 0 \\ b_{21} & b_{22} & b_{23} & 0 \\ 0 & b_{32} & b_{33} & b_{34} \\ 0 & b_{42} & b_{43} & b_{44} \end{pmatrix} \tag{A.2}$$

with: $b_{11} = 2\cosh\left(\tilde{\nu}_{coat}\right)$, $b_{21} = -2a_{coat}\gamma_{coat}\tilde{\nu}_{coat}\sinh\left(\tilde{\nu}_{coat}\right)$,

$b_{12} = -\exp\left(\tilde{\nu}_{sub}\right)$, $b_{22} = \tilde{\nu}_{sub}\exp\left(\tilde{\nu}_{sub}\right)$, $b_{13} = -\exp\left(-\tilde{\nu}_{sub}\right)$, $b_{23} = -\tilde{\nu}_{sub}\exp\left(-\tilde{\nu}_{sub}\right)$,

$b_{32} = \left(1 + R_{ss}^{*}\tilde{\nu}_{sub}/\left(a_{coat}\gamma_{coat}\right)\right)\exp\left(\tilde{\nu}_{sub}\left(1+Z_{sub}\right)\right)$, $b_{42} = \exp\left(\tilde{\nu}_{sub}\left(1+Z_{sub}\right)\right)$,

$b_{33} = \left(1 - R_{ss}^{*}\tilde{\nu}_{sub}/\left(a_{coat}\gamma_{coat}\right)\right)\exp\left(-\tilde{\nu}_{sub}\left(1+Z_{sub}\right)\right)$, $b_{43} = -\exp\left(-\tilde{\nu}_{sub}\left(1+Z_{sub}\right)\right)$,

$b_{34} = -\exp\left(-\tilde{\nu}_{ss}\left(1+Z_{sub}\right)\right)$, $b_{44} = \left(a_{ss}\gamma_{ss}\tilde{\nu}_{ss}/\tilde{\nu}_{sub}\right)\exp\left(-\tilde{\nu}_{ss}\left(1+Z_{sub}\right)\right)$,

and,

$$d_1 = \frac{\exp\left(-\nu^2/4\right)}{2a_{coat}\gamma_{coat}\Lambda\left(\tilde{\nu}_{coat}^2 - 1/\Lambda^2\right)}\left(\frac{\exp\left(-\tilde{\nu}_{coat}\right)}{\Lambda\tilde{\nu}_{coat}}\left(1-\Re_1\exp\left(-2/\Lambda\right)\right) - \left(1+\Re_1\right)\exp\left(-1/\Lambda\right)\right)$$

,

$$d_2 = -\frac{\exp\left(-\nu^2/4\right)}{2}\exp\left(-1/\Lambda\right)\left(1 - \Re_1 + \Lambda^2\frac{1-\Re_1+\left[\Re_1\exp\left(-1/\Lambda\right) - \exp\left(1/\Lambda\right)\right]\exp\left(-\tilde{\nu}_{coat}\right)}{\left(\tilde{\nu}_{coat}^2 - 1/\Lambda^2\right)}\right)$$

Appendix B: Reflectivity Measurement

This section describes reflectivity measurements of an optical beam with its incident angle normal to a sample. A hemispherical elliptic mirror was used to collect the reflected power of the beam and redirect it to a laser calorimeter. A Synrad Firestar t60 CO_2 laser at 10.6 μm provided the optical heating and a Scientech Large Aperture Calorimeter, model 380402, for the power measurements; an illustration of the experimental apparatus is shown in Figure B.1.

Measuring the reflectivity does not require an absolute laser power measurement, only the relative drop in power measured from the calorimeter with respect to a highly polished surface. From this the reflectivity is expressed as

$$R_s = \frac{Q_s}{Q_{mirror}} \tag{B.1}$$

where Q_s is the reflected power of a specimen and Q_{mirror} is the reflected power of a mirror surface.

The reflecting surface can be mounted in any practical way, but must be normal to the elliptic mirror. The positioning of the laser calorimeter need only to ensure that the reflected beam was expanded over the sensing area of the calorimeter. The laser apparatus was powered on and allowed to stabilize for at least 45 minutes. A plane mirror was used for the Q_{mirror} measurements. A second measurement for the sample reflected power Q_s was recorded. Each individual measurement was taken after an additional 10-minute stabilization.

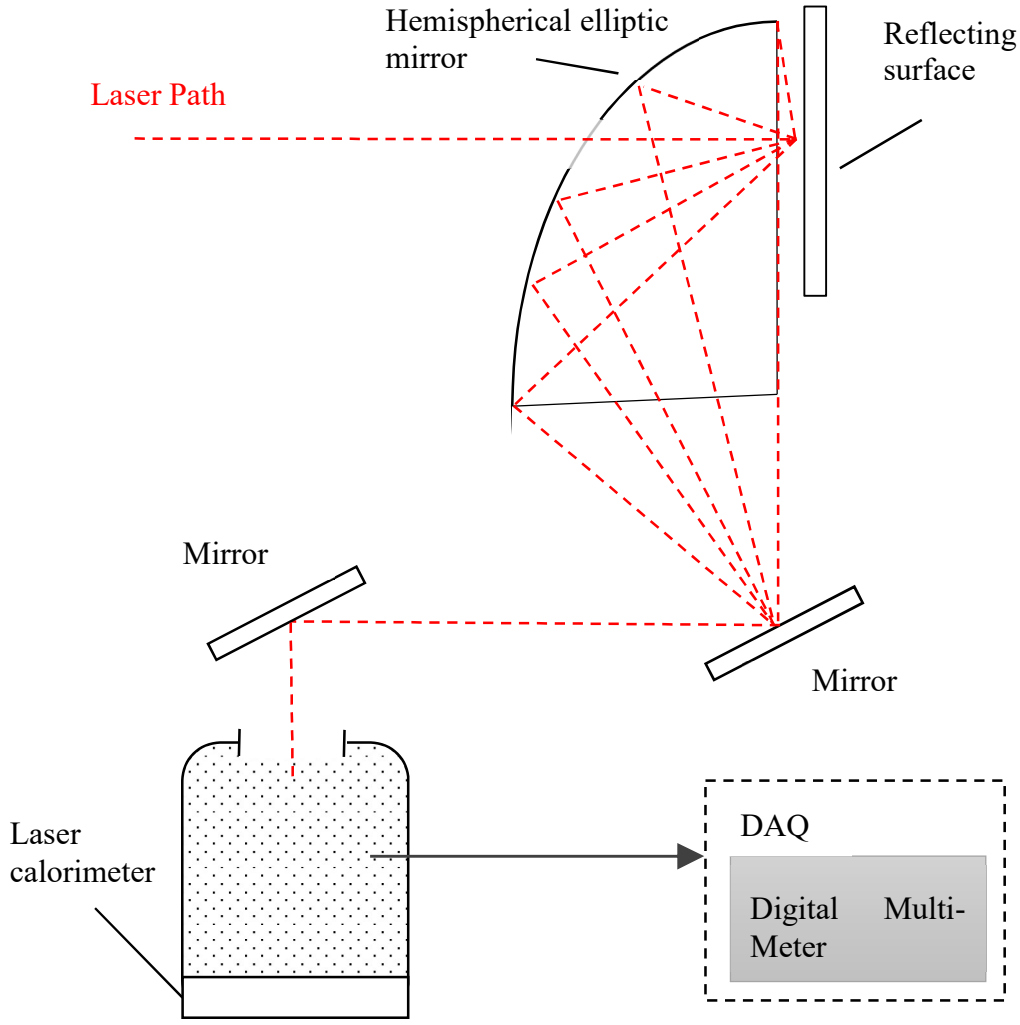

Figure B.1: Reflectivity of sample; experimental apparatus.

Appendix C: Biot Analysis for disk PopTea Model

The heat transfer model developed in Chapter 6 as eq. (6.2) and eq. (6.3) is the first PopTea model (i) of a finite disk and to (ii) include heat losses at the heated surface and peripheral radial boundaries. In the steady state, the heat absorption is balanced by the heat losses at the boundaries, as illustrated in Figure C.1. The heat losses are modeled as a nondimensional Biot number in the boundary conditions. Although these boundaries were developed for convective heat transfer, other forms of heat losses can be manifested through equivalent heat transfer coefficients and Biot numbers.

The predominate forms of heat transfer at the heated surface was the absorption of the laser, heat convection to the laboratory air, and thermal radiation exchange with the

environment. The Nusselt number is used to estimate the natural heat convection coefficient for the surface of disk with a diameter 25.4 mm

$$h_1 = \frac{\mathrm{Nu} \cdot k_{\mathrm{air}}}{D} \tag{C.1}$$

The Churchill and Chu correlation [168] for the average Nusselt number Nu for a vertical isothermal surface is

$$\mathrm{Nu} = 0.68 + 0.67\ \mathrm{Ra}^{1/4}\left[1+\left(\frac{0.492}{\mathrm{Pr}}\right)^{9/16}\right]^{-4/9} \tag{C.2}$$

where, the Rayleigh number (Ra) describes the contribution of heat convection with respect to heat conduction for a buoyancy driven fluid:

$$\mathrm{Ra} = \frac{g\beta}{\nu\alpha}\Delta T \cdot D^3 \tag{C.3}$$

The temperature difference ΔT that is driving the natural convection is based on the steady state temperature of the sample T_o, approximately 200°C, and the bulk air and environmental temperature T_∞ at 20°C. The air is described by a thermal expansion coefficient $\beta = 0.00341\,\mathrm{K}^{-1}$, thermal diffusivity $\alpha_{\mathrm{air}} = 2.203 \cdot 10^{-5}\ \mathrm{m^2 s^{-1}}$, viscous diffusivity $\nu_{\mathrm{air}} = 1.568 \cdot 10^{-5}\ \mathrm{m^2 s^{-1}}$, and thermal conductivity $k_{\mathrm{air}} = 0.0257\ \mathrm{W \cdot m^{-1} K^{-1}}$ in a gravitational field with acceleration $g = 9.81\,\mathrm{m \cdot s^{-2}}$. The Prantl number ($\mathrm{Pr}$) is the ratio of

the viscous to thermal diffusivity, $\mathrm{Pr} = \nu/\alpha$. These values evaluate to a $\mathrm{Ra} = 2.96 \cdot 10^5$, $\mathrm{Pr} = 0.71$, $\mathrm{Nu} = 12.6$ and a surface convection heat transfer coefficient $h_{1,conv} = 12.7\ \mathrm{W \cdot m^2 K^{-1}}$.

The thermal radiative exchange with the environment can be expressed using a radiation heat transfer coefficient [169]:

$$h_{1,rad} = 4\varepsilon\sigma\left(\frac{T_o + T_\infty}{2}\right)^3 \tag{C.4}$$

Evaluating the contribution of thermal radiation with an environmental temperature of 20°C, sample emissivity of unity, and Stephan-Boltzmann constant $\sigma = 5.670367 \cdot 10^{-8}\ \mathrm{W \cdot m^{-2} K^{-4}}$ results in radiative surface heat transfer coefficient of $h_{1,rad} = 12.8\ \mathrm{W \cdot m^2 K^{-1}}$ and this is the same order of magnitude as natural convection. Since both of these heat transfer modes operate in parallel, the equivalent contribution can be evaluated by taking the combined resistance $(R'' = 1/h)$ in parallel

$$\begin{aligned} R''_1 &= R''_{1,conv} \parallel R''_{1,rad} = \frac{R''_{1,conv} \cdot R''_{1,rad}}{R''_{1,conv} + R''_{1,rad}} \\ h_1 &= 25.48\ \mathrm{W \cdot m^2 K^{-1}} \end{aligned} \tag{C.5}$$

The effective heated surface Biot number for a sample with a thermal conductivity $90\ \mathrm{W \cdot m^{-1} K^{-1}}$ and heating radius $6\ \mathrm{mm}$ results in $\mathrm{Bi}_1 = 1.7 \cdot 10^{-3}$ with no dependence on

the thickness of the sample. Since $\mathrm{Bi}_1 \ll 1$, assuming the heated surface Biot is zero is well justified.

The peripheral radial heat losses are also described by an effective heat transfer coefficient and Biot number. An analysis of the heated surface revealed that the heat losses by convection and radiation is negligible, and these contributions are expected to be less significant at the radial boundaries where the exchange area is much smaller. However, the experimental apparatus holds the sample at the peripheral boundary using a steel chuck and the steady state temperature is maintained by heat losses through this fixture. Neglecting the natural convection and thermal radiation, the heat losses through the peripheral is equal to the heat absorbed from the laser, approximately $Q_{absorbed} = 7.38$ W. In order to support this heat loss, the heat transfer coefficient for the disk is

$$h_2 = \frac{Q_{absorbed}}{A \cdot \Delta T} \tag{C.6}$$

where, the peripheral area (A) is calculated for the disk with a thickness of 0.424 mm, and $\Delta T = 180$ K. This results in a peripheral heat transfer coefficient $h_2 = 1212\ \mathrm{W \cdot m^2 K^{-1}}$ and a peripheral $\mathrm{Bi}_2 = 8.1 \cdot 10^{-2}$ that decreases with increasing thickness of the sample. Although larger than the heated surface Biot number, it is still $\mathrm{Bi}_2 \ll 1$, and assuming the peripheral Biot is zero is well justified.

An exploration of the impact of increased Biot number is shown in Figure C.2. These plots show that even in cases of large Biot numbers, $\mathrm{Bi}_2 \gg 1$, the effect of heat losses at the radial boundary is limited to measurements at low frequencies. This is expected to occur because the phase and amplitude respond to the peripheral Biot only in cases that the radial thermal penetration approaches the peripheral boundary; however, the measurements in the two-color PopTea investigation are limited to frequencies greater than or equal 1.0 Hz so even large Biot numbers would not impact the thermal property measurements.

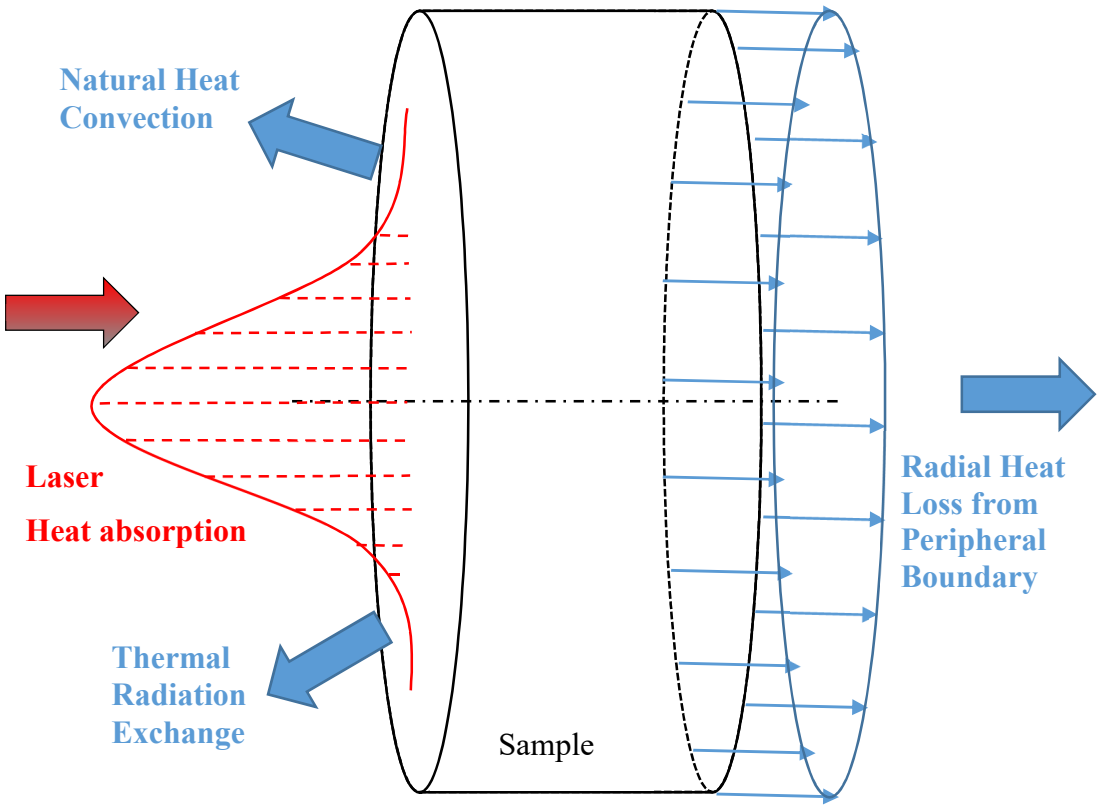

Figure C.1: Steady state heat flow in a disk sample with heat absorption and heat losses at the heated surface and peripheral boundaries.

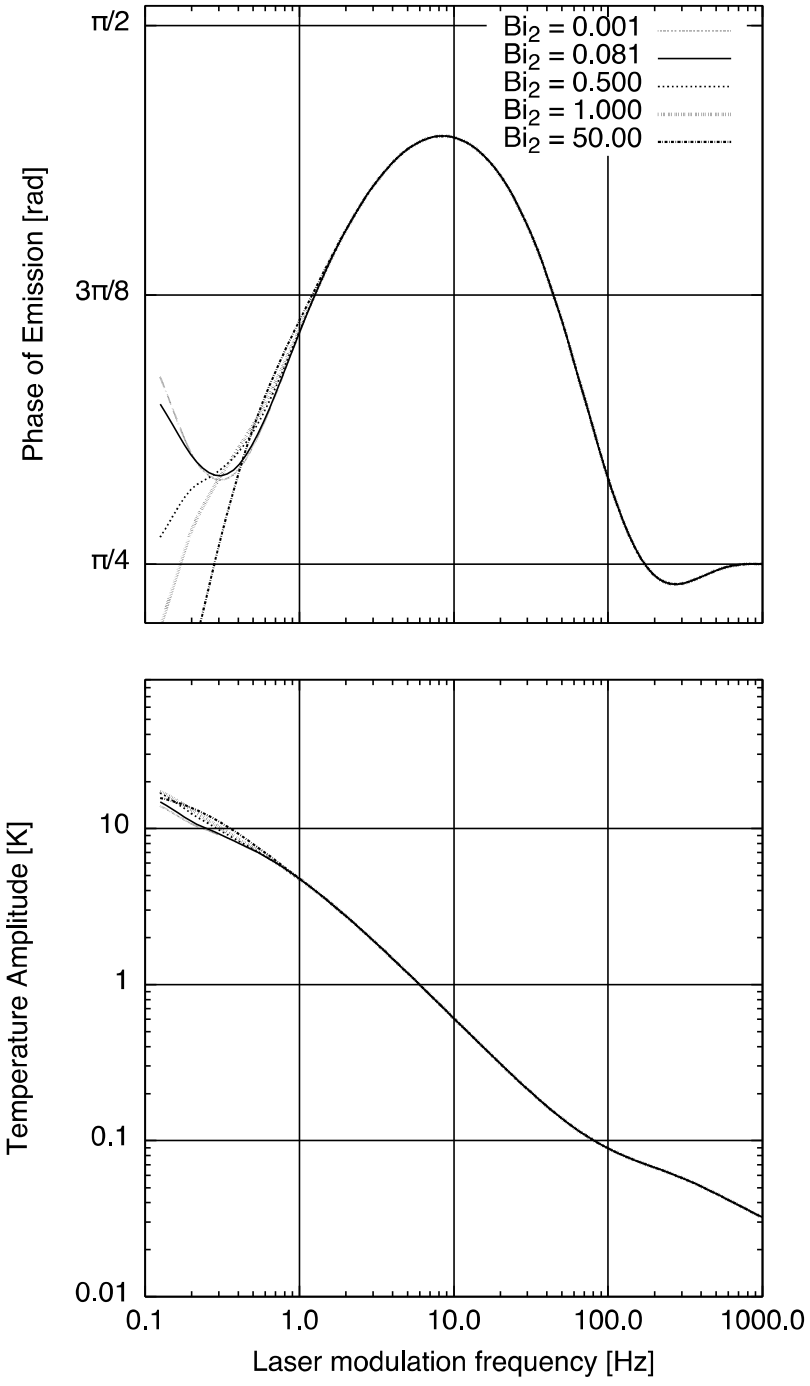

Figure C.2: Parametric peripheral Biot results of phase and temperature amplitude

Appendix D: Uncertainty Analysis for Two-Color Pyrometry

This section develops the uncertainty analysis for two-color pyrometry described in Chapter 6. The uncertainty analysis is carried out using the Propagation of Uncertainty Method [167]. Consider a generic model that evaluates a quantity from parameters

$$g = f\left(X\right) \tag{D.1}$$

For a vector of N input parameters, the uncertainty of the output is evaluated to

$$u_g = \sqrt{\left(\frac{\partial f}{\partial X_1}u_{X_1}\right)^2 + \left(\frac{\partial f}{\partial X_2}u_{X_2}\right)^2 + \ldots + \left(\frac{\partial f}{\partial X_N}u_{X_N}\right)^2} \tag{D.2}$$

Steady state temperature uncertainty

The steady state temperature is evaluated from two-color detector measurements, the thermal emission detector signal at two emissive wavelengths using the steady form of equation (6.32). There are four measurements that are required to make this assessment. The scene radiance I_λ is determined by removing the background radiance I_{bk} from the total detector signal I by using an external shutter.

$$I_\lambda = I - I_{bk} \tag{D.3}$$

The uncertainty for the scene radiance is then

$$u_{I_\lambda} = \sqrt{u_I^2 + u_{I_{bk}}^2} \tag{D.4}$$

Evaluating the scene uncertainty for each of the two color wavelengths becomes

$$\begin{aligned} u_{I_{\lambda_1}} &= \left[\sqrt{u_I^2 + u_{I_{bk}}^2} \right]_{\lambda_1} \\ u_{I_{\lambda_2}} &= \left[\sqrt{u_I^2 + u_{I_{bk}}^2} \right]_{\lambda_2} \end{aligned} \tag{D.5}$$

The detector steady signal ratio, eq. (6.31), evaluates to an uncertainty

$$u_{SR_d} = \sqrt{\left(-\frac{I_{\lambda_2}}{I_{\lambda_1}^2} \right)^2 u_{I_{\lambda_1}}^2 + \left(\frac{1}{I_{\lambda_1}} \right) u_{I_{\lambda_2}}^2} \tag{D.6}$$

The SR used in the two-color analysis needed to be calibrated by the SR gain, eq. (6.36) The uncertainty in the signal ratio is then

$$u_{SR} = \sqrt{g^2 u_{SR_d}^2 + SR_d^2 u_g^2} \tag{D.7}$$

The uncertainty for the two-color steady state temperature using the steady state form of eq. (6.32) is

$$u_T = \sqrt{\left(-\frac{C_2/\lambda_1 - C_2/\lambda_2}{SR \cdot \left(\ln(SR) - 5\ln\left(\lambda_1/\lambda_2\right)\right)^2} \right)^2 u_{SR}^2} \tag{D.8}$$

Amplitude temperature uncertainty

The harmonic detector signal ratio can be formulated as a summation of the steady state scene radiance and the harmonic component, when $\cos(\omega t) = 1$ (highest uncertainty)

$$SR_d = \frac{\overline{I}_{\lambda_2} + \left|\tilde{I}_{\lambda_2}\right|}{\overline{I}_{\lambda_1} + \left|\tilde{I}_{\lambda_1}\right|} \tag{D.9}$$

The uncertainty in the detector signal ratio is

$$u_{SR_d} = \sqrt{\left(-\frac{\bar{I}_{\lambda_2}+\tilde{I}_{\lambda_2}}{\left(\bar{I}_{\lambda_1}+\tilde{I}_{\lambda_1}\right)^2}u_{\bar{I}_{\lambda_1}}\right)^2+\left(\frac{1}{\bar{I}_{\lambda_1}+\tilde{I}_{\lambda_1}}u_{\bar{I}_{\lambda_2}}\right)^2+\left(-\frac{\bar{I}_{\lambda_2}+\tilde{I}_{\lambda_2}}{\left(\bar{I}_{\lambda_1}+\tilde{I}_{\lambda_1}\right)^2}u_{\tilde{I}_{\lambda_1}}\right)^2+\left(\frac{1}{\bar{I}_{\lambda_1}+\tilde{I}_{\lambda_1}}u_{\tilde{I}_{\lambda_2}}\right)^2} \tag{D.10}$$

And the uncertainty in the calibrated signal ratio, after SR gain, has already been presented as eq. (D.7). An explicit relationship for the temperature amplitudes can be formulated in terms of the steady state temperature using eq. (6.32) and $\cos(\omega t)=1$.

$$\left|\tilde{T}\right| = \bar{T}-\bar{T}^2\left(\frac{\ln(SR)-5\ln\left(\lambda_1/\lambda_2\right)}{C_2/\lambda_1-C_2/\lambda_2}\right) \tag{D.11}$$

Propagating the uncertainty in the signal ratio and steady state temperature results in

$$u_{|\tilde{T}|} = \sqrt{\left(\left(1-2\bar{T}\left(\frac{\ln(SR)-5\ln\left(\lambda_1/\lambda_2\right)}{C_2/\lambda_1-C_2/\lambda_2}\right)\right)u_{\bar{T}}\right)^2+\left(\left(-\frac{\bar{T}^2}{SR\cdot\left(C_2/\lambda_1-C_2/\lambda_2\right)}\right)u_{SR}\right)^2} \tag{D.12}$$

References

[1] W. W. Bathie, “Fundamentals of gas turbines,” Jan. 1984.

[2] C. Soares, *Gas Turbines: A Handbook of Air, Land, and Sea Applications*. Butterworth-Heinemann, 2007.

[3] J. H. Perepezko, “The Hotter the Engine, the Better,” *Science*, vol. 326, no. 5956, pp. 1068–1069, Nov. 2009.

[4] J. H. Horlock, D. T. Watson, and T. V. Jones, “Limitations on Gas Turbine Performance Imposed by Large Turbine Cooling Flows,” *J. Eng. Gas Turbines Power*, vol. 123, no. 3, pp. 487–494, Feb. 2001.

[5] A. G. Evans, D. R. Mumm, J. W. Hutchinson, G. H. Meier, and F. S. Pettit, “Mechanisms controlling the durability of thermal barrier coatings,” *Progress in Materials Science*, vol. 46, no. 5, pp. 505–553, 2001.

[6] D. R. Clarke and C. G. Levi, “Materials design for the next generation thermal barrier coatings,” *Annual Review of Materials Research*, vol. 33, pp. 383–417, 2003.

[7] C. G. Levi, “Emerging materials and processes for thermal barrier systems,” *Current Opinion in Solid State and Materials Science*, vol. 8, no. 1, pp. 77–91, Jan. 2004.

[8] U. Schulz, C. Leyens, K. Fritscher, M. Peters, B. Saruhan-Brings, O. Lavigne, J.-M. Dorvaux, M. Poulain, R. Mévrel, and M. Caliez, “Some recent trends in research and technology of advanced thermal barrier coatings,” *Aerospace Science and Technology*, vol. 7, no. 1, pp. 73–80, Jan. 2003.

[9] J. R. Fincke, W. D. Swank, R. L. Bewley, D. C. Haggard, M. Gevelber, and D. Wroblewski, “Diagnostics and control in the thermal spray process,” *Surface and Coatings Technology*, vol. 146–147, pp. 537–543, Sep. 2001.

[10] J. A. Haynes, M. K. Ferber, and W. D. Porter, “Thermal cycling behavior of plasma-sprayed thermal barrier coatings with various MCrAlX bond coats,” *J Therm Spray Tech*, vol. 9, no. 1, pp. 38–48, Mar. 2000.

[11] K. Kokini, J. DeJonge, S. Rangaraj, and B. Beardsley, “Thermal shock of functionally graded thermal barrier coatings with similar thermal resistance,” *Surface and Coatings Technology*, vol. 154, no. 2–3, pp. 223–231, May 2002.

[12] L. Li, N. Hitchman, and J. Knapp, “Failure of Thermal Barrier Coatings Subjected to CMAS Attack,” *J Therm Spray Tech*, vol. 19, no. 1–2, pp. 148–155, Jul. 2009.

[13] I. G. Wright and T. B. Gibbons, “Recent developments in gas turbine materials and technology and their implications for syngas firing,” *International Journal of Hydrogen Energy*, vol. 32, no. 16, pp. 3610–3621, Nov. 2007.

[14] J. M. Wright, D. C. Faucett, M. Ayre, and S. R. Choi, “Foreign Object Damage (FOD) of Ceramic Thermal Barrier Coatings (TBCs) in Gas Turbine Airfoils,” p. V004T02A006, Jun. 2013.

[15] H. Wang and R. B. Dinwiddie, “Reliability of laser flash thermal diffusivity measurements of the thermal barrier coatings,” *J Therm Spray Tech*, vol. 9, no. 2, pp. 210–214, Jun. 2000.

[16] W. Chi, S. Sampath, and H. Wang, “Comparison of the Thermal Transport Property Measurements of Thermally Sprayed Coatings by the Laser and Xenon Flash Techniques,” *J Therm Spray Tech*, vol. 16, no. 3, pp. 444–448, Jul. 2007.

[17] J. G. Sun, “Pulsed Thermal Imaging Measurement of Thermal Properties for Thermal Barrier Coatings Based on a Multilayer Heat Transfer Model,” *J. Heat Transfer*, vol. 136, no. 8, pp. 081601–081601, May 2014.

[18] P. G. Bison, F. Cernuschi, E. Grinzato, S. Marinetti, and D. Robba, “Ageing evaluation of thermal barrier coatings by thermal diffusivity,” *Infrared Physics & Technology*, vol. 49, no. 3, pp. 286–291, Jan. 2007.

[19] P. Bison, F. Cernuschi, and E. Grinzato, “In-depth and in-plane thermal diffusivity measurements of thermal barrier coatings by IR camera: Evaluation of ageing,” *International Journal of Thermophysics*, vol. 29, no. 6, pp. 2149–2161, 2008.

[20] T. Bennett, T. Kakuda, and A. Kulkarni, “Front surface thermal property measurements of air plasma spray coatings,” *Journal of Applied Physics*, vol. 105, no. 8, 2009.

[21] T. D. Bennett and F. Yu, “A nondestructive technique for determining thermal properties of thermal barrier coatings,” *Journal of Applied Physics*, vol. 97, no. 1, 2005.

[22] S. Bose, *High Temperature Coatings*. Butterworth-Heinemann, 2011.

[23] M. P. Boyce, *Gas Turbine Engineering Handbook*. Elsevier, 2011.

[24] N. P. Padture, M. Gell, and E. H. Jordan, "Thermal Barrier Coatings for Gas-Turbine Engine Applications," *Science*, vol. 296, no. 5566, pp. 280–284, Apr. 2002.

[25] D. R. Clarke, M. Oechsner, and N. P. Padture, "Thermal-barrier coatings for more efficient gas-turbine engines," *MRS Bulletin*, vol. 37, no. 10, pp. 891–898, 2012.

[26] K. W. Schlichting, N. P. Padture, and P. G. Klemens, "Thermal conductivity of dense and porous yttria-stabilized zirconia," *Journal of Materials Science*, vol. 36, no. 12, pp. 3003–3010, 2001.

[27] M. J. Donachie and S. J. Donachie, *Superalloys: A Technical Guide, 2nd Edition*. ASM International, 2002.

[28] Z. Lu, S. W. Myoung, E. H. Kim, J. H. Lee, and Y. G. Jung, "Microstructure Evolution and Thermal Durability with Coating Thickness in APS Thermal Barrier Coatings," *Materials Today: Proceedings*, vol. 1, no. 1, pp. 35–43, 2014.

[29] R. C. Progelhof, J. L. Throne, and R. R. Ruetsch, "Methods for predicting the thermal conductivity of composite systems: A review," *Polym Eng Sci*, vol. 16, no. 9, pp. 615–625, Sep. 1976.

[30] J. C. Maxwell and J. J. Thompson, *A Treatise on Electricity and Magnetism*. Clarendon, 1904.

[31] A. Eucken, "Allgemeine Gesetzmäßigkeiten für das Wärmeleitvermögen verschiedener Stoffarten und Aggregatzustände," *Forsch Ing-Wes*, vol. 11, no. 1, pp. 6–20, Jan. 1940.

[32] R. Landauer, “The Electrical Resistance of Binary Metallic Mixtures,” *Journal of Applied Physics*, vol. 23, no. 7, pp. 779–784, Jul. 1952.

[33] C. J. F. Böttcher, O. C. van Belle, P. Bordewijk, and A. Rip, *Theory of electric polarization*. Elsevier Scientific Pub. Co., 1978.

[34] Q. Guo, *Thermosets: Structure, Properties and Applications*. Elsevier, 2012.

[35] G. K. Batchelor, “Transport Properties of Two-Phase Materials with Random Structure,” *Annual Review of Fluid Mechanics*, vol. 6, no. 1, pp. 227–255, 1974.

[36] M. Ferrari, “Composite homogenization via the equivalent poly-inclusion approach,” *Composites Engineering*, vol. 4, no. 1, Dec. 1994.

[37] J. K. Carson, “Review of effective thermal conductivity models for foods,” *International Journal of Refrigeration*, vol. 29, no. 6, pp. 958–967, Sep. 2006.

[38] J. K. C. Jianfeng Wang, “A New Approach to Modelling the Effective Thermal Conductivity of Heterogeneous Materials,” *International Journal of Heat and Mass Transfer*, vol. 49, no. 17–18, pp. 3075–3083, 2006.

[39] Ö. Altun, “Numerical Modeling of Thermal Conductivity Of Air-Plasma-Sprayed Zirconia With Different Porosity Levels,” *0 Isı bilimi ve tekniği dergisi = Journal of Thermal Sciences and Technology*, vol. 31, no. 1, pp. 77–84, 2011.

[40] A. Kulkarni, Z. Wang, T. Nakamura, S. Sampath, A. Goland, H. Herman, J. Allen, J. Ilavsky, G. Long, J. Frahm, and R. W. Steinbrech, “Comprehensive microstructural characterization and predictive property modeling of plasma-sprayed zirconia coatings,” *Acta Materialia*, vol. 51, no. 9, pp. 2457–2475, May 2003.

[41] Z. Wang, A. Kulkarni, S. Deshpande, T. Nakamura, and H. Herman, “Effects of pores and interfaces on effective properties of plasma sprayed zirconia coatings,” *Acta Materialia*, vol. 51, no. 18, pp. 5319–5334, Oct. 2003.

[42] A. D. Jadhav, N. P. Padture, E. H. Jordan, M. Gell, P. Miranzo, and E. R. Fuller Jr., “Low-thermal-conductivity plasma-sprayed thermal barrier coatings with engineered microstructures,” *Acta Materialia*, vol. 54, no. 12, pp. 3343–3349, Jul. 2006.

[43] P. Michlik and C. Berndt, “Image-based extended finite element modeling of thermal barrier coatings,” *Surface and Coatings Technology*, vol. 201, no. 6, pp. 2369–2380, 2006.

[44] J. Banks, *Handbook of Simulation: Principles, Methodology, Advances, Applications, and Practice*. John Wiley & Sons, 1998.

[45] J. P. C. Kleijnen, “Verification and validation of simulation models,” *European Journal of Operational Research*, vol. 82, no. 1, pp. 145–162, Apr. 1995.

[46] W. L. Oberkampf and C. J. Roy, *Verification and Validation in Scientific Computing*. Cambridge University Press, 2010.

[47] M. N. Ozisik and H. R. B. Orlande, *Inverse Heat Transfer: Fundamentals and Applications*. Taylor & Francis, 2000.

[48] R. Poensgen, “A technical process for investigating the heat conducting capacity of plate-shaped material,” *Zeitschrift des Vereines deutscher Ingenieure*, 1912.

[49] D. Salmon, “Thermal conductivity of insulations using guarded hot plates, including recent developments and sources of reference materials,” *Measurement Science and Technology*, vol. 12, no. 12, pp. R89–R98, Dec. 2001.

[50] W. J. Parker, R. J. Jenkins, C. P. Butler, and G. L. Abbott, “Flash Method of Determining Thermal Diffusivity, Heat Capacity, and Thermal Conductivity,” *Journal of Applied Physics*, vol. 32, no. 9, pp. 1679–1684, Sep. 1961.

[51] F. I. Chu, R. E. Taylor, and A. B. Donaldson, “Thermal diffusivity measurements at high temperatures by the radial flash method,” *Journal of Applied Physics*, vol. 51, no. 1, pp. 336–341, 1980.

[52] D02 Committee, “Test Method for Thermal Diffusivity of Carbon and Graphite by Thermal Pulse Method,” ASTM International, 2010.

[53] F. Hemberger, S. Weis, G. Reichenauer, and H.-P. Ebert, “Thermal transport properties of functionally graded carbon aerogels,” *International Journal of Thermophysics*, vol. 30, no. 4, pp. 1357–1371, 2009.

[54] M. Ruoho, K. Valset, T. Finstad, and I. Tittonen, “Measurement of thin film thermal conductivity using the laser flash method,” *Nanotechnology*, vol. 26, no. 19, 2015.

[55] A. Cai, L. Yang, J. Chen, T. Xi, S. Xin, and W. Wu, “Thermal Conductivity of Anodic Alumina Film at (220 to 480) K by Laser Flash Technique,” *J. Chem. Eng. Data*, vol. 55, no. 11, pp. 4840–4843, Nov. 2010.

[56] D. P. H. Hasselman, R. Syed, and T.-Y. Tien, “Thermal diffusivity and conductivity of transformation-toughened solid solutions of alumina and chromia.,” *Journal of Materials Science*, vol. 20, no. 7, pp. 2549–2556, 1985.

[57] L. A. Girifalco, *Statistical Mechanics of Solids*. Oxford University Press, USA, 2003.

[58] K. A. Borup, J. de Boor, H. Wang, F. Drymiotis, F. Gascoin, X. Shi, L. Chen, M. I. Fedorov, E. Müller, B. B. Iversen, and G. J. Snyder, “Measuring thermoelectric transport properties of materials,” *Energy Environ. Sci.*, vol. 8, no. 2, pp. 423–435, Feb. 2015.

[59] J. C. Gibbings, *Dimensional Analysis*. Springer Science & Business Media, 2011.

[60] P. K. Kuo, M. J. Lin, C. B. Reyes, L. D. Favro, R. L. Thomas, D. S. Kim, Shu-yi Zhang, L. J. Inglehart, D. Fournier, A. C. Boccara, and N. Yacoubi, "Mirage-effect measurement of thermal diffusivity. Part I: Experiment," *Canadian journal of physics*, vol. 64, no. 9, pp. 1165–1168, 1985.

[61] R. A. Morgan, K. I. Kang, C. C. Hsu, C. L. Koliopoulos, and N. Peyghambarian, "Measurement of the thermal diffusivity of nonlinear anisotropic crystals using optical interferometry," *Applied Optics*, vol. 26, no. 24, p. 5266, Dec. 1987.

[62] A. Rosencwaig, J. Opsal, W. L. Smith, and D. L. Willenborg, "Detection of thermal waves through optical reflectance," *Applied Physics Letters*, vol. 46, no. 11, pp. 1013–1015, Jun. 1985.

[63] M. A. Olmstead, N. M. Amer, S. Kohn, D. Fournier, and A. C. Boccara, "Photothermal Displacement spectroscopy: an optical probe for solids and surfaces.," *Applied physics. A, Solids and surfaces*, vol. A32, no. 3, pp. 141–154, 1983.

[64] H. S. Carslaw and J. C. Jaeger, "Conduction of heat in solids," *Oxford: Clarendon Press, 1959, 2nd ed.*, vol. -1, 1959.

[65] R. L. Rudkin, R. J. Jenkins, and W. J. Parker, "Thermal Diffusivity Measurements on Metals at High Temperatures," *Review of Scientific Instruments*, vol. 33, no. 1, pp. 21–24, Jan. 1962.

[66] R. D. Cowan, "Pulse Method of Measuring Thermal Diffusivity at High Temperatures," *Journal of Applied Physics*, vol. 34, no. 4, pp. 926–927, Apr. 1963.

[67] J. A. Cape and G. W. Lehman, "Temperature and Finite Pulse Time Effects in the Flash Method for Measuring Thermal Diffusivity," *Journal of Applied Physics*, vol. 34, no. 7, pp. 1909–1913, Jul. 1963.

[68] R. E. Taylor and J. A. Cape, “Finite pulse time effects in the flash diffusivity technique,” *Applied Physics Letters*, vol. 5, no. 10, pp. 212–213, Nov. 1964.

[69] K. B. Larson and K. Koyama, “Correction for Finite-Pulse-Time Effects in Very Thin Samples using the Flash Method of Measuring Thermal Diffusivity,” *Journal of Applied Physics*, vol. 38, no. 2, pp. 465–474, Feb. 1967.

[70] R. C. Heckman, “Finite pulse-time and heat-loss effects in pulse thermal diffusivity measurements,” *Journal of Applied Physics*, vol. 44, no. 4, pp. 1455–1460, Apr. 1973.

[71] T. Azumi and Y. Takahashi, “Novel finite pulse-width correction in flash thermal diffusivity measurement,” *Review of Scientific Instruments*, vol. 52, no. 9, pp. 1411–1413, Sep. 1981.

[72] M. M. Gentleman, V. Lughi, J. A. Nychka, and D. R. Clarke, “Noncontact Methods for Measuring Thermal Barrier Coating Temperatures,” *International Journal of Applied Ceramic Technology*, vol. 3, no. 2, pp. 105–112, Apr. 2006.

[73] W. A. Ellingson, R. Lipanovich, S. Hopson, and R. Visher, “Nondestructive evaluation methods for high temperature ceramic coatings,” in *Advanced Ceramic Coatings and Interfaces - 30th International Conference on Advanced Ceramics and Composites, January 22, 2006 - January 27, 2006*, 2006, vol. 27, pp. 207–214.

[74] D. R. Green, “Thermal Surface Impedance for Plane Heat Waves in Layered Materials,” *Journal of Applied Physics*, vol. 37, no. 8, pp. 3095–3099, Jul. 1966.

[75] K. B. Larson and K. Koyama, “Measurement by the Flash Method of Thermal Diffusivity, Heart Capacity, and Thermal Conductivity in Two-Layer Composite Samples,” *Journal of Applied Physics*, vol. 39, no. 9, pp. 4408–4416, Aug. 1968.

[76] C. S. Ang, H. S. Tan, and S. L. Chan, “Three-layer thermal-diffusivity problem applied to measurements on mercury,” *Journal of Applied Physics*, vol. 44, no. 2, pp. 687–691, Feb. 1973.

[77] J.-Y. Hsu, N.-C. Wu, and S.-C. Yu, “Characterization of Material for Low-Temperature Sintered Multilayer Ceramic Substrates,” *Journal of the American Ceramic Society*, vol. 72, no. 10, pp. 1861–1867, 1989.

[78] I. Hatta, “Thermal diffusivity measurements of thin films and multilayered composites,” *International Journal of Thermophysics*, vol. 11, no. 2, pp. 293–303, 1990.

[79] J. Sulistyo, T. Hata, M. Fujisawa, K. Hashimoto, Y. Imamura, and T. Kawasaki, “Anisotropic thermal conductivity of three-layer laminated carbon-graphite composites from carbonized wood,” *Journal of Materials Science*, vol. 44, no. 3, pp. 734–744, 2009.

[80] M. Niezgoda, D. Rochais, F. Enguehard, P. Echegut, and B. Rousseau, “Modeling of time-resolved coupled radiative and conductive heat transfer in multilayer semitransparent materials up to very high temperatures,” *Applied Physics Letters*, vol. 99, no. 22, p. 224101, 2011.

[81] H.-P. Tan and H.-L. Yi, “Temperature response in participating media with anisotropic scattering caused by pulsed lasers,” *Journal of Quantitative Spectroscopy and Radiative Transfer*, vol. 87, no. 2, pp. 175–192, Aug. 2004.

[82] A. P. F. Albers, T. A. G. Restivo, L. Pagano, and J. B. Baldo, “Effect of testing conditions on the laser flash thermal diffusivity measurements of ceramics,” *Thermochimica Acta*, vol. 370, no. 1–2, pp. 111–118, Apr. 2001.

[83] F. Cernuschi, L. Lorenzoni, P. Bianchi, and A. Figari, “The effects of sample surface treatments on laser flash thermal diffusivity measurements,” *Infrared Physics & Technology*, vol. 43, no. 3–5, pp. 133–138, Jun. 2002.

[84] S.-K. Kim and Y.-J. Kim, “Determination of apparent thickness of graphite coating in flash method,” *Thermochimica Acta*, vol. 468, no. 1–2, pp. 6–9, Feb. 2008.

[85] D. P. Almond and P. Patel, *Photothermal Science and Techniques*. Springer, 1996.

[86] J. Stuckey, J. G. Sun, and W. A. Ellingson, “Rapid Infrared Characterization of Thermal Diffusivity in Continuous Fiber Ceramic Composite Components,” in *Nondestructive Characterization of Materials VIII*, R. E. G. Jr, Ed. Springer US, 1998, pp. 805–810.

[87] J. G. Sun, C. Deemer, W. A. Ellingson, T. E. Easler, A. Szweda, and P. A. Craig, “Thermal Imaging Measurement and Correlation of Thermal Diffusivity in Continuous Fiber Ceramic Composites,” Argonne National Lab., IL (United States), ANL/ET/CP--93341; CONF-9710119--, Sep. 1997.

[88] W. A. Ellingson, E. R. Koehl, J. G. Sun, C. Deemer, H. Lee, and T. Spohnholtz, “Development of nondestructive evaluation methods for hot gas filters,” *Materials at High Temperatures*, vol. 16, no. 4, pp. 213–218, 1999.

[89] W. A. Ellingson, C. Deemer, S. Erdman, and A. Parikh, “Nondestructive characterization of environmental barrier coatings applied to monolithic ceramics,” in *Proceedings of the ASME TURBO EXPO 2002: Ceramics, Industrial and Cogeneration Structures and Dynamics, June 3, 2002 - June 6, 2002*, 2002, vol. 4 A, pp. 179–185.

[90] J. G. Sun, “Measurement of thermal barrier coating conductivity by thermal imaging method,” in *Advanced Ceramic Coatings and Interfaces IV - 33rd International*

Conference on Advanced Ceramics and Composites, January 18, 2009 - January 23, 2009, 2010, vol. 30, pp. 97–103.

[91] F. Cernuschi, P. Bison, and J. G. Sun, "Thermal diffusivity of TBC: Results of a small round robin test and considerations about the effect of the surface preparation and the measuring approach," *Surface and Coatings Technology*, vol. 258, pp. 284–292, Nov. 2014.

[92] F. Cernuschi, P. G. Bison, A. Figari, S. Marinetti, and E. Grinzato, "Thermal Diffusivity Measurements by Photothermal and Thermographic Techniques," *International Journal of Thermophysics*, vol. 25, no. 2, pp. 439–457, 2004.

[93] S. Kozerski, L. Łatka, L. Pawlowski, F. Cernuschi, F. Petit, C. Pierlot, H. Podlesak, and J. P. Laval, "Preliminary study on suspension plasma sprayed ZrO2 + 8 wt.% Y2O3 coatings," *Journal of the European Ceramic Society*, vol. 31, no. 12, pp. 2089–2098, Oct. 2011.

[94] P. Bison, F. Clarelli, and A. Vannozzi, "Pulsed Thermography for Depth Profiling in Marble Sulfation," *International Journal of Thermophysics*, vol. 36, no. 5–6, pp. 1123–1130, Jun. 2015.

[95] F. Cernuschi, "Can TBC porosity be estimated by non-destructive infrared techniques? A theoretical and experimental analysis," *Surface and Coatings Technology*, vol. 272, pp. 387–394, Jun. 2015.

[96] N. W. Pech-May, A. Mendioroz, and A. Salazar, "Simultaneous measurement of the in-plane and in-depth thermal diffusivity of solids using pulsed infrared thermography with focused illumination," *NDT & E International*, vol. 77, pp. 28–34, Jan. 2016.

[97] T. D. Bennett, “Determining anisotropic film thermal properties through harmonic surface heating with a Gaussian laser beam: A theoretical consideration,” *Journal of Heat Transfer*, vol. 126, no. 3, pp. 305–311, 2004.

[98] F. Yu and T. D. Bennett, “Phase of thermal emission spectroscopy for properties measurements of delaminating thermal barrier coatings,” *Journal of Applied Physics*, vol. 98, no. 10, 2005.

[99] T. D. Bennett and F. Yu, “Linear radiation model for phase of thermal emission spectroscopy,” *Journal of Applied Physics*, vol. 98, no. 9, p. 093516, Nov. 2005.

[100] T. R. Kakuda, C. G. Levi, and T. D. Bennett, “The thermal behavior of CMAS-infiltrated thermal barrier coatings,” *Surface and Coatings Technology*, vol. 272, pp. 350–356, 2015.

[101] T. R. Kakuda, A. M. Limarga, T. D. Bennett, and D. R. Clarke, “Evolution of thermal properties of EB-PVD 7YSZ thermal barrier coatings with thermal cycling,” *Acta Materialia*, vol. 57, no. 8, pp. 2583–2591, 2009.

[102] T. Kakuda, A. Limarga, A. Vaidya, A. Kulkarni, and T. D. Bennett, “Non-destructive thermal property measurements of an APS TBC on an intact turbine blade,” *Surface and Coatings Technology*, vol. 205, no. 2, pp. 446–451, 2010.

[103] H. Zhao, F. Yu, T. D. Bennett, and H. N. G. Wadley, “Morphology and thermal conductivity of yttria-stabilized zirconia coatings,” *Acta Materialia*, vol. 54, no. 19, pp. 5195–5207, 2006.

[104] O. Cleynan, *Gas_turbine_applications_(numbered)*. retrieved from https://commons.wikimedia.org/wiki/File:Gas_turbine_applications_(numbered).svg. Used under Creative Commons Attribution-NonCommercial-ShareAlike 2.0 Generic license (http://creativecommons.org/licenses/by-nc-sa/2.0/).

[105] J. Dahl, *Jet Engine*. retrieved from https://en.wikipedia.org/wiki/File:Jet_engine.svg. Used under Creative Commons Attribution-NonCommercial-ShareAlike 2.0 Generic license (http://creativecommons.org/licenses/by-nc-sa/2.0/).

[106] C. U. Hardwicke and Y.-C. Lau, "Advances in thermal spray coatings for gas turbines and energy generation: A review," *Journal of Thermal Spray Technology*, vol. 22, no. 5, pp. 564–576, 2013.

[107] R. E. Taylor, "Thermal conductivity determinations of thermal barrier coatings," *Materials Science and Engineering: A*, vol. 245, no. 2, pp. 160–167, May 1998.

[108] F. Yu, "The nondestructive evaluation of thermal barrier coatings: Measurements of thermal properties and associated defects," *Ph.D. Thesis*, Nov. 2005.

[109] T. Kakuda, "Phase of Photothermal Emission Analysis as a Diagnostic Tool for Thermal Barrier Coatings on Serviceable Engine Components," D.Eng., University of California, Santa Barbara, United States -- California, 2010.

[110] N. A. of Engineering, *Lasers:: Invention to Application*. National Academies Press, 1987.

[111] E. R. Menzel, *Laser Spectroscopy: Techniques and Applications*. CRC Press, 1995.

[112] M. A. de Arajo, R. Silva, E. de Lima, D. P. Pereira, and P. C. de Oliveira, "Measurement of Gaussian laser beam radius using the knife-edge technique: improvement on data analysis," *Appl. Opt.*, vol. 48, no. 2, pp. 393–396, Jan. 2009.

[113] Goutzoulis, *Design and Fabrication of Acousto-Optic Devices*. CRC Press, 1994.

[114] U. Efron, *Spatial Light Modulator Technology: Materials, Devices, and Applications*. CRC Press, 1994.

[115] J. C. Whitaker, *The Electronics Handbook, Second Edition*. CRC Press, 2005.

[116] K. Iizuka, *Engineering Optics*. Springer Science & Business Media, 2009.

[117] R. Hunsperger, *Integrated Optics: Theory and Technology*. Springer Science & Business Media, 2013.

[118] W. Bai and B. S. Wong, "Thermal wave scattering from subsurface defects in plates with finite thickness under convective environments," *Measurement Science and Technology*, vol. 13, no. 5, pp. 700 – 705, 2002.

[119] X. Chen, G. Newaz, and X. Han, "Damage assessment in thermal barrier coatings using thermal wave imaging technique," in *American Society of Mechanical Engineers, Aerospace Division (Publication) AD*, New York, NY, United states, 2001, vol. 66, pp. 239 – 246.

[120] C. T. Sims, N. S. Stoloff, and W. C. Hagel, *Superalloys II*. Wiley, 1987.

[121] R. C. Reed, *The Superalloys: Fundamentals and Applications*. Cambridge University Press, 2008.

[122] B. Tryon, F. Cao, K. S. Murphy, C. G. Levi, and T. M. Pollock, "Ruthenium-containing bond coats for thermal barrier coating systems," *JOM*, vol. 58, no. 1, pp. 53–59, Jan. 2006.

[123] J. G. Sun, "Thermal imaging characterization of thermal barrier coatings," in *Ceramic Engineering and Science Proceedings*, Daytona Beach, FL, United states, 2008, vol. 28, pp. 53 – 60.

[124] H. Cohen, G. F. C. Rogers, and H. I. H. Saravanamuttoo, *Gas turbine theory*, 2d ed. New York: Wiley, 1973.

[125] P. J. Haines, *Principles of Thermal Analysis and Calorimetry*. Royal Society of Chemistry, 2002.

[126] P. Gill, T. T. Moghadam, and B. Ranjbar, "Differential Scanning Calorimetry Techniques: Applications in Biology and Nanoscience," *J Biomol Tech*, vol. 21, no. 4, pp. 167–193, Dec. 2010.

[127] R. Venkatasubramanian, "Lattice thermal conductivity reduction and phonon localizationlike behavior in superlattice structures," *Phys. Rev. B*, vol. 61, no. 4, pp. 3091–3097, Jan. 2000.

[128] T. Borca-Tasciuc, W. Liu, J. Liu, T. Zeng, D. W. Song, C. D. Moore, G. Chen, K. L. Wang, M. S. Goorsky, T. Radetic, R. Gronsky, T. Koga, and M. S. Dresselhaus, "Thermal conductivity of symmetrically strained Si/Ge superlattices," *Superlattices and Microstructures*, vol. 28, no. 3, pp. 199–206, Sep. 2000.

[129] T. Borca-Tasciuc, A. R. Kumar, and G. Chen, "Data reduction in 3ω method for thin-film thermal conductivity determination," *Review of Scientific Instruments*, vol. 72, no. 4, pp. 2139–2147, Apr. 2001.

[130] A. Jacquot, B. Lenoir, A. Dauscher, M. Stölzer, and J. Meusel, "Numerical simulation of the 3ω method for measuring the thermal conductivity," *Journal of Applied Physics*, vol. 91, no. 7, pp. 4733–4738, Apr. 2002.

[131] S. Kudo, H. Hagino, S. Tanaka, K. Miyazaki, and M. Takashiri, "Determining the Thermal Conductivity of Nanocrystalline Bismuth Telluride Thin Films Using the Differential 3 Method While Accounting for Thermal Contact Resistance," *Journal of Electronic Materials*, vol. 44, no. 6, pp. 2021–2025, 2015.

[132] J. V. Beck, *Parameter estimation in engineering and science*. New York: Wiley, 1977.

[133] G. Chavent, “Nonlinear Inverse Problems: Examples and Difficulties,” in *Nonlinear Least Squares for Inverse Problems*, Springer Netherlands, 2010, pp. 5–28.

[134] A. van den Bos, *Parameter Estimation for Scientists and Engineers*. John Wiley & Sons, 2007.

[135] T. Binder and E. Kostina, “Gauss–Newton Methods for Robust Parameter Estimation,” in *Model Based Parameter Estimation*, H. G. Bock, T. Carraro, W. Jäger, S. Körkel, R. Rannacher, and J. P. Schlöder, Eds. Springer Berlin Heidelberg, 2013, pp. 55–87.

[136] P. Englezos, *Applied Parameter Estimation for Chemical Engineers*. CRC Press, 2000.

[137] J. Rantala, L. Wei, P. K. Kuo, J. Jaarinen, M. Luukkala, and R. L. Thomas, “Determination of thermal diffusivity of low-diffusivity materials using the mirage method with multiparameter fitting,” *Journal of Applied Physics*, vol. 73, no. 6, pp. 2714–2723, Mar. 1993.

[138] L. Wright, X.-S. Yang, C. Matthews, L. Chapman, and S. Roberts, “Parameter Estimation from Laser Flash Experiment Data,” in *Computational Optimization and Applications in Engineering and Industry*, vol. 359, X.-S. Yang and S. Koziel, Eds. Springer Berlin / Heidelberg, 2011, pp. 205–220.

[139] J. V. Beck, “Transient determination of thermal properties,” *Nuclear Engineering and Design*, vol. 3, no. 3, pp. 373–381, Apr. 1966.

[140] S. T. Hsu, “Determination of thermal conductivities of metals by measuring transient temperatures in semi-infinite solids,” *Review of Scientific Instruments*, vol. 28, no. 5, pp. 333–336, 1957.

[141] J. Dempster, *The Laboratory Computer: A Practical Guide for Physiologists and Neuroscientists*. Academic Press, 2001.

[142] G. Lawday, D. Ireland, and G. Edlund, *A Signal Integrity Engineer's Companion: Real-Time Test and Measurement and Design Simulation*. Pearson Education, 2008.

[143] R. Miller, "Thermal barrier coatings for aircraft engines: history and directions," *Journal of Thermal Spray Technology*, vol. 6, no. 1, pp. 35–42, 1997.

[144] R. Schafrik and R. Sprague, "Superalloy Technology - A Perspective on Critical Innovations for Turbine Engines," *Key Engineering Materials*, vol. 380, pp. 113–134, 2008.

[145] J. Beaudouin, M. S. Mommer, H. G. Bock, and R. Eils, "Experiment Setups and Parameter Estimation in Fluorescence Recovery After Photobleaching Experiments: A Review of Current Practice," in *Model Based Parameter Estimation*, H. G. Bock, T. Carraro, W. Jäger, S. Körkel, R. Rannacher, and J. P. Schlöder, Eds. Springer Berlin Heidelberg, 2013, pp. 157–169.

[146] N. Curry, N. Markocsan, X.-H. Li, A. Tricoire, and M. Dorfman, "Next Generation Thermal Barrier Coatings for the Gas Turbine Industry," *Journal of Thermal Spray Technology*, vol. 20, no. 1–2, pp. 108–115, Nov. 2010.

[147] T. M. Yonushonis, "Overview of thermal barrier coatings in diesel engines," *JTST*, vol. 6, no. 1, pp. 50–56, Mar. 1997.

[148] M. Reichling and H. Grönbeck, "Harmonic heat flow in isotropic layered systems and its use for thin film thermal conductivity measurements," *Journal of Applied Physics*, vol. 75, no. 4, pp. 1914–1922, Feb. 1994.

[149] N. Mathis, "'Transient Thermal Conductivity Measurements: Comparison of Destructive and Nondestructive Techniques,'" *High Temperatures-High Pressures*, vol. 32, no. 3, pp. 321–327, 2000.

[150] J. R. Howell, R. Siegel, and M. P. Menguc, *Thermal Radiation Heat Transfer, 5th Edition*, 5th ed. CRC Press, 2010.

[151] L. Michalski, *Temperature Measurement*. John Wiley & Sons, 2001.

[152] D. W. Hahn and M. N. Ozisik, *Heat Conduction*. John Wiley & Sons, 2012.

[153] G. E. Myers, *Analytical methods in conduction heat transfer*. McGraw-Hill, 1971.

[154] T. D. Bennett and R. Valdes, "Differential phase of photothermal emission analysis for thermal property measurement of thermal barrier coatings," *Surface and Coatings Technology*, vol. 261, pp. 102–107, Jan. 2015.

[155] R. Sheppard, D. Morgan, D. Mathess, and D. Bray, "Properties and Characteristics of Graphite for the EDM Industry." Poco Graphite Inc., 2002.

[156] U. Maradia, M. Boccadoro, J. Stirnimann, F. Kuster, and K. Wegener, "Electrode wear protection mechanism in meso–micro-EDM," *Journal of Materials Processing Technology*, vol. 223, pp. 22–33, Sep. 2015.

[157] N. W. Ashcroft and N. D. Mermin, *Solid state physics*. Saunders College, 1976.

[158] S. G. Bapat and H. Nickel, "Thermal conductivity and electrical resistivity of poco grade axf-q1 graphite to3300 degree K.," *Carbon*, vol. 11, no. 4, pp. 323–327, 1973.

[159] M. L. Minges, "Analysis of thermal and electrical energy transport in Poco AXM-5Q1 graphite," *International Journal of Heat and Mass Transfer*, vol. 20, no. 11, pp. 1161–1172, 1977.

[160] R. E. Taylor and H. Groot, “Thermophysical properties of poco graphite,” *High Temperatures - High Pressures*, vol. 12, no. 2, pp. 147–160, 1980.

[161] J. G. Hust, “Graphite as a Standard Reference Material,” in *Thermal Conductivity 15*, V. V. Mirkovich, Ed. Springer US, 1978, pp. 161–167.

[162] A. E. Aliev, S. B. Lee, R. H. Baughman, and A. A. Zakhidov, “Thermal properties of carbon inverse opal photonic crystals,” *Journal of Luminescence*, vol. 125, no. 1–2, pp. 11–17, 2007.

[163] M. L. Minges, “Evaluation of selected refractories as high temperature thermophysical property calibration materials,” *International Journal of Heat and Mass Transfer*, vol. 17, no. 11, pp. 1365–1382, Nov. 1974.

[164] R. Valdes and T. D. Bennett, “Coating thermal diffusivity and effusivity measurement optimization using regression-based sensitivity,” *Review of Scientific Instruments*, vol. 86, no. 1, p. 015108, Jan. 2015.

[165] J. B. Kennedy and A. M. Neville, *Basic statistical methods for engineers and scientists*. New York: IEP, 1976.

[166] E. W. Kreutz and K. Wissenbach, “Coating design for laser transformation hardening,” in *High Power Lasers*, A. N. L. Mordike, Ed. Oxford: Pergamon, 1989, pp. 159–191.

[167] H. W. Coleman and W. G. Steele, *Experimentation, Validation, and Uncertainty Analysis for Engineers*. John Wiley & Sons, 2009.

[168] S. W. Churchill and H. H. S. Chu, “Correlating equations for laminar and turbulent free convection from a vertical plate,” *International Journal of Heat and Mass Transfer*, vol. 18, no. 11, pp. 1323–1329, Nov. 1975.

[169] J. H. Lienhard, *A Heat Transfer Textbook: Fourth Edition*. Courier Corporation, 2013.